The cascaded H-bridge converter for large-scale PV grid-integration with isolated DC/DC converters

The Cascaded H-Bridge Converter for Large-Scale PV Grid-Integration with Isolated DC/DC Converters

by Wei Zhao

UNSW
AUSTRALIA

A Thesis submitted in fulfillment of the requirements for the degree of

Master of Engineering

School of Electrical Engineering and Telecommunications

The University of New South Wales

August 2012

Sydney, NSW, Australia

PLEASE TYPE

THE UNIVERSITY OF NEW SOUTH WALES
Thesis/Dissertation Sheet

Surname or Family name: Zhao

First name: Wei Other name/s:

Abbreviation for degree as given in the University calendar: ME

School: Electrical Engineering and Telecommunications Faculty: Engineering

Title: The Cascaded H-Bridge Converter for Large-Scale PV Grid-Integration with Isolated DC/DC Converters

Abstract 350 words maximum:

As a well-established multilevel converter topology, the cascaded H-bridge (CHB) is suitable for large-scale PV grid-integration due to its high-voltage and high-power capability, high power quality, modular structure, and multiple DC-links which are able to incorporate a large number of PV generators. Since PV system grounding is required by most countries' grid codes and the modulation process of the CHB introduces high potentials upon the DC-side of the converter, galvanic isolation between the PV and the grid is essential to avoid the potential induced degradation (PID) of the PV modules, and to prevent the leakage current, as a result of the PV panel-to-ground parasitic capacitance, from flowing through the converter and ground, posing serious safety concerns. PV isolation can be achieved by the implementation of isolated DC/DC converters. The DC/DC converters connect the PV sources to the CHB converter through DC-links, performing maximum power point tracking (MPPT) and necessary DC voltage amplification, while the imbedded high-frequency transformers isolate the PV from the AC-side.

The thesis presents the system validation and documents the performance evaluation of the CHB converter with isolated DC/DC converters for large-scale PV grid-integration, featuring different power and voltage level configurations, tailored with two control approaches, and through specific case studies. Two isolated DC/DC converter topologies, namely the boost-half-bridge (BHB) and the flyback are implemented.

The CHB converter provides good quality voltage and current waveforms and is capable of medium-voltage grid-connection of the PV system. The system can be well regulated with voltage-oriented control (VOC) schemes both in the synchronous frame using Proportional-Integral (PI) controllers, and in the stationary frame using Proportional-Resonant (PR) controllers. Both DC/DC converters are able to perform MPPT under Standard Test Conditions (STC) and track the varying input voltage reference signal in a wide range fast and accurately. Compared with the flyback, the BHB converter presents lower ripples on the control variables and offers better MPPT efficiency at a higher component count. As the building block of the multiphase DC/DC converters, which feature high-voltage and high-current capability with modular and interleaved structures, the BHB makes a competitive candidate for this application.

FOR OFFICE USE ONLY Date of completion of requirements for Award:

THIS SHEET IS TO BE GLUED TO THE INSIDE FRONT COVER OF THE THESIS

ORIGINALITY STATEMENT

‘I hereby declare that this submission is my own work and to the best of my knowledge it contains no materials previously published or written by another person, or substantial proportions of material which have been accepted for the award of any other degree or diploma at UNSW or any other educational institution, except where due acknowledgement is made in the thesis. Any contribution made to the research by others, with whom I have worked at UNSW or elsewhere, is explicitly acknowledged in the thesis. I also declare that the intellectual content of this thesis is the product of my own work, except to the extent that assistance from others in the project's design and conception or in style, presentation and linguistic expression is acknowledged.’

Signed …….....

Date …….....

Abstract

Advanced power electronics technologies facilitate the large-scale PV energy conversion and grid connection process. Multilevel converters are well suited for large-scale PV integration to the grid due to the high-voltage and high-power capability, high power quality, improved modulation techniques and flexible control strategies. The cascaded H-bridge (CHB) is a well-established multilevel converter topology which is widely applied in high-power medium-voltage drives and STATCOM applications. The modular structure of the CHB and the fact that it features multiple DC-links, make it an attractive option for the large-scale PV grid connection.

Since PV system grounding is required by most countries' grid codes and the modulation process of the CHB introduces high potentials upon the DC-side of the converter, it is necessary to isolate the PV generators from the CHB converter and grid, so as to avoid the potential induced degradation (PID) of the PV modules. More importantly, galvanic isolation between the PV and the grid is essential to prevent the leakage current, as a result of the PV panel-to-ground parasitic capacitance, from flowing through the converter and ground, posing serious safety concerns. PV isolation from the CHB converter and grid can be achieved by the implementation of isolated DC/DC converters. The DC/DC converters fed with the PV sources are connected through DC-links to the CHB converter, performing maximum power point tracking (MPPT) and necessary DC voltage amplification. The high-frequency transformers imbedded in the DC/DC converters isolate the PV from the grid-side, thus the PID issue and the leakage current are not present in the system.

The thesis presents the system validation and documents the performance evaluation of the CHB converter in association with isolated DC/DC converters for large-scale PV grid-integration, featuring different power and voltage level configurations, tailored with two control approaches, and through specific case studies. Two isolated DC/DC converter topologies, namely the boost-half-bridge (BHB) and the flyback are implemented in this system. While the flyback is a typical choice in industrial applications, the BHB presents a modular structure giving low electromagnetic interference (EMI) and a wide input voltage range. The performance of both DC/DC topologies integrated with the CHB grid-connected PV system is investigated through simulation studies.

The CHB converter proves to be adequate to provide good quality voltage and current waveforms and capable of high-power medium-voltage grid-connection of PV systems. The CHB converter system can be well regulated both in the synchronous frame with Proportional-Integral (PI) controllers, and in the stationary frame with Proportional-Resonant (PR) controllers. Both DC/DC converters prove to be able to perform MPPT under Standard Test Con-

ditions (STC) and track the varying input voltage reference signal in a wide range fast and accurately. The BHB converter presents lower ripples on the control variables and offers better MPPT efficiency due to less fluctuation around the operating points compared with the flyback. Although the BHB topology has a higher component count than the flyback, as the building block of the multiphase DC/DC converters which feature high-voltage and high-current capability with modular and interleaved structures, the BHB makes a competitive candidate for this application.

Acknowledgements

Firstly, I would like to thank my supervisor Professor Vassilios G. Agelidis for his continuing guidance, motivation and inspiration in my studies, for sharing his experiences and knowledge of the world along the road.

Secondly, I would like to thank my co-supervisor Dr. Mihai Ciobotaru for his contributions to this project and valuable advice all this time.

I am grateful to my fellow students Mr. Hyuntae Choi and Mr. Guishi Wang for the productive collaborations and pitching of ideas. I would also like to express my gratitude to Dr. Georgios Konstantinou, for his continuous encouragement that leads me through the days.

I would like to thank my dear friends, for shining in the dark, for lighting up my way, for making me who I am.

Last but not least, I would like to thank my family, for their never-ending support, for loving and caring, for always having faith in me. I love you.

Table of Contents

List of Tables

List of Figures

List of symbols

Symbol		Definition
A	:	Effective surface area of the capacitor
C	:	Capacitance
C_{G_PV}	:	PV panel-to-ground parasitic capacitance
d	:	Distance between the capacitor plates
E	:	Solar irradiance
f	:	Frequency
f_s	:	Switching frequency
I	:	Current
I_{G_PV}	:	PV leakage ground current
i_g	:	Grid current
I_{MPP}	:	PV output current at its maximum power point (MPP)
I_{pv}	:	PV output current
k	:	Number of series connected power cells of a multilevel converter
L	:	Main inductor of a the boost converter or the boost-half-bridge (BHB) converter
L_f	:	Grid-side filter inductance
L_g	:	Inductive component of grid impedance
L_k	:	Leakage inductance of the boost-half-bridge (BHB) converter
L_m	:	Inductance of the flyback transformer
m_a	:	Amplitude Modulation Index
N	:	Neutral point of the cascaded H-bridge (CHB) converter
n	:	Number of the voltage levels of a multilevel converter
P_{MPP}	:	PV output power at its maximum power point (MPP)
Q	:	Electric charge
R_g	:	Resistive component of grid impedance
T	:	Temperature
t	:	Time
V	:	Voltage
V_{dc}	:	DC-link voltage
V_g	:	Grid voltage
V_{MPP}	:	PV output voltage at its maximum power point (MPP)
V_{OC}	:	PV open circuit voltage
V_{pv}	:	PV output voltage

α	:	Switching angle
ε	:	Permittivity
θ	:	Phase angle
ω	:	Angular frequency

Sub/Superscript		Definition
$\ldots^{*}$	:	Reference value
$\ldots_{\alpha}$	:	Alpha component in the stationary frame
$\ldots_{\beta}$	:	Beta component in the stationary frame
$\ldots_{d}$	:	Direct component in the synchronous frame
$\ldots_{q}$	:	Quadrature component in the synchronous frame
$\ldots_{abc}$	:	Three phase components in the abc frame

List of Abbreviations

Abbreviation		Definition
AC	:	Alternating Current
APAC	:	Asia Pacific
ANPC	:	Active Neutral Point Clamped
APOD	:	Alternative Phase Opposition Disposition
BHB	:	Boost Half Bridge
CHB	:	Cascaded H-Bridge
CMC	:	Cascaded Matrix Converter
CSC	:	Current Source Converter
CV	:	Constant Voltage
DC	:	Direct Current
DPC	:	Direct Power Control
DTC	:	Direct Torque Control
EMI	:	Electromagnetic Interference
FACTS	:	Flexible Alternating Current Transmission System
FC	:	Flying Capacitor
FFT	:	Fast Fourier Transform
FLC	:	Fuzzy Logic Control
FOC	:	Field Oriented Control
FPGA	:	Field Programmable Gate Array
FRT	:	Fault Ride-Through
GJB	:	Generator Junction Box
GW	:	Giga-Watt
HF	:	High Frequency
HVDC	:	High Voltage Direct Current
IGBT	:	Insulated Gate Bipolar Transistor
IGCT	:	Integrated Gate Commutated Thyristor
INC	:	Incremental Conductance
LF	:	Low Frequency
LS-PWM	:	Level-Shifted PWM
MC	:	Multicell Converter
MEA	:	Middle East and Africa
MF	:	Medium Frequency
MMC	:	Modular Multilevel Converter
MPP	:	Maximum Power Point

MPPT	:	Maximum Power Point Tracking
MSHE	:	Multilevel Selective Harmonic Elimination
MV	:	Medium-Voltage
MW	:	Mega-Watt
NPC	:	Neutral Point Clamped
P	:	Proportional
P&O	:	Perturb and Observe
PC	:	Parasitic Capacitance
PD	:	Phase Disposition
PI	:	Proportional Integral
PLL	:	Phase Locked Loop
POD	:	Phase Opposition Disposition
PR	:	Proportional Resonant
PS-PWM	:	Phase-Shifted PWM
PV	:	Photovoltaic
PWM	:	Pulse Width Modulation
ROW	:	Rest of the World
SHE	:	Selective Harmonic Elimination
SHM	:	Selective Harmonic Mitigation
SoC	:	System on Chip
SPWM	:	Sinusoidal Pulse Width Modulation
STATCOM	:	Static Compensator
STC	:	Standard Test Conditions
SVM	:	Space Vector Modulation
TCC	:	Transistor Clamped Converter
THD	:	Total Harmonic Distortion
UPS	:	Uninterruptible Power Supplies
VOC	:	Voltage Oriented Control
VSC	:	Voltage Source Converter
VSI	:	Voltage Source Inverter
ZCS	:	Zero Current Switching
ZVS	:	Zero Voltage Switching

Chapter 1

Introduction

1.1 Background & Motivation

A sustainable future is essential for the humankind. Along with the extraordinary industrial development in the past century, depleting fossil fuels and the impact of the greenhouse effect are pushing innovations in the energy technologies. As a significant contributor to today's power supply in achieving environmental and economic goals, renewable energy is a feasible solution [1]. During 2011, renewables accounted for almost half of the electricity generation capacity added globally (estimated at 208 GW) [4]. By the end of 2011, the total global renewable power capacity exceeded 1,360 GW [4]. Renewables have contributed to more than 25% of total global power-generating capacity (estimated at 5,360 GW in 2011), and supplied an estimated 20.3% of the global electricity [4]. Wind and solar PV accounted for almost 40% and 30% of the added renewable capacity, respectively, followed by hydropower (nearly 25%) [4].

As the fastest growing renewable energy source, solar PV has gained great public attention in the past decade and is stepping into the main stream energy market. Record PV cell efficiency and unprecedented price reduction driven by the government incentives and technology improvements are bringing a solar PV installation boom throughout the world. Solar PV operating capacity has been increasing by an average of 58% annually since 2006 and through 2011 [4]. The global cumulative and annual installed capacities from 2000 to 2011 are depicted in Fig. 1.1 and Fig. 1.2 respectively, specified with regional data from different countries [2]. Grid-connected applications have gained dominance in an increasing number of countries over the years, as can be seen from Fig. 1.3 [3]. According to EPIA findings, 29.7 GW of PV electricity is integrated to the grid in 2011 up from 16.8 GW in 2010, and solar PV is now the third most important renewable energy source after hydro and wind [2].

While residential PV applications sprout up in every household, large-scale PV power plants are gaining prominent popularity due to the reduced investment cost and the rocketing energy consumption. The annual installed and cumulative capacity of large-scale grid-connected PV power plants in the last decade can be seen in Fig. 1.4 [5]. Large numbers of MW level PV power plants are under construction and being connected to the grid every year. Considering that the solar PV energy yield has an intermittent nature and the output is variable and highly dependent on the atmospheric conditions, such as insolation and tem-

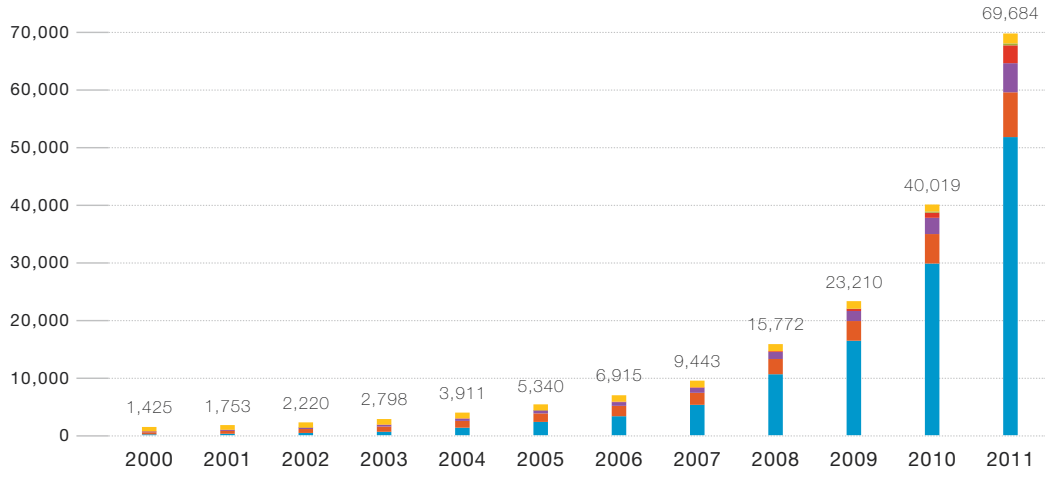

	2000	2001	2002	2003	2004	2005	2006	2007	2008	2009	2010	2011
ROW	751	807	887	964	993	1,003	1,108	1,150	1,226	1,306	1,209	1,717
MEA	N/A	N/A	N/A	N/A	N/A	N/A	N/A	N/A	N/A	21	205	336
China	19	30	45	55	64	68	80	100	145	373	893	3,093
America	146	177	222	287	379	496	645	856	1,205	1,744	2,820	5,053
APAC	355	491	677	902	1,178	1,475	1,797	2,080	2,643	3,409	5,116	7,769
Europe	154	248	389	590	1,297	2,299	3,285	5,257	10,554	16,357	29,777	51,716
Total	**1,425**	**1,753**	**2,220**	**2,798**	**3,911**	**5,340**	**6,915**	**9,443**	**15,772**	**23,210**	**40,019**	**69,684**

Source: EPIA

Figure 1.1. Global PV cumulative installed capacity 2000-2011 (MW)

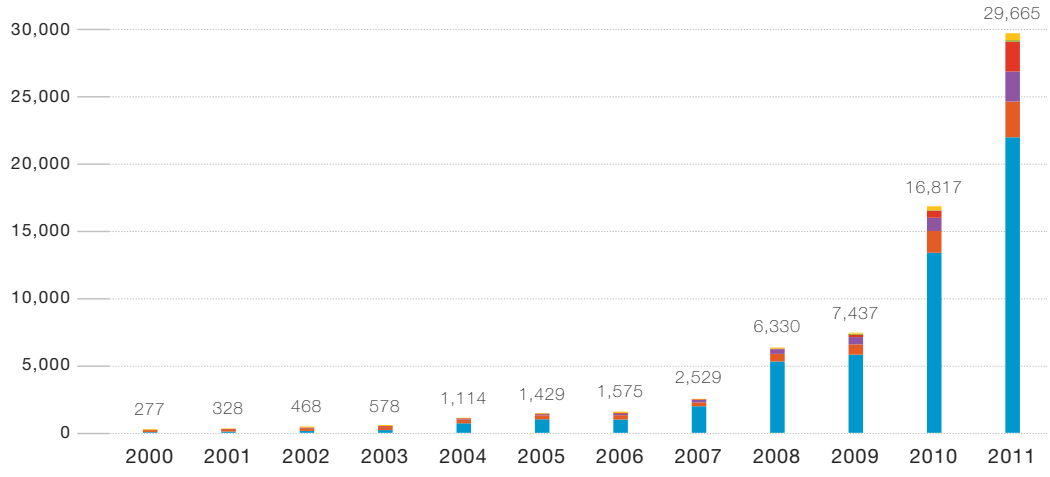

	2000	2001	2002	2003	2004	2005	2006	2007	2008	2009	2010	2011
ROW	88	56	80	77	29	10	105	42	76	80	284	508
MEA	N/A	N/A	N/A	N/A	N/A	N/A	N/A	N/A	N/A	21	45	131
China	0	11	15	10	9	4	12	20	45	228	520	2,200
America	23	31	46	65	92	117	149	212	349	539	983	2,234
APAC	114	136	186	225	276	296	322	283	563	766	1,618	2,653
Europe	53	94	142	201	708	1,002	987	1,972	5,297	5,803	13,367	21,939
Total	**277**	**328**	**468**	**578**	**1,114**	**1,429**	**1,575**	**2,529**	**6,330**	**7,437**	**16,817**	**29,665**

Source: EPIA

Figure 1.2. Global PV annual installations 2000-2011 (MW)

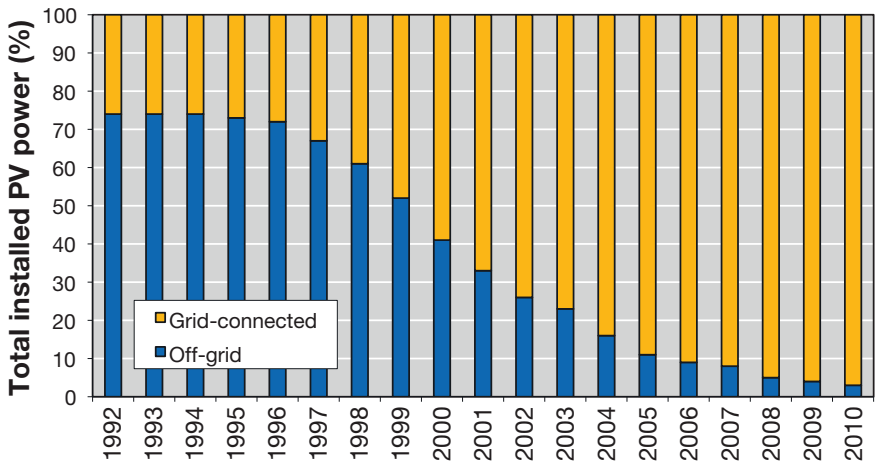

Source: IEA PVPS

Figure 1.3. Percentages of grid-connected and off-grid PV power in the IEA PVPS program 2011 reporting countries

perature, high penetration of PV electricity could challenge the reliability and stability of the grids. Proper forecasting and energy management mechanisms should be utilized to regulate local grids, reducing the intermittency effects and controlling loads in response to network requirements.

As an essential part of the grid integration of PV systems, inverters are being challenged to handle massive power and interact with higher voltage levels. Due to advanced power electronics technologies, PV inverters are getting cheaper and more efficient. However, the increasing penetration of PV generation in the distribution network and the growing demand of a smarter grid require the PV inverters to be more intelligent. Furthermore, large-scale grid-connected PV systems are required to perform grid services including static and dynamic grid support by the grid codes in certain countries [6]. Therefore, the architecture of the PV system and the structure of the PV inverter are crucial for the grid integration of larger PV systems. The conventional PV system architecture mainly includes centralized, string, and multistring topologies. In the meanwhile micro-inverters and DC optimizers, or distributed power conversion products, have been gaining popularity in recent years [8]. However, in order to cope with high voltage and power levels of the large-scale PV systems, novel topologies capable of high capacity, high efficiency, high reliability and high power quality need to be developed.

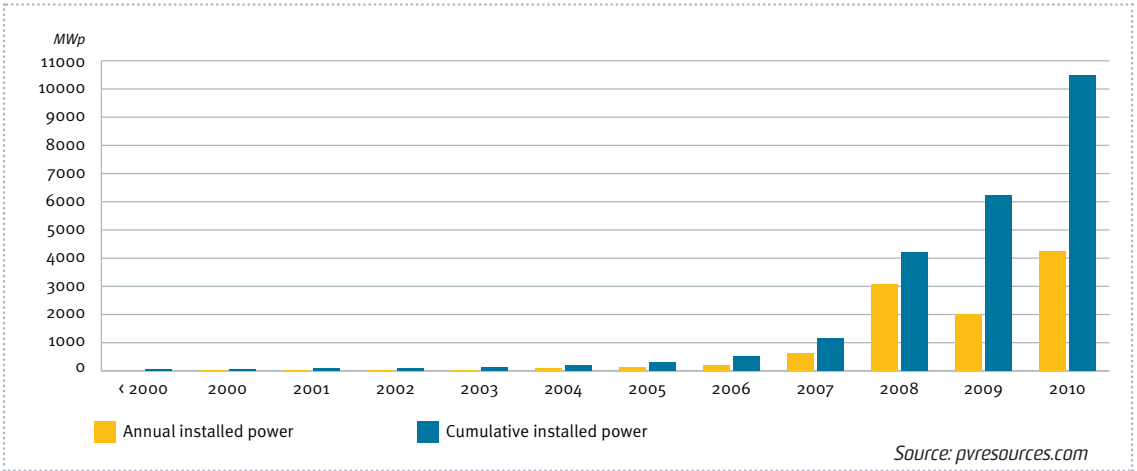

Figure 1.4. Annual installed and cumulative power output capacity of large-scale grid-connected PV power plants 2000-2010

1.2 Objectives

As the power level of the PV system increases and the grid connections happen at medium-voltage grids, multilevel converters can be utilized to perform the power conversion and ancillary services. As the state-of-the-art technology in high-power high-voltage applications, multilevel converters provide improved power quality, reduced switching frequency and low EMI [44]-[75]. One of the mature and proven topologies is the cascaded H-bridge (CHB) converter [44]-[47], [49]-[53]. It offers a modular solution for the grid-connection of PV systems. The PV panels can be grouped into several sections. In each section, a number of PV panels are incorporated to form a separate DC source and connect to the CHB converter via individual DC-links [84]-[102]. By means of cascaded H-bridge power cells, the CHB converter is capable of adding up the voltage of the DC sources, and synthesizing a near sinusoidal stepped waveform at the output through the modulation process. Depending on the number of series connected H-bridge cells, the converter is expandable to different voltage and power levels.

In order to avoid introducing high potentials upon the DC sources due to the modulation of the CHB converter, and prevent the PV panels from generating leakage currents that induce module degradation and pose safety issues, the PV panels have to be isolated from the AC-side and at the same time grounded on the DC-side of the converter [101], [102]. Therefore, isolated DC-DC converters are implemented in the CHB converter system, providing galvanic isolation by the imbedded high-frequency transformers, and meanwhile performing maximum power point tracking (MPPT) individually for the PV generators.

In this work, the CHB converter equipped with isolated DC/DC converters for large-scale solar PV grid-integration is investigated. The function of the system mainly includes DC voltage balancing, grid current regulating and MPPT for the PV generators. Different voltage and power levels of the CHB converter are investigated, two control schemes are applied. Two types of DC/DC converters are integrated into the system and compared on their performance. Detailed analysis on the system behavior and systematic evaluation are provided.

1.3 List of Publications

The work presented in this thesis has resulted in the following international conference publications

[1] W. Zhao, H. Choi, G. Konstantinou, M. Ciobotaru, and V. G. Agelidis, "Cascaded H-bridge multilevel converter for large-scale PV grid-integration with isolated DC-DC stage," in *Power Electronics for Distributed Generation Systems (PEDG), 3rd IEEE International Symposium on*, 2012, pp. 849-856.

[2] H. Choi, W. Zhao, M. Ciobotaru, and V. G. Agelidis, "Large-scale PV system based on the multiphase isolated DC/DC converter," in *Power Electronics for Distributed Generation Systems (PEDG), 3rd IEEE International Symposium on*, 2012, pp. 801-807.

1.4 Outline

The thesis is organized as follows:

Chapter 2 provides an overview of the PV system architecture, featuring the state-of-the-art PV generator configurations and the PV inverter topologies with an emphasis on the isolation in PV systems.

Chapter 3 presents a review of the classic multilevel converter topologies, including their modulation techniques and control scenarios. The working principles, modulation and control of the CHB grid-connected converter system are investigated through simulation studies, featuring different voltage and power ratings of the system and alternative control structures.

Chapter 4 discusses two types of isolated DC/DC converters, namely the boost-half-bridge (BHB) converter and the flyback converter. The functions and characteristics of the two converters are investigated through simulation studies.

Chapter 5 includes a series of simulation studies on the grid-connected PV system featuring the CHB converter with isolated DC/DC converters. The system behavior is investigated through case studies with specific focus on several aspects in order to evaluate essential system criteria and validate the system topology from practical perspectives.

Finally, Chapter 6 concludes the work, summarizes its contributions and suggests ideas for future research.

Chapter 2

PV System Architecture

2.1 Introduction

The International Energy Agency (IEA) has summarized four primary PV applications, namely, off-grid domestic, off-grid non-domestic, grid-connected distributed, and grid-connected centralized PV systems [7]. In general, the first two applications are standalone systems and the last two applications are grid-connected systems. The grid-connected centralized system can perform functions of conventional centralized power system or power conditioning system used for strengthening the utility distribution system, while the grid-connected distributed system is a new approach to power buildings or other loads that are also connected to the electricity network.

A grid-connected PV power system essentially consists of the following components: PV generator (PV modules), generator junction box (GJB), inverters, meters, grid connection, DC and AC cabling [8]. PV systems vary from the use of different PV modules (crystalline silicon or thin-film), the way they are connected (series, parallel), as well as the use of different inverter topologies [8]. Conventional centralized architecture had been utilized before the improvements prone to a more distributed architecture took place in recent years. Novel technical developments such as micro-inverters and DC optimizers have also extended the capability of system configurations. Normally the PV modules are divided into strings and the strings are connected to one or more inverters through one or more power conversion stages. This allows flexible system design in order to tackle technical issues such as module mismatch and partial shading, and to improve the overall system efficiency [9].

Major divergences lie between solar PV power generation and the requirement of the utility grid [8]. The function of the inverter is to interface between the PV system and the grid, in order to feed the solar power into the grid with best possible quality and efficiency [8]. Therefore, a PV system's yield not only depends on the interconnection, orientation and quality of the PV modules, subject to atmospheric and load changes, but also relies heavily on the reliability and efficiency of the inverter [8]. The inverter performs several tasks, mainly the MPPT of the PV arrays, and the power conversion from the direct current (DC) generated by the PV sources into the alternating current (AC) compatible to the grid. Other tasks include system monitoring, information collection, grid support and so on. In order to ensure maximum power yield from the PV sources, the inverter must automatically search for the PV

generator's optimal operating point under various conditions. The Maximum Power Point (MPP) must be constantly tracked as the current and voltage of the PV generator may fluctuate following the solar irradiation and ambient temperature change, which means that the MPP moves back and forth along the PV current-voltage (I-V) curve under the atmospheric condition variations. The MPPT algorithms, which are performed by the inverters, are designed to always locate the MPP with precision under certain conditions, and to follow the MPP movement immediately the irradiation and/or temperature changes. Another task for the inverter is to convert the DC generated by the PV sources into the grid-compatible AC with stable voltage and frequency. In some cases, the conversion can occur with a specific phase shift, in order to feed reactive power to the grid for voltage support or in the event of a grid failure. Apart from that, the inverter also has to ensure the output power quality, perform system control and protection. Advanced power electronics technology enables the power conversion with high efficiency, high reliability, low cost and high tolerance over wide range of input voltage variations. Furthermore, the technology developments drive the inverter towards simpler structure, lower component counts and tighter modular design.

2.2 PV Generator Configuration

As the PV system has a highly modular structure, by dividing the PV generator into strings or arrays and connecting them to one or more inverters, more flexibility can be achieved in the system design in order to serve specific purposes. A number of possible configurations have been proposed [10]-[25]. The commonly used configurations can be categorized as centralized topology, string topology, multistring topology and AC module topology (micro-inverters), as shown in Fig. 2.1. Inverter topologies are selected according to the configuration and the output of the PV modules.

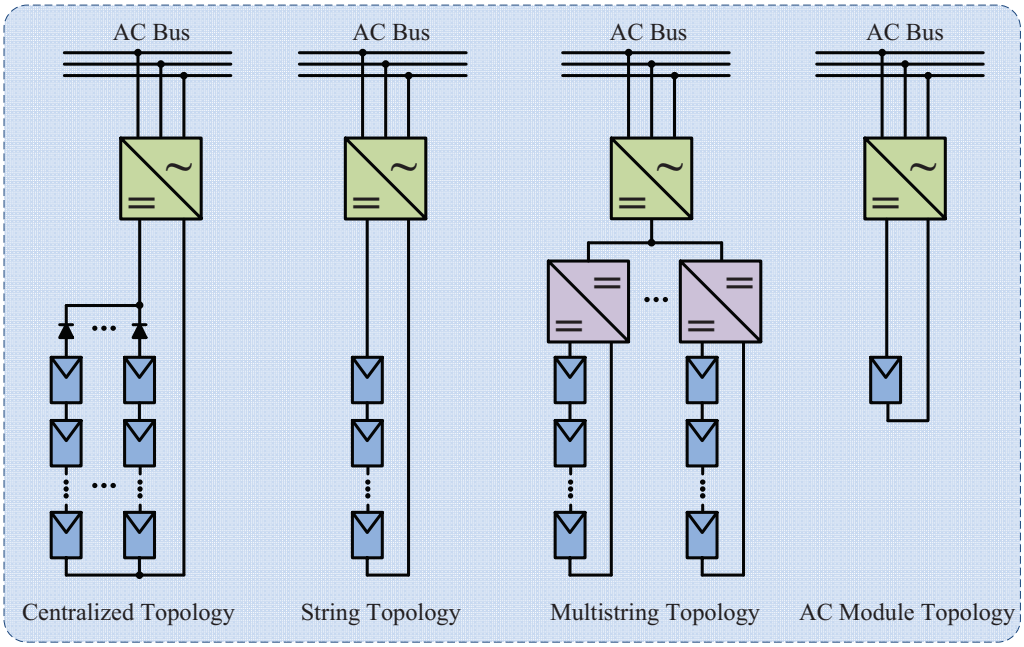

Figure 2.1. PV generator configurations

2.2.1 Centralized Topology

In the centralized topology, the central inverter interfaces an array of PV modules to the grid. The PV modules are divided into series connections which are called PV strings, to build up the output voltage. The strings are then connected in parallel through string diodes to reach higher power levels. This configuration faces limitations, such as high voltage DC cables between PV modules and the central inverter, mismatch losses between PV modules, power dissipated on string diodes, and lack of flexibility in the system design. When the PV plants were small, such a configuration was the norm. However, as PV power systems grow larger and larger in scale, this configuration is no longer adequate to handle the power with good quality and gives low efficiency due to the poor MPPT capability.

2.2.2 String Topology

Instead of one single inverter for the whole PV array, each PV string can be equipped with a separate inverter in the string inverter configuration. No string diodes are needed and the MPP of each string is tracked individually, leading to higher energy yield. This is especially true when the strings are under different shading and insolation conditions throughout the day, the operating points of different strings vary differently.

2.2.3 DC Optimizers

Considering that each module in a string could have its own MPP under certain conditions, controlling the MPP of the string is a compromise between the modules. Separate MPP controllers for every module in a string have been developed, which are called power optimizers, in order to solve this problem. These power optimizers are integrated in the string inverter, enabling optimum power yield from the PV modules and leading to high efficiency. These devices are particularly useful when the PV modules are exposed to different insolation conditions during the day, so shading on individual modules does not impair the yield of the system as a whole. Additional benefits, depending on the device provider, include module mismatch correction, non-uniform module degradation, temperature coefficient difference and uneven soiling among modules.

2.2.4 AC modules

A micro-inverter is one step lower in its conversion capability as each PV module has its own dedicated inverter, thus the PV module with its inverter unit works as an AC module and the output directly feeds the grid [92]. This configuration essentially provides each PV module with optimized adjustment to its MPP through individual MPPT, and removes the mismatch losses between different PV modules. Each micro-inverter is a plug-and-play device which is easy to implement. However, the configuration is not suitable for large commercial and

utility scale installations. Relatively low reliability as well as high specific cost limit this configuration only to special applications [16].

2.2.5 multistring Topology

In order to reduce the extreme inverter count in the AC module configuration while achieving good MPPT and power quality, the multistring topology is derived from the string inverter for higher power level applications. A DC/DC converter stage is introduced to perform individual MPPT for each PV string. PV strings are equipped with their own DC/DC converters and such DC/DC converters are incorporated to connect to a common central inverter. The DC/DC converters act as MPP trackers and provide isolation and DC voltage amplification if necessary. The central inverter converts DC to AC and delivers the power to the grid. This configuration takes advantage of the modularity of the PV generator, which is accompanied by flexibility in design, while retaining a centralized structure, which gives high efficiency and reliability.

2.2.6 Hierarchical Structure and Multilevel Topology for Large-scale PV system

Nowadays for large-scale PV plants, a variant of the centralized configuration with several inverters working in a hierarchical order is applied [8]. The inverters are coupled in a master/slave configuration. The master inverter enables or disables the slave inverters through communication according to the insolation and temperature variations. For a more evenly distributed workload among the inverters, master and slaves usually operate in a rotating order in a fixed cycle. On the other hand, multilevel inverter topologies have the potential to be applied in large-scale PV systems due to their flexibility in design, high power and high voltage capability, as well as better power quality and better MPPT efficiency when applied with multistring configurations [94]. In the following chapters, a multilevel multistring topology featuring the cascaded H-bridge (CHB) converter with isolated DC/DC converters incorporating large numbers of PV strings will be introduced and verified through simulations.

2.3 PV Inverter Topologies

2.3.1 General Classification

As a key component in the PV system, the inverter features various converter topologies and control methods. Traditionally, the inverters used for PV systems are classified based on the number of power processing stages, type of power decoupling, with/without transformers, and types of grid interface [16],[10]. Different circuit topologies and control structures applied in the inverter are also taken into account.

According to the first classification, the PV inverter topologies can be categorized into single-stage inverter, dual-stage inverter and multi-stage inverter. The conceptual diagram of this classification is shown in Fig. 2.2.

As shown in Fig. 2.2(a), the single-stage inverter must handle all the tasks required in PV power processing, which includes MPPT, DC/AC power conversion, grid synchronization, power quality assurance, grid current regulation and requisite voltage control. This configuration is typical for central inverters, with all the associated technical issues. The inverter must also be designed to handle a peak power of twice the nominal power [16].

A dual-stage inverter which includes two power processing stages is shown in Fig. 2.2(b). The dual-stage inverter splits the tasks into two power processing stages, which include a DC/DC stage assigned for MPPT plus requisite voltage amplification, and a subsequent DC/AC stage taking care of the rest such as DC voltage and grid current control by means of pulse-width modulation (PWM), space vector modulation (SVM), and so on.

Multi-stage topologies can be applied in multistring inverters as shown in Fig. 2.2(c). Each PV section is equipped with a dedicated DC/DC converter. The DC/DC converters, which perform MPPT and perhaps boost the voltage, are connected to the DC-link of a common DC-AC inverter, which fulfills other tasks especially grid current regulation.

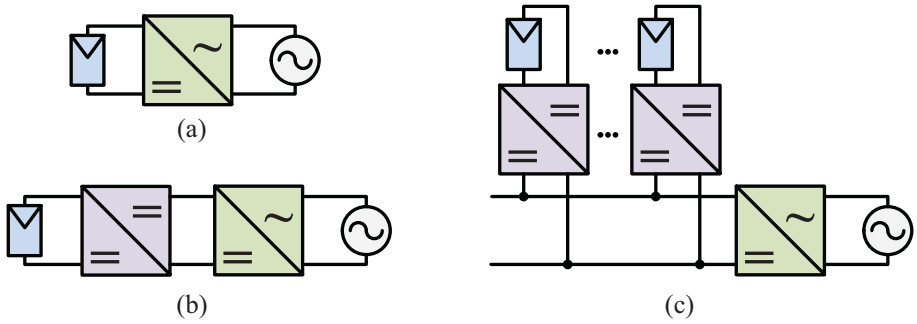

Figure 2.2. PV inverter classification: (a) Single-stage (b) Dual-stage (c) Multi-stage

Further classification of PV inverters is illustrated in Fig. 2.3, with inverter topologies and system configurations taken into consideration, especially the presence of transformers, and whether they are high-frequency (HF) transformers on the DC side or low-frequency (LF) transformers on the grid side [15].

2.3.2 Isolation in PV Inverters

The PV inverter can adopt isolated or non-isolated inverter topologies, depending on the local grid regulations. According to some countries' grid codes, galvanic isolation is required for grid-connected PV systems [16]. This galvanic isolation is usually by means of a transformer, either a HF transformer on the DC side, or a LF transformer on the AC side. Furthermore, a HF transformer imbedded in a DC/DC converter can facilitate the PV panel grounding; whereas including a line-frequency transformer between the inverter and the grid can help reduce the DC injection to comply with grid standards [16].

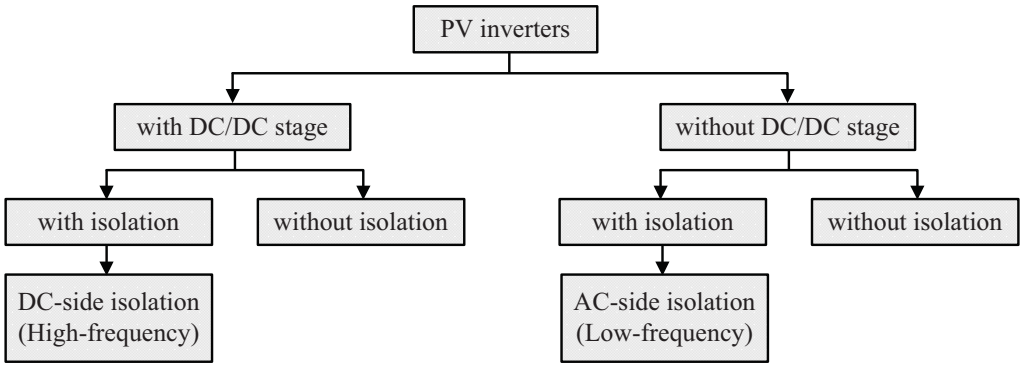

Figure 2.3. Power configuration for PV inverters

On the other hand, some countries allow transformerless PV inverter topologies to be applied while other measures are taken for safety concerns. The advantage of transformerless topologies is mainly the increase of system efficiency due to the removal of transformer magnetic and ohmic losses, and the noise, weight and size of system can also be largely reduced. However, the presence of the PV panel parasitic capacitance and its induced leakage current may cause degradation to the PV modules and pose personal safety issues [31], [26]. Therefore, special design to solve the problems caused by the parasitic capacitance and the leakage current is required for transformerless topologies.

2.3.3 Parasitic Capacitance and Leakage Current

PV panels are typically built in a sandwich structure including glass, silicon semiconductor and backplane with a grounded metallic frame [28]. Parasitic capacitance is generated by the electrically chargeable layer of the PV module which lies in between the glass plates (or foil), faced with the grounded frame, as illustrated in Fig. 2.4 [30]. This capacitance is also related to the material and type of mounting of the PV modules, and varies a lot due to weather-related factors such as humidity, rain and dust. The parasitic capacitance is particularly high for PV modules with flexible substrates and for certain crystalline modules with metallic lining on the back [30].

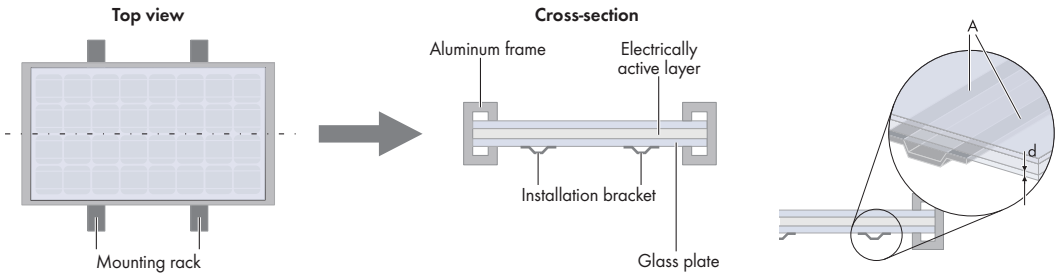

Figure 2.4. PV panel structure and its parasitic capacitor

The capacitance can be calculated using (2.1):

$$C = \varepsilon_0 \cdot \varepsilon_r \cdot \frac{A}{d} \tag{2.1}$$

where ε_0 is the permittivity (physical constant, $8.85 \cdot 10^{-12}$As/Vm), ε_r is the permittivity number which is material dependent, A is the effective surface area of the capacitor and d is the distance between the capacitor plates.

During the operation of a grid-connected PV system, the PV modules are connected through the inverter to the AC grid. Thus an alternating voltage is imposed on the PV modules. In the case when a transformerless inverter is used (single-phase topology is considered), half the grid voltage amplitude is applied at the PV modules [30]. In the case of an isolated inverter topology being used, only a small ripple is passed on to the PV modules. The fluctuating voltage continuously changes the state of charge of the parasitic capacitor of the PV modules, creating a displacement current. This current (root-mean-square value) can be calculated by (2.2), in which f is the fundamental frequency and V is the root-mean-square value of the alternating voltage across the PV modules. This leakage current is a reactive current with 90° phase-shift to the grid voltage, thus incur no loss [30].

$$I = \frac{\Delta Q}{\Delta t} = C\frac{\Delta V}{\Delta t} = C \cdot 2\pi \cdot f \cdot V \tag{2.2}$$

When a transformerless topology is used, the PV modules are directly connected to the grid due to the lack of isolation transformer, forming a direct path for the leakage current to flow through the circuit, as illustrated in Fig. 2.5 [26]. Studies show that in an event of a person touching the surface of the PV panel, a ground current could flow through the human body and cause possible injury [26]. Therefore, the PV modules should be grounded and preferably isolated from the grid side using a transformer, otherwise specific design targeting at leakage current elimination has to take place in a transformerless inverter topology.

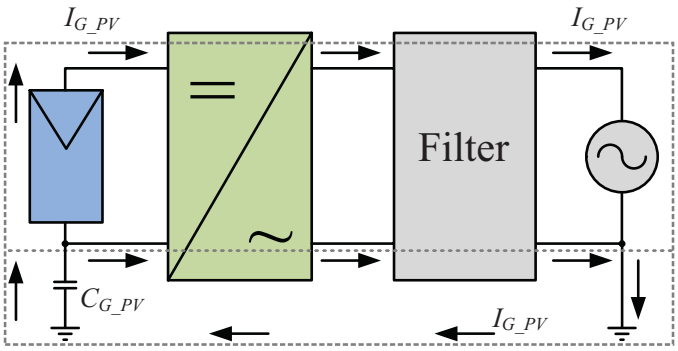

Figure 2.5. Parasitic capacitance ($C_{G,PV}$) between PV panel and its grounded glass frame and the path of the alternating ground leakage current ($I_{G,PV}$) of the transformerless PV system

2.3.4 Transformerless PV Inverter Topologies

Transformerless inverter topologies have been developed to eliminate the leakage current without the presence of a transformer [27]. These transformerless topologies can be categorized into two families [28]. One transformerless topology family is H-bridge based, including H5 inverter (SMA), HERIC inverter (Sunways), REFU inverter (Refu Solar), full-bridge

inverter with DC bypass (FB-DCBP by Ingeteam) and full-bridge zero-voltage rectifier (FB-ZVR). These topologies create zero-voltage states by using an additional switch (H5), an additional AC bypass (HERIC and REFU), or DC bypass (FB-DCBP). H5 and HERIC isolate the PV panels from the grid during zero-voltage states, while REFU and FB-DCBP clamp the neutral to the midpoint of the DC link. The other family of transformerless inverter is derived from the NPC topology, such as NPC half-bridge inverter and Conergy NPC inverter. The NPC derived topologies have higher efficiency, compared to the H-bridge derived topologies, because of the clamping of PV panels during the zero-voltage state and practically no leakage is generated due to the grounded DC-link midpoint. However, this comes at the expense of higher complexity of the circuit. Two typical transformerless topologies, the H5 and HERIC, are shown in Fig. 2.6.

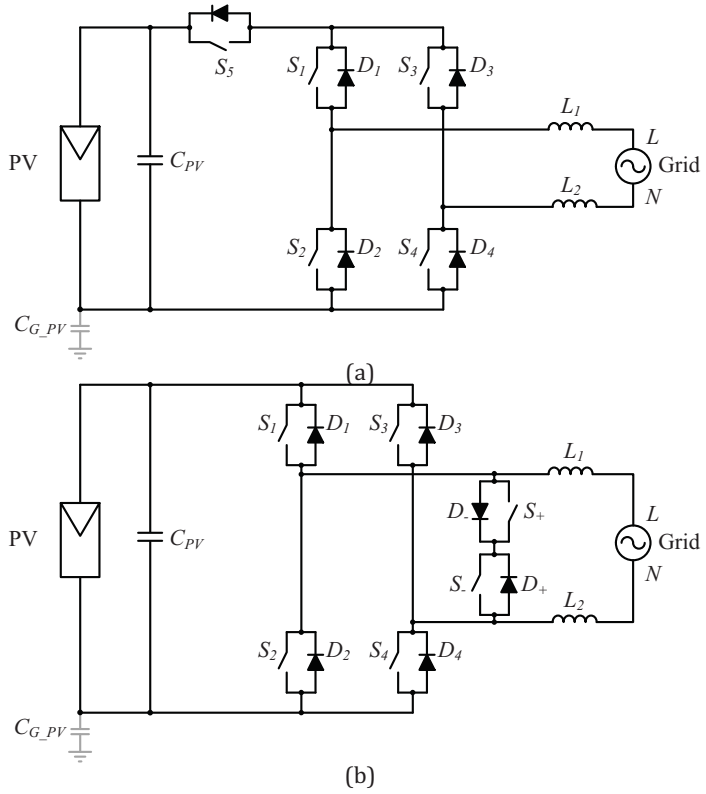

Figure 2.6. Transformerless PV inverter topologies: (a) H5-SMA (b) HERIC

2.4 PV Inverter Control

The control functions of PV inverters include the following aspects: (a) basic functions as common grid-connected converters, including grid synchronization , DC voltage control, and grid current control to meet certain standards regarding power quality and stability; (b) PV specific functions, including MPPT, anti-islanding protection, grid monitoring and plant monitoring; (c) ancillary functions mainly grid support, such as local voltage control, reactive power compensation, harmonic compensation and fault ride-through. The generic control diagram of PV inverters is depicted in Fig. 2.7 [28]. In general, the PV side controller performs

MPPT algorithm on a DC/DC converter to extract maximum power from the PV modules; the grid-side controller regulates the active and reactive power injected to the grid, control the DC-link voltage, ensure the power quality, achieves grid synchronization and performs harmonic compensation. The control structure of the cascaded H-bridge converter with isolated DC/DC converters for a grid-connected PV system will be introduced in Chapter 5. The control scheme of the system will be discussed in detail and verified through simulation studies.

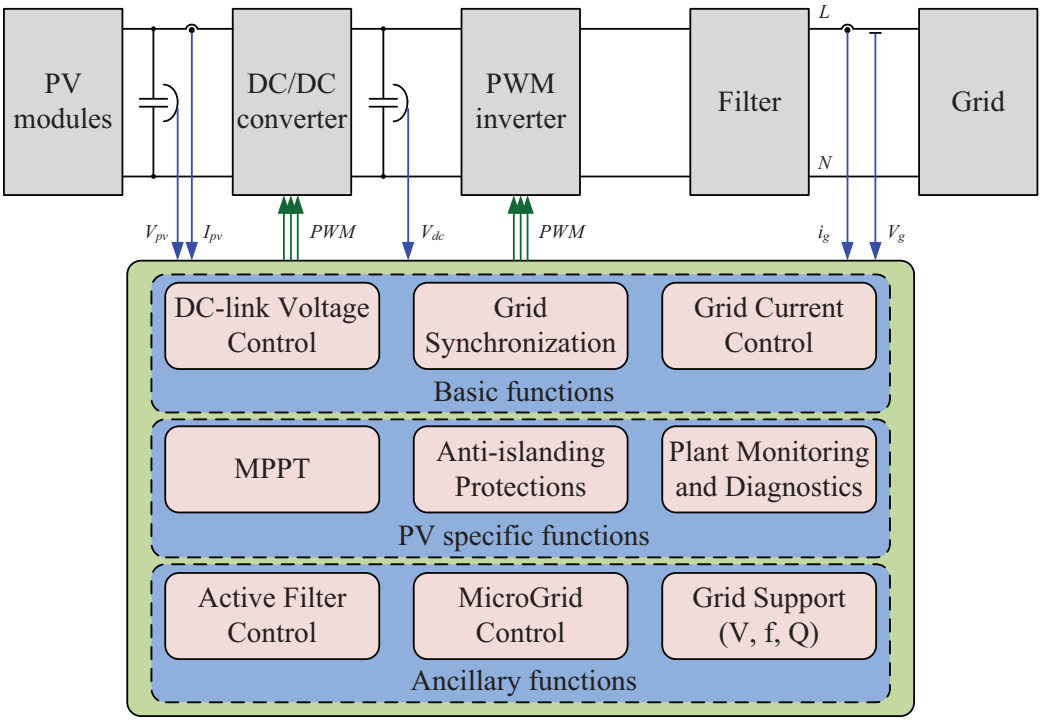

Figure 2.7. Generic control structure of PV inverters

2.5 Multilevel topologies for PV systems

As the power level of the PV systems increases and the grid connections happen at medium voltages, the system can benefit from the utilization of multilevel converters due to the low EMI, reduced switching frequency, increased efficiency and improved waveform quality. Multilevel converter topologies for PV applications have been studied in recent years [32]-[43] and the cascaded H-bridge converter shows great prospective in this application [84]-[102].

Reference [84] introduces a control method and a proportional PWM strategy for a single-phase seven-level CHB converter system for grid-connected PV applications. The control method enables individual MPPT for each PV array, leading to efficient use of the available solar energy and less losses due to mismatch and partial shading. The proportional PWM strategy enables maximum individual H-bridge cell power delivery through perturb and observe (P&O) MPPT algorithm. The modular multilevel configuration of the CHB PV system offers a large number of voltage and power levels, featuring good power quality with low harmonic distortion. The harmonic contents are reduced and moved to higher frequencies,

simplifying the filter design. Another advantage is the reduction in the common-mode perturbations which is originated by the PV panel parasitic capacitance.

A novel three-phase grid-connected PV inverter topology is proposed in [39]. The scheme is based on two isolated PV strings, each feeding a DC bus of a standard three-phase two-level voltage-source inverter (VSI). The two inverters are connected to the grid by a three-phase transformer with open-end windings on the inverter side. This structure performs as a multilevel active power filter. The output voltage waveforms are generated by an improved SVM algorithm which is suitable for the industrial digital signal processors. A novel control method is also introduced to regulate the DC-link voltages and achieve MPPT. However this structure is not scalable to expand to higher voltage levels.

In [33], a three-phase four-level diode-clamped converter is considered for PV systems. A control and modulation scheme is proposed to enable independent control of the operating voltage of each PV array without diminishing the quality of the output power. Compared to a conventional two-level inverter system, the proposed multilevel converter system allows maximum energy yield from the PV arrays especially under partial shading and in case of mismatched PV arrays. Additionally, the multilevel structure offers a reduction of the device voltage ratings, low output harmonic distortion and high system efficiency.

A three-phase three-level NPC converter based on multistring PV system topology is investigated in [34]. The split DC-link of the NPC enables the use of two series connected DC-buses, doubling the voltage level of the system. Hence, less voltage step-up effort has to be made by a DC/DC converter or by a grid-side transformer in order to reach medium-voltage level. The multilevel converter also features good quality waveforms with low switching frequency and thus improved efficiency of the system. Moreover, a large number of PV strings can be integrated into the DC-buses according to the power rating of the NPC, which enables concentrating large-scale PV power system into a central converter, allowing lower losses, smaller size and less cost than using several two-level converters in order to handle the same power. In addition, the DC/DC stage of the multistring approach decouples the DC side from the inverter, thus the MPPT voltage reference of each PV string does not affect the DC bus voltage, enabling fixed DC voltage for the inverter operation and facilitating the power control without introducing voltage distortion.

In [35], a novel integrated fuzzy logic controller (FLC)/modulator is proposed for single-phase CHB converter for PV systems, featuring a fully FLC with no optimal PWM switching angle generator or Proportional-Integral (PI) controller required and an H-bridge power-sharing algorithm. Most of the required signal processing is performed by a mixed-mode field-programmable gate array (FPGA), leading to a fully integrated system-on-chip (SoC) controller, which offers significantly enhanced performance over microprocessor based implementations.

Reference [88] presents a single-phase seven-level CHB converter for grid-connected PV applications. The adopted control scheme enables the independent control of each DC-link voltage and individual MPPT for each PV string. The system provides high quality currents with low switching frequency operation and features modularity and flexibility in system

design. However, a filter is required to eliminate the third harmonic and the filter inductance is limited by the control scheme in order to provide unity power factor.

A control method for a single-phase three-level CHB grid-connected PV system is analyzed in [87]. Two extra stages are added to this traditional voltage oriented control (VOC) scheme, one to introduce MPPT for each PV string and the other to control the DC-link voltage drift due to circulating power in the converter. This control method is capable of power decoupling between PV and grid, individual MPPT for each PV string, unity power factor output, modular design and enhanced efficiency.

The PV AC module introduced in [92] is fitted with a large collection of low-power inverters integrated at PV cell level, meaning that each PV cell has its dedicated inverter for power conversion. The inverter aggregate is controlled by using interleaved carrier PWM. Each solar cell operates at its MPP under various weather conditions. The extreme inverter counts with interleaving offer major benefits such as cancellation of many high-frequency terms, allowing for a very low switching frequency, low voltage rating and reduction of output filter inductance while achieving low current distortion.

A multilevel multistring configuration based on a three-phase CHB converter and isolated DC/DC converters incorporating large numbers of PV strings is introduced [94]. This configuration enables large-scale PV system connection to medium-voltage grids, featuring high flexibility and modularity since it decouples the grid converter from the PV strings, which allows independent control objectives. A control strategy is proposed targeting the power imbalances which occur not only between the H-bridge power cells per phase but also between the three phases. Additional advantages of the system include the inherent superior power quality of the CHB, low switching frequency (higher efficiency) and possible fault tolerant operation due to the cascaded structure.

Reference [96] presents an energy-balance control strategy for a single-phase CHB grid-connected PV converter system. The control scheme is based on an energy-sampled data model of the PV system and features a voltage loop linear discrete controller enabling the operation in the whole range of PV array operating conditions. The control design is adapted to Phase-Shifted and Level-Shifted carrier-based PWM schemes to perform individual MPPT and execute the control goals.

Reference [97] presents a multilevel DC-AC-AC converter topology for medium-voltage grid integration of MW scale PV systems. The large-scale PV system is divided into many zones, and zonal power balancing and MPPT is achieved by employing a current-sharing technique. The power conversion architecture consists of a full-bridge inverter feeding a medium-frequency (MF) transformer with three secondary windings. The voltages at the transformer secondaries are then converted to three-phase line-frequency AC by three full-bridge AC-AC converters. This structure eliminates the 2nd harmonic from the DC bus and removes the bulky line-frequency transformer from the utility interface.

Chapter 3

Multilevel Converters

3.1 Introduction

Multilevel voltage source converters (VSCs) are power converters consisting of an array of power switches and capacitive voltage sources. Multiple-step voltage waveforms are generated by manipulating the combination of the switching states of power semiconductor devices. Stepped waveforms are then synthesized by the voltage levels generated from connecting different numbers of capacitive voltage sources to the load through the power switches. The modulation strategies and control methods for multilevel converters have been investigated and studied extensively [44]-[52]. The past three decades saw the increasing attention on research and development of this technology in both academia and industry [52], [53]. A number of circuit topologies have been well established and polished through the years, while novel designs sprout up continuously [54]-[62].

Multilevel converters have experienced remarkable development in recent years and are considered the state-of-the-art technology for high-power and power-quality demanding energy conversion systems [49]. Significant progress has taken place in this research area and commercialized products have made their way to a wide range of applications [49]-[53]. Due to the high power and voltage levels being achieved, multilevel converters have become an important alternative for high-power medium-voltage fans, pumps, compressors, conveyors, pumped hydro storage, marine propulsion, railway traction, electric and hybrid vehicles, renewable energy conversion, high-voltage direct-current (HVDC) transmission, uninterruptible power supplies (UPS), reactive power compensation, regenerative applications, and so on [63]-[65].

Many reasons account for the growing importance and successful implementation of multilevel converters in high-power applications. Multilevel converters offer numerous advantages over the traditional two-level (2L) converters. The most significant features of multilevel converters are as follows [44]:

- High-power and high-voltage operating capability.
- Better harmonic performance of the output voltages and currents with low harmonic distortion and low voltage derivatives dv/dt, providing near sinusoidal waveforms and good quality power.

- Smaller sized input and output filters could be used if necessary.
- Reduced common-mode voltages (CMV) and the possibility of its elimination by adopting specific modulation methods [66].
- Low switching frequency operation.
- Fault-tolerant operation of the cascaded multilevel topologies by means of bypassing the faulty modules [49].

Multilevel converters have a great potential for future improvements on enhancing the energy efficiency and the system reliability while reducing its cost, size and weight, in order to diversify and broaden their implementation, making a more attractive and competitive option for high-power and high-voltage applications. The following techniques are being developed for this purpose [51]:

- Control modification and modulation optimization to improve harmonic performance.
- Improvement in the design of circuit topologies and selection of device configurations, to reduce the power losses and increase energy efficiency.
- Cost reduction by applying advanced technologies and devices.
- Control strategies for DC capacitor voltage balancing, current ripple reduction, and harmonic mitigation to meet specific standards or grid codes.
- New topology design introducing attractive features and improvement on system performance.

In this chapter, a brief review on multilevel converters is presented, covering the classic topologies, operating principles, modulation techniques and system control methods. Simulation studies of the cascaded H-bridge (CHB) topology are provided for evaluation in the end.

3.2 Classic Multilevel Converter Topologies

As part of the medium-voltage high-power converter family, multilevel converter topologies are classified as shown in Fig. 3.1 [49], [52]. The most known and well established multilevel topologies include the neutral point clamped (NPC) or diode clamped, the flying capacitor (FC) or capacitor clamped, and the cascaded H-bridge (CHB) [52]. The FC and CHB are also referred to as multicell converters (MCs) due to their modular structures [49]. Variations of the three classic multilevel converter topologies and hybrids between them have been elaborately explored over the years [52]. Some of the new topologies found practical applications, such as the active NPC family of converters [60]-[62], the modular multilevel converter (MMC) [67]-[70] and the cascaded matrix converter (CMC) [71]. Several other topologies are

currently under development, such as the CHB fed with unequal dc sources or asymmetric CHB [49], the hybrid NPC-CHB and the stacked FC or stacked multicell [72].

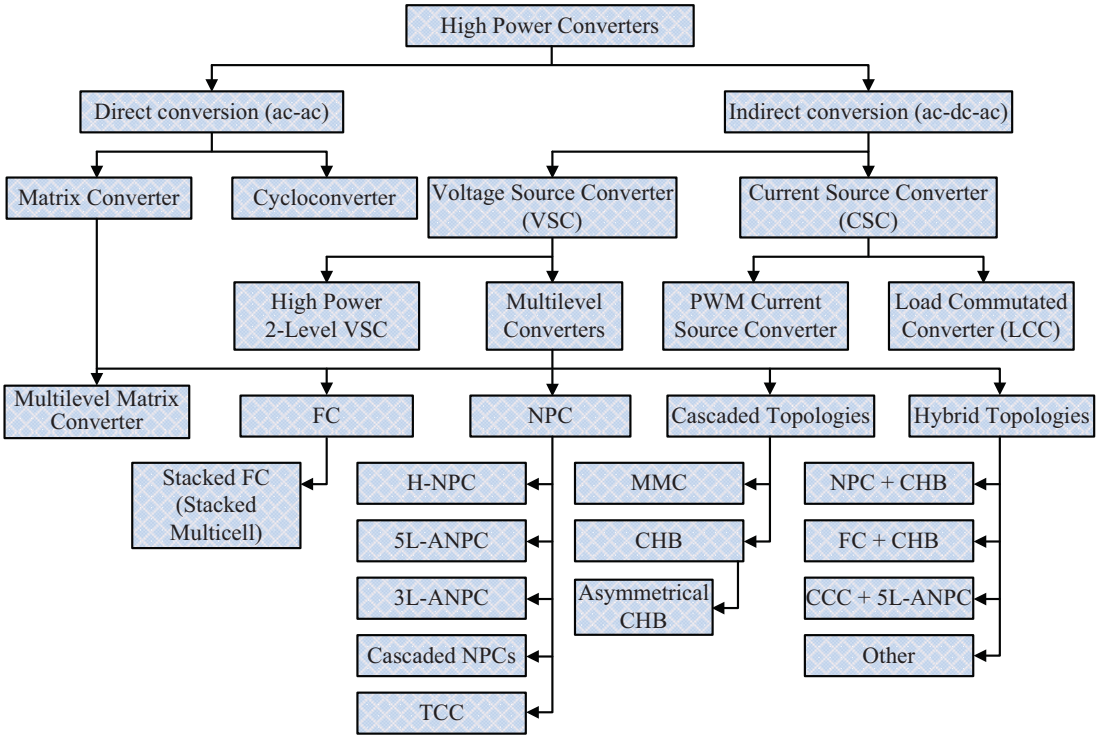

Figure 3.1. Classification of multilevel converters

3.2.1 Neutral Point Clamped (NPC) Converters

An NPC converter consists of two traditional two-level VSCs stacked one over the other, as shown in Fig. 3.2, with the negative bar of the upper converter in conjunct with the positive bar of the lower converter, forming the new phase output. The original outputs of the upper and lower converters are connected through clamping diodes, forming the neutral point N which splits the dc-link voltage in half. Thus the output voltage of the NPC converter consists of three levels, which are V_{dc}/2, 0, and -V_{dc}/2. The switching states with corresponding output voltage levels are listed in Table 3.1.

Table 3.1. Three-level NPC switching states and corresponding output voltage levels

v_{aN}	Switching state			
	S_{a1}	S_{a2}	S_{a3}	S_{a4}
$V_{dc}/2$	1	1	0	0
0	0	1	1	0
$-V_{dc}/2$	0	0	1	1

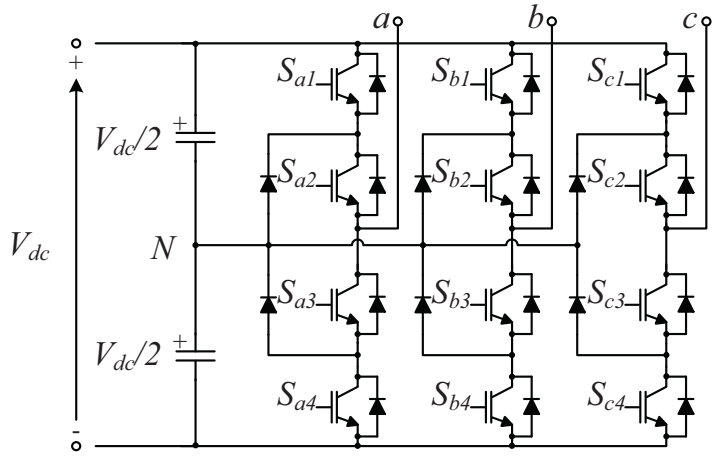

Figure 3.2. Three-level three-phase NPC topology

3.2.2 Flying Capacitor (FC) Converters

Similarly, in the FC topology, which is shown in Fig. 3.3, the dc-link voltage is split by flying capacitors in place of the clamping diodes of the NPC topology. Instead of clamping the output voltage to the neutral of the converter by diodes, the zero voltage is generated by connecting the load to either the positive bus or the negative one of the converter through the FC whichever is with opposite polarity to the dc-link. The switching states and their corresponding output voltage levels are listed in Table 3.2.

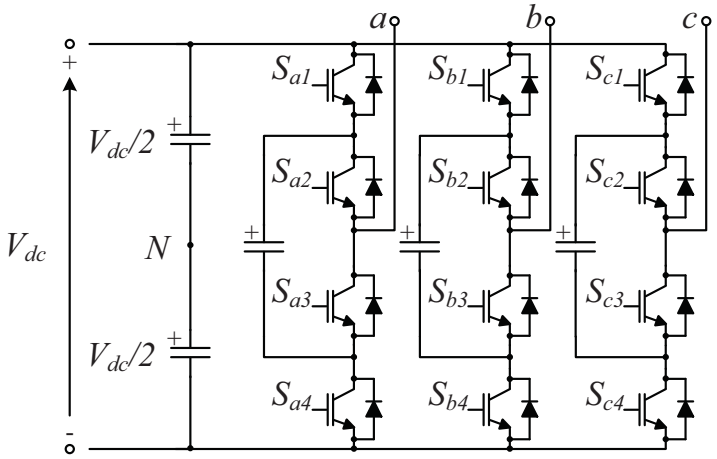

Figure 3.3. Three-level three-phase FC topology

Table 3.2. Three-level FC switching states and corresponding output voltage levels

v_{aN}	Switching state			
	S_{a1}	S_{a2}	S_{a3}	S_{a4}
$V_{dc}/2$	1	1	0	0
0	1	0	1	0
0	0	1	0	1
$-V_{dc}/2$	0	0	1	1

3.2.3 Cascaded H-bridge (CHB) Converters

The CHB converter is structured by a series of cascaded identical H-bridges, as shown in Fig. 3.4. Each H-bridge as a power cell is capable of three different voltage levels at the output. The series connection of the H-bridges generates output voltage waveforms that are synthesized by the combination of each output of the H-bridges at certain switching states. Generally, when k H-bridges are connected in series, the output waveforms contains n=2k+1 different voltage levels and a maximum output voltage of k times V_{dc} assuming all cells have equal and constant DC voltage. The switching states of a single H-bridge power cell and the corresponding output voltage levels are listed in Table 3.3.

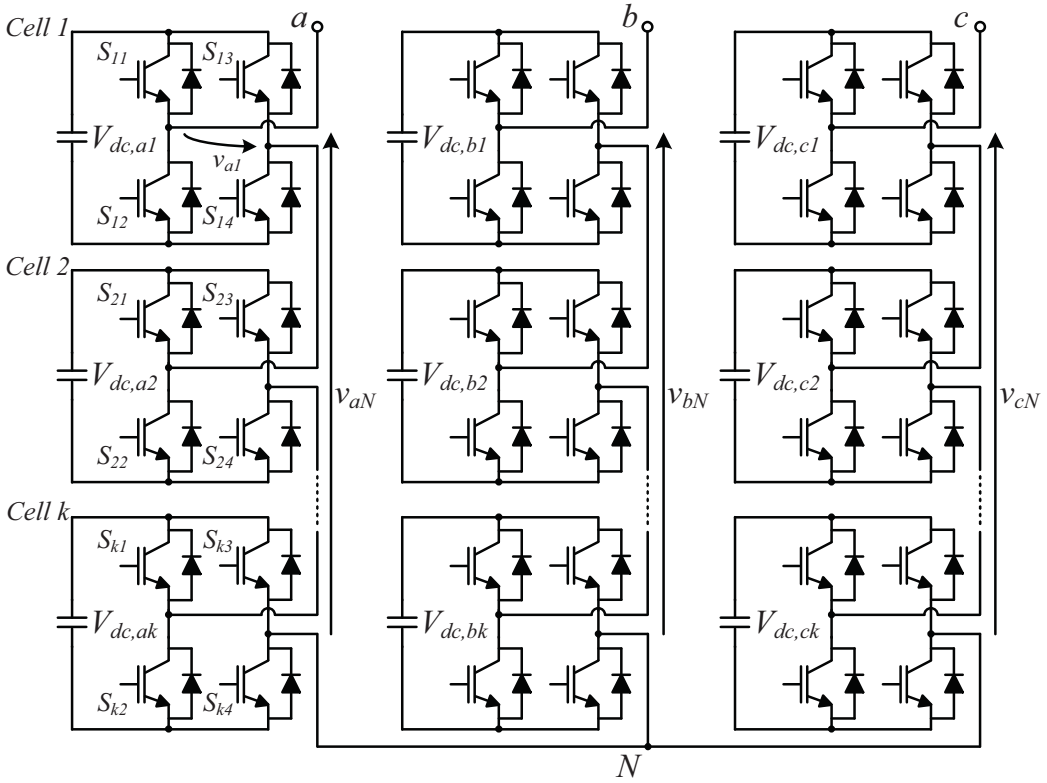

Figure 3.4. k-Level three-phase CHB topology

Table 3.3. H-bridge power cell switching states and corresponding output voltage levels

v_{aN}	Switching state			
	S_{11}	S_{12}	S_{13}	S_{14}
V_{dc}	1	0	0	1
0	1	0	1	0
0	0	1	0	1
$-V_{dc}$	0	1	1	0

3.2.4 Comparison of Multilevel Topologies

The NPC topology is popular for its simple circuit structure and low device count. It features medium/high-voltage devices, such as integrated gate-commutated thyristor (IGCT) and medium/high-voltage insulated-gate bipolar transistor (IGBT). The NPC structure can be extended to higher power ratings with more voltage levels by increasing the number of power switches and clamping diodes. However, large numbers of clamping diodes are needed in order to block higher voltage levels, and higher losses which are unevenly distributed in the circuit are introduced. Furthermore, the balancing of the dc-link capacitors becomes very difficult [57].

The FC topology offers more flexibility in choices of switching combination. However, the number of the clamping capacitors and their individual pre-charge circuits increase largely as the levels go up and the current rating of the flying capacitors becomes high. Besides, the control strategies to maintain the capacitor voltages become very complicated as the capacitor voltages vary with the converter operating conditions, making it not very feasible for high-power applications [57].

On the other hand, the CHB is well suited for high-power applications due to its modular structure which allows higher voltage operation by the series expansion of power cells using merely low-voltage rating semiconductors. The use of identical power cells simplifies the maintenance and reduces the manufacturing costs. The use of phase shifted carriers during the modulation process moves the switching frequency harmonics to a higher range which eases the filtering process. Also, good power quality can be achieved with even lower device switching frequency (≤500 Hz). However, the CHB requires isolated dc sources, which could increase the system complexity, adding up the system cost and weight [52].

The high-power and high-voltage capability of the CHB converter enables connection to medium-voltage grids; and the modular and flexible design make it a competitive candidate for solar PV systems. As the PV systems are growing larger in scale and integrated to higher voltage grids, the CHB converter can be applied to achieve high capacity and good quality power injection to the electricity grids.

3.3 Modulation Techniques for Multilevel Converters

Modulation methods for multilevel converters are basically derived from the traditional techniques used for the 2-level VSC. With more power-electronic devices and switching redundancies, the more complicated circuit structures of multilevel converters give rise to the complexity of the converter control. However, the additional power switches which introduce more switching states, add more control degrees of freedom at the same time. This enables more flexibility in the modulation process which could help reduce the switching frequency, lower the harmonic contents, minimize the common-mode voltage and balance the dc-link voltages, leading to better power quality and higher efficiency. Numerous modulation algorithms have been proposed, adapted for specific aims and improved along with the development of multilevel converter topologies. Common modulation strategies can be classified by the switching frequency used for the converter operation, as shown in Fig. 3.5 [49]. For high-power applications, high switching frequencies are considered to be above 1 kHz.

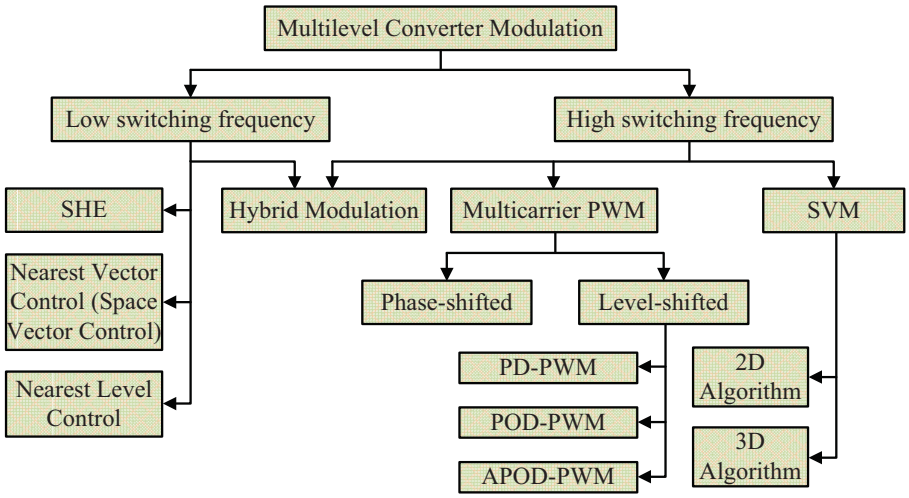

Figure 3.5. Classification of multilevel converter modulation strategies

3.3.1 Multicarrier PWM Techniques

Multicarrier PWM methods are the natural extensions of traditional carrier-based sinusoidal PWM (SPWM). A set of triangular carriers is used for the modulation of the multilevel converter. The phasic or vertical position of the carriers is shifted by a certain angle or level (depending on the level of the converter) between one and another, in order to form multiple-step output voltages of the converter. Phase-Shifted PWM (PS-PWM) and Level-Shifted PWM (LS-PWM) have been developed for the multicell converters (CHB and FC) and for the NPC converter, respectively.

3.3.1.1 Phase-Shifted PWM (PS-PWM)

The Phase-Shifted PWM (PS-PWM) is specially developed for the CHB and the FC converters. Since each H-bridge cell is a three-level converter and each FC cell is a two-level converter, the traditional unipolar and bipolar PWM switching schemes can be adopted, respectively. Due to the modularity of the two topologies, the series-connected power cells within a phase leg of the converter are modulated with individual carrier signals while sharing the same reference signal. A phase shift among the carriers is applied between contiguous power cells. The angle of the phase shift depends on the level of the converter and is tailored to the specific switching scheme which is implemented in each power cell. Optimum harmonic cancellation can be achieved when the phase shift between the carriers is $180°/k$ for the CHB and $360°/k$ for the FC, respectively [47], where k is the number of series-connected power cells per phase leg of the converter. For instance, under unipolar switching scheme, a pair of carriers is associated to each power cell of the CHB, introducing asynchronous switching patterns among different power cells, and stepped multilevel waveforms are synthesized at the output of the converter. The operating principle of a seven-level CHB converter is illustrated in Fig. 3.6. The converter circuit structure is shown in Fig. 3.4, in which k=3.

Since the series-connected power cells within a phase leg of the converter share the same modulating signal and use carriers of the same frequency, the switching device usage and the average power handled by the power cells is evenly distributed across the entire modulation index range. This is advantageous for the CHB as multipulse rectifiers can be used to reduce input current harmonics, and leads to the self-balancing property of the capacitors in the FC topology. Moreover, the phase-shifted carriers introduce a multiplicative effect on the converter operating frequency, which means that the equivalent switching frequency of the converter is k times the actual switching frequency of each power cell. Depending on the switching scheme used in each power cell, which could be bipolar or unipolar, the equivalent switching frequency of the converter is k or $2k$ times the semiconductor device switching frequency, respectively (where k is the number of series-connected power cells per phase leg). Therefore, good harmonic performance can be achieved with low device switching frequency, leading to lower losses and higher efficiency of the converter. The PS-PWM under unipolar switching scheme for a seven-level CHB converter is depicted in Fig. 3.7.

Similarly, for a five-level FC converter, as shown in Fig. 3.8, the switching signal generating scheme is depicted in Fig. 3.9 [48]. The PS-PWM with bipolar switching patterns is illustrated in Fig. 3.10.

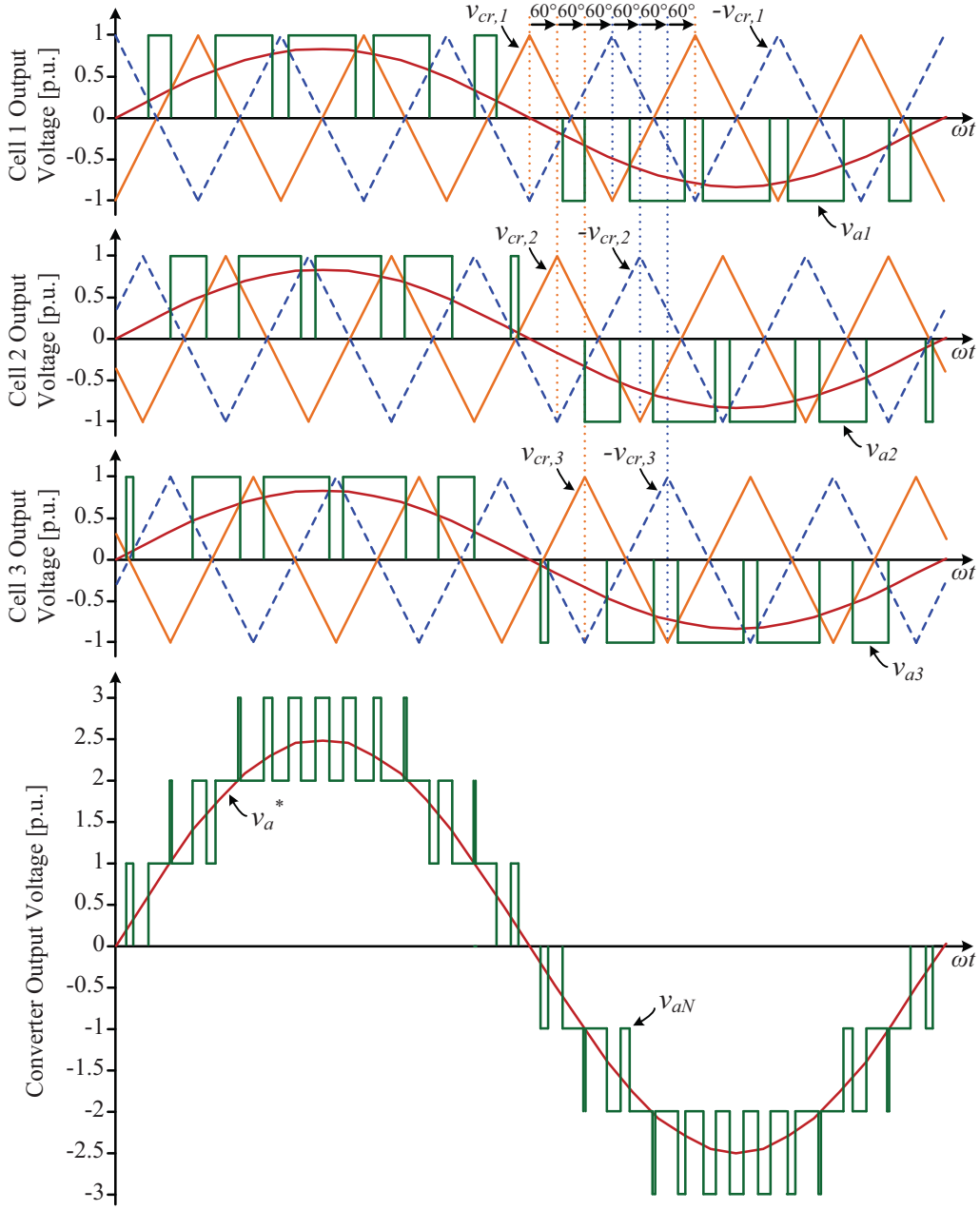

Figure 3.6. Seven-level CHB PS-PWM waveforms (one phase)

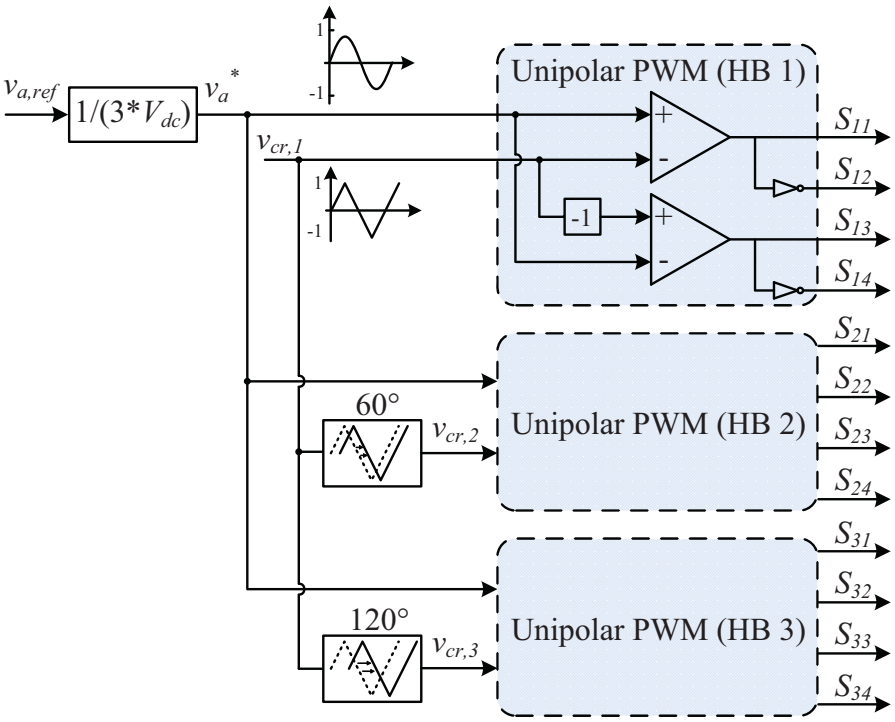

Figure 3.7. Seven-level CHB PS-PWM unipolar switching scheme

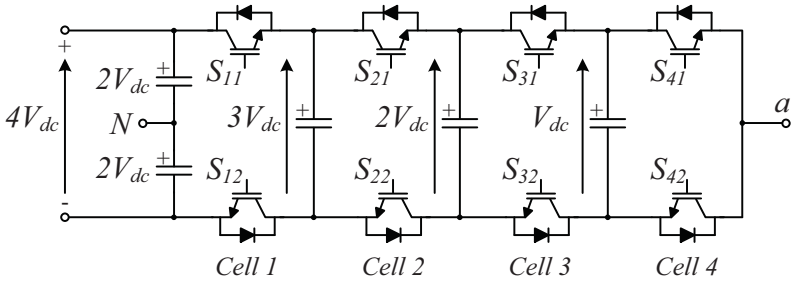

Figure 3.8. Five-level FC converter topology (one phase)

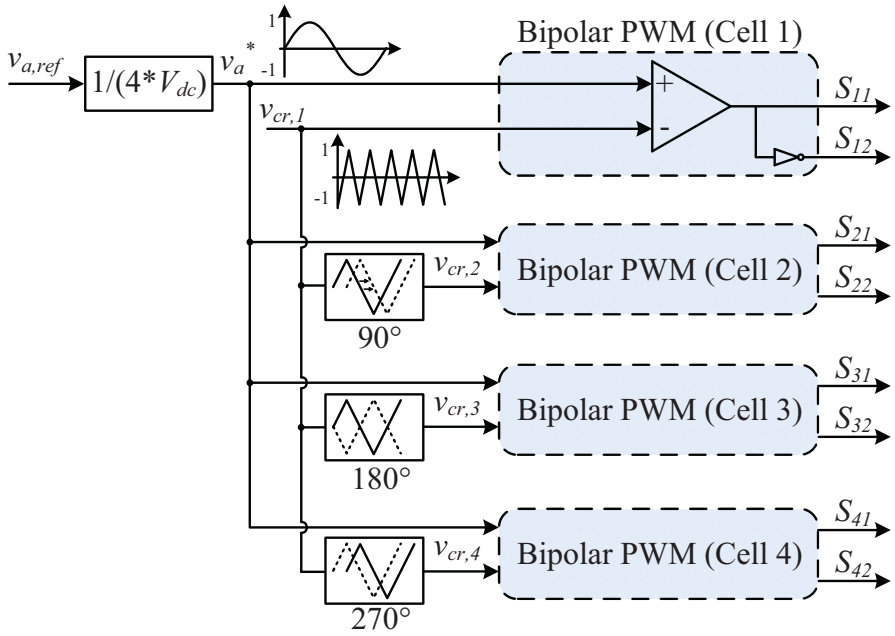

Figure 3.9. Five-level FC PS-PWM bipolar switching scheme

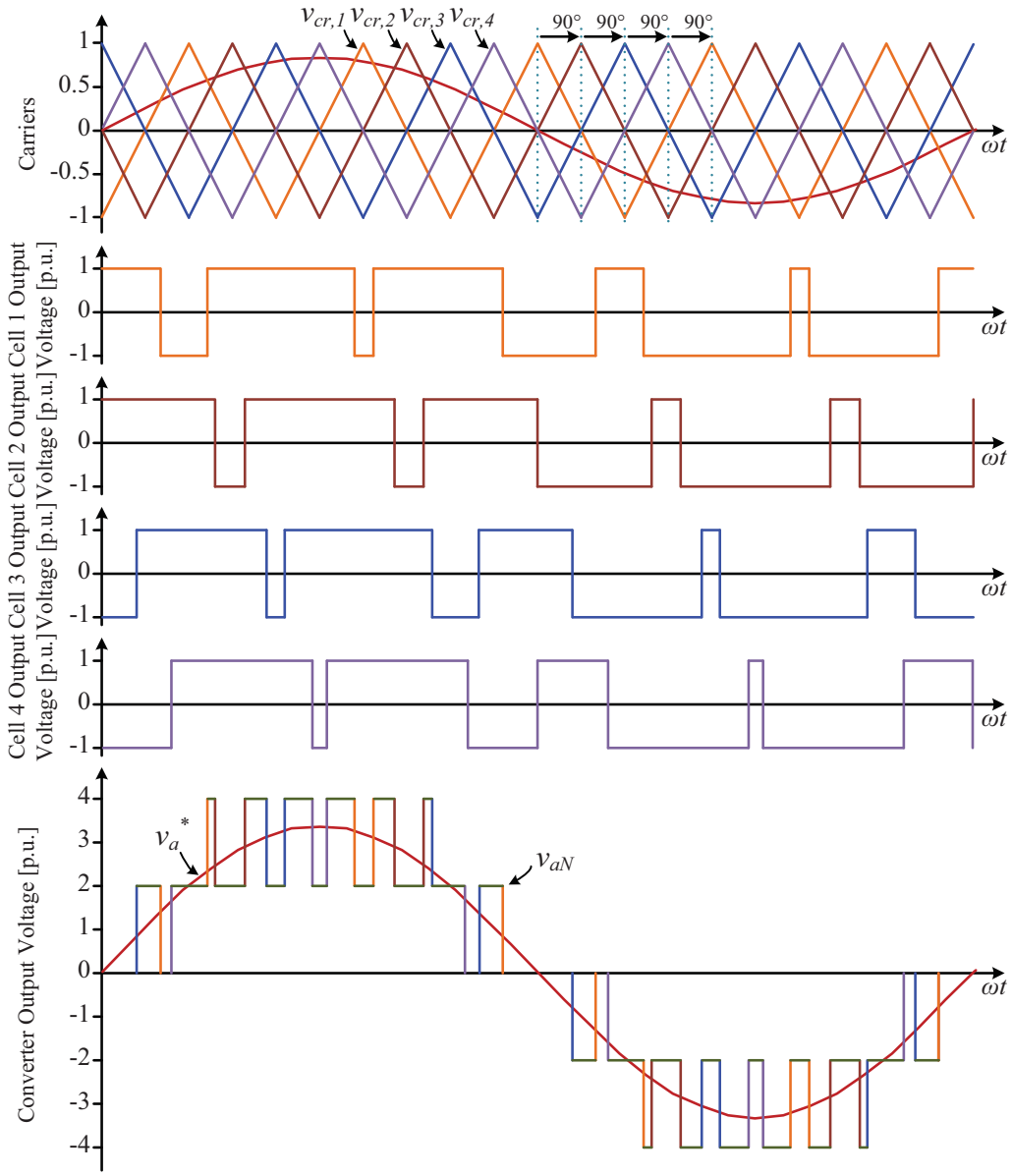

Figure 3.10. Five-level FC PS-PWM waveforms (one phase)

It should be noted that the PS-PWM is the only commercialized modulation method for the CHB and the FC [52]. Although the PS-PWM may not give a better harmonic profile than the LS-PWM, it does not make much of a difference since the harmonics stand at high-frequency and can be easily filtered out. From a practical point of view, the operational advantages of the PS-PWM for the CHB and the FC are much more important and that is why it has gained vast acceptance from the industry.

3.3.1.2 Level-Shifted PWM (LS-PWM)

Similar to the PS-PWM, the Level-Shifted PWM (LS-PWM) is naturally extended from the traditional bipolar PWM switching scheme. Instead of being shifted by a phase angle to create asynchronism for the multilevels to occur, the multiple carriers in the LS-PWM are shifted

in a vertical dimension to cater different voltage levels of the series-connected power cells. For an n-level converter, (n-1) carriers with the same frequency and amplitude are required in the LS-PWM, as in the PS-PWM. Each carrier is set between two voltage levels and the (n-1) carriers are vertically located in a contiguous way that they occupy the full amplitude modulation index range m_a. The amplitude modulation index m_a is defined as in (3.1).

$$m_a = \frac{\hat{v^*}}{(n-1)\hat{V_{cr}}}, \quad 0 \leq m_a \leq 1, \tag{3.1}$$

where $\hat{v^*}$ is the peak amplitude of the reference signal, and $\hat{V_{cr}}$ is the peak-to-peak value of the carrier [47].

Three schemes of arranging the vertical shifts between the carriers are commonly used for the LS-PWM: (a) phase disposition (PD), with all carriers in phase across all bands; (b) phase opposition disposition (POD), with all positive carriers in phase and all negative carriers shifted by $180°$ from the positive ones; (c) alternative phase opposition disposition (APOD), where carriers in adjacent bands are shifted by $180°$ [47]. The PS-PWM for a five-level converter with the above three carrier arrangements is shown in Fig. 3.11.

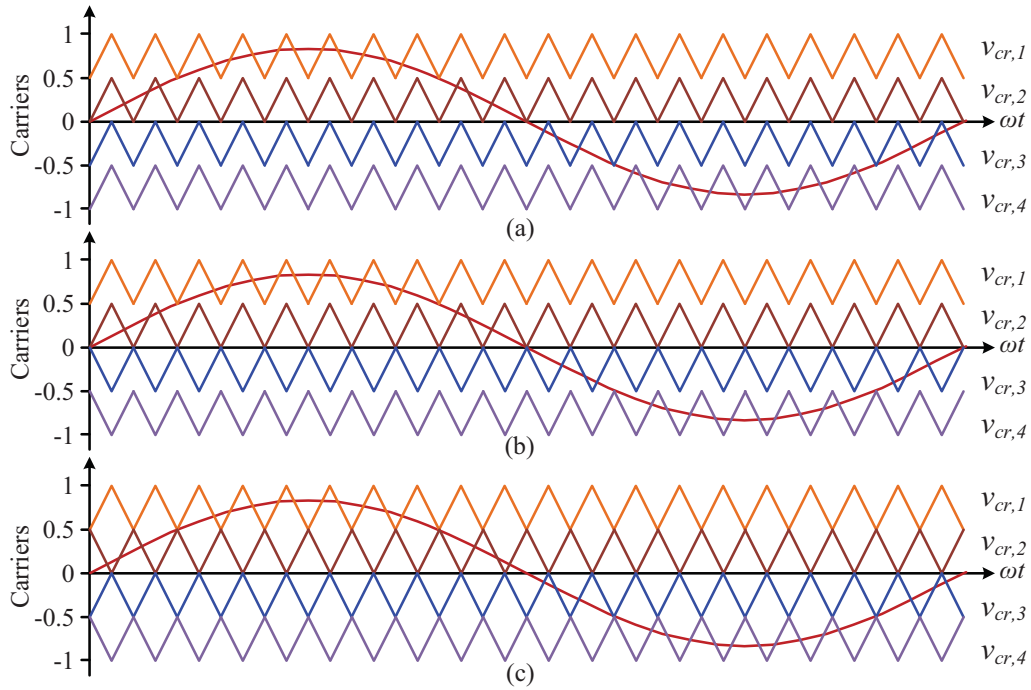

Figure 3.11. LS-PWM carrier disposition schemes for a five-level converter: (a) PD, (b) POD, (c) APOD

The LS-PWM method is especially suited for the NPC converters, as each carrier simply caters for two corresponding power switches. The operating principle of a three-level NPC converter, with PD-PWM carriers and bipolar switching scheme is illustrated in Fig. 3.12 [49].

Compared to PS-PWM, LS-PWM has a slightly better line-to-line voltage Total Harmonic Distortion (THD) performance [47]. However, device switching frequency and conduction period vary with voltage levels, and power is unevenly distributed among the converter cells.

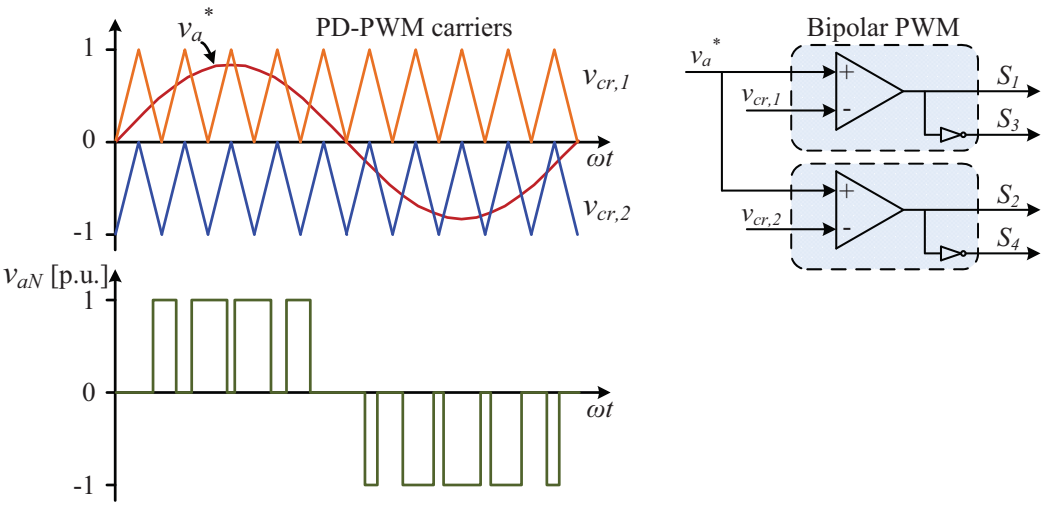

Figure 3.12. LS-PWM for a three-level NPC converter (one phase)

This could result in input current distortion in the CHB, which requires rotating of switching patterns, to evenly distribute the switching and conduction losses [46]. Since the unevenly distributed power could cause capacitor unbalance, the LS-PWM is also not preferable for the FC as well [49].

3.3.2 Selective Harmonic Elimination (SHE)

Selective Harmonic Elimination (SHE) is a low switching frequency PWM method that enables the elimination of undesired low-order harmonics by computing the switching angles offline via Fourier analysis [73] -[75]. This method has the advantage of minimum switching losses due to the very few commutations per cycle and therefore achieves better efficiency. However, this method requires numerical algorithms to solve equations based on the Fourier series and the assumption of steady-state sinusoidal voltages. The pre-calculated solutions are usually stored in lookup tables. Note that these angles cannot fully eliminate the harmonics during variable-speed operation, and the error will be amplified in the closed-loop controller and affect the overall performance of the system. Therefore this method is not suitable for high dynamic performance demanding applications [49].

For the CHB converter, two approaches are available. One is the staircase modulation, which limits the switching frequency of each H-bridge to the fundamental frequency. Each power cell of the CHB converter is associated with a switching angle, and these angles are calculated using the SHE algorithms. This method is rather simple to implement on the CHB with all the pre-calculated switching angles and look-up tables. The operating principle is shown in Fig. 3.13. Compared with the carrier-based PWM schemes, the staircase modulation features low switching losses as all the switching devices operate at the fundamental frequency. The second approach is based on calculating multiple switchings within the levels of the waveform, providing better harmonic performance when compared with the staircase approach [75].

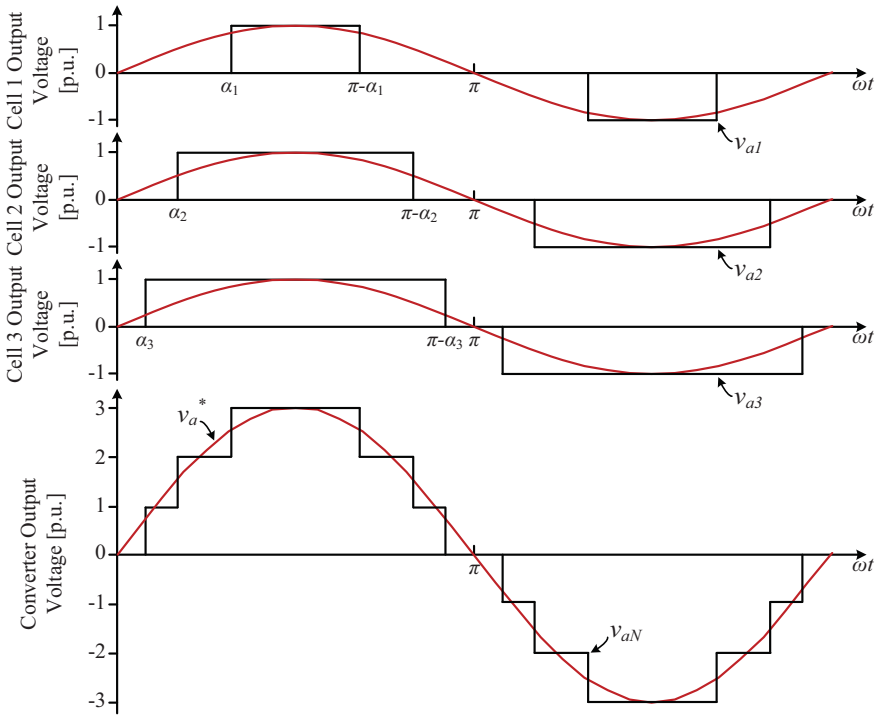

Figure 3.13. Seven-level CHB staircase PWM waveforms (one phase)

3.3.3 Space Vector Modulation

Together with the higher power and voltage capability, multilevel converters bring many more control degrees of freedom. However, the additional zero common-mode voltage vectors, the switching-state redundancy and space vector redundancy are not always fully exploited by the carrier-based PWM schemes. One of the newly developed technologies which have the potential of exploring more control degrees of freedom is the space vector modulation (SVM). The SVM has been employed for multilevel converters using 2-D and 3-D algorithms [52]. SVM-based schemes usually include three steps: (a) selecting switching states, or vectors; (b) computing the duty cycles; (c) generating the sequence. The algorithms may vary on the basic steps in pursuit of lower switching frequency, computational cost reduction, common-mode voltage reduction or elimination, lower THD, or targeting at multiphase systems, unbalanced systems, capacitor voltage balancing and so on [52]. Nevertheless, SVM-based multilevel algorithms do not dominate in the industrial applications nowadays. Since the carrier-based PWM methods only require reference and carrier signals plus simple comparators to deliver the switching signals, they are easy-to-implement mature and mainstream technologies; whereas SVM algorithms are more complex and require a great deal of computational effort.

3.4 Control Strategies for Multilevel Converters

Control strategies for the traditional 2-L VSCs apply straightforward to multilevel converters. Commonly used methods for multilevel converter powered variable-speed motor drives include v/f control (or scalar control), field-oriented control (FOC, or vector control), and direct torque control (DTC) [52] ,[53]. For the v/f control and the FOC, only the modulation stage in the control loop needs adaptation while the control scheme remains the same; whereas it is not the case for the DTC. Since each switching state or voltage vector is associated with a specific change in the motor flux and torque, the DTC cannot be directly extended to multilevel converters. Nonetheless, possible solutions have been proposed for the 3L-NPC and some other multilevel topologies [52].

Control strategies for grid-connected multilevel converter systems include voltage-oriented control (VOC) and direct power control (DPC), which are the counterparts of the FOC and the DTC used for drives. The VOC achieves high static and dynamic performance through the combination of an outer voltage loop and an inner current loop. The control diagram of a grid converter with the VOC is shown in Fig. 3.14. On the other hand, the DPC directly selects the switching states from a switching table based on the instantaneous errors between the commanded and estimated values of active and reactive power [28]. The main advantage of the DPC is the simplicity in algorithm and the key to this method is the correct and fast estimation of the active and reactive power. However, it requires high sampling frequency to obtain satisfactory performance and is difficult to implement under stiff grid condition [28].

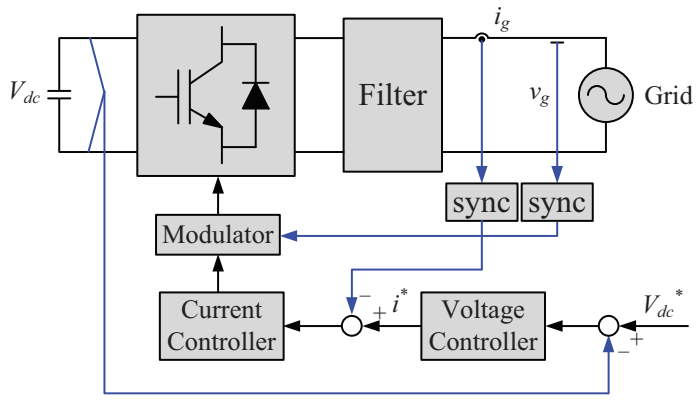

Figure 3.14. Generic VOC control diagram

3.4.1 Voltage-Oriented Control (VOC)

3.4.1.1 Synchronous Frame VOC

Typically VOC is implemented in the dq reference frame, rotating at the speed of ω and oriented in such a way that the d axis is aligned with the grid voltage vector. In the dq frame the vector of the fundamental has constant components while the harmonic vectors have pulsating components. Since the grid converter is used to generate or absorb sinusoidal currents,

the reference current components in the dq frame are DC quantities. The d component of the reference current I_d^* is controlled to manage the active power and perform the DC voltage regulation; while the q component I_q^* is controlled to manage the reactive power and obtain a unity power factor. In order to have the grid current vector in phase with the grid voltage vector, the I_q^* is normally set to zero. The general control diagram of the VOC in the synchronous rotating dq frame featuring an inner current loop and an outer voltage loop with cross-coupling and voltage feed-forward is shown in Fig. 3.15. The synchronization between the converter and grid is achieved by a three-phase phase-locked loop (PLL). Normally PI controllers are used in this control structure since all the control variables are transformed to DC values in the dq frame. Typical transfer function of a PI controller is given by (3.2),

$$G_{PI}(s) = K_p + K_i \frac{1}{s}. \tag{3.2}$$

where K_p is the proportional gain and K_i is the integral gain of the controller.

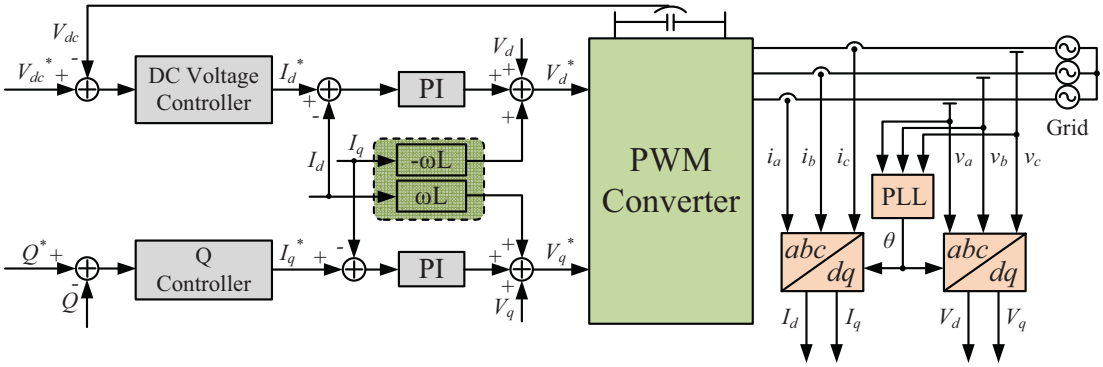

Figure 3.15. Synchronous frame VOC

3.4.1.2 Stationary Frame VOC

Apart from the rotating dq reference frame, VOC can also be performed in the $\alpha\beta$ stationary frame. The general control structure of the VOC in the stationary frame using resonant controllers and harmonic compensators is shown in Fig. 3.16. Since in the stationary reference frame the control variables are time-varying signals, PI controllers are not capable of removing the steady-state error. In this case, Proportional-Resonant (PR) controller is introduced in the $\alpha\beta$ control structure due to its ability of regulating sinusoidal signals without steady-state error [113], [114]. Additionally, harmonic compensators which eliminate low-order harmonics without affecting the controller dynamics are easy to implement in this control structure. The PLL is used for adapting the frequency of the PR controllers and extracting the fundamental of the grid voltages which are used for calculating the reference current components.

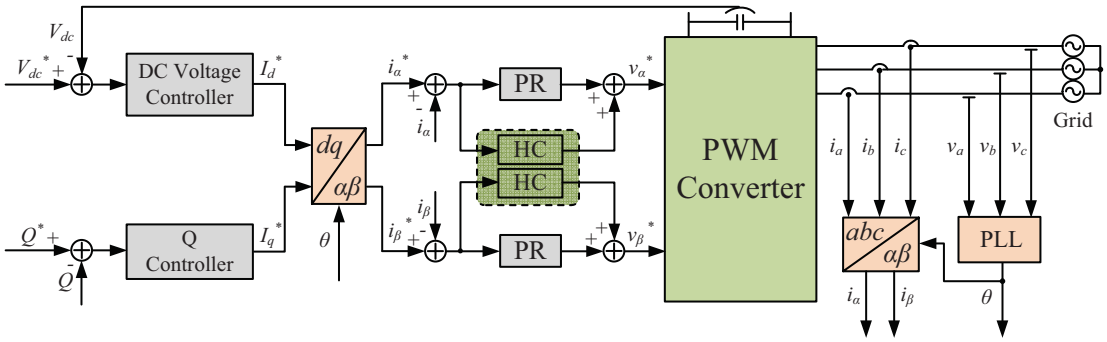

Figure 3.16. Stationary frame VOC

3.5 Simulation Studies of the Cascaded H-bridge Converter

Simulation studies are conducted on the CHB converter for its performance evaluation. A seven-level three-phase CHB converter is investigated on its behavior under PS-PWM with DC voltage sources and its control performance of grid-connection with DC current sources. The control performance is investigated in a 300 kW system and 3 MW system respectively. Furthermore, a vertical extension of the CHB is investigated by increasing the series connected H-bridge cells in order to integrate more power to higher voltage grids. A thirteen-level three-phase CHB converter is investigated in a 3 MW grid-connected system, regulated by PI controllers in the dq frame and PR controllers in the $\alpha\beta$ frame, respectively. The simulations are performed in MATLAB/Simulink and PLECS Blockset.

3.5.1 CHB Converter with DC Voltage Sources

The parameters used in the simulation are listed in Table 3.4. The circuit structure of the 7-L CHB converter fed with DC voltage sources is shown in Fig. 3.17. The modulation diagram of the CHB converter is shown Fig. 3.18. Carriers with the same phase disposition are applied to each phase of the converter.

The output voltages of the three series connected H-bridges in one converter phase are shown in Fig. 3.19. The synthesized phase output voltage is shown in Fig. 3.20. Moreover, Fig. 3.21 shows the PWM induced potential added upon the DC sources, which poses challenges for the CHB converter applications in PV system since galvanic isolation would be necessary to prevent the PV panel leakage currents from flowing through the converter and pose safety concerns [26]. This high potential could also cause degradation of the PV modules and shorten their lifetime [31]. These issues will be discussed further in the following chapters.

Table 3.4. Simulation parameters - The CHB converter with DC voltage sources

Modulating Signal		CHB Converter	
Frequency	50 Hz	DC Voltage	2 kV
Modulation Index	0.8	Switching Frequency	500 Hz

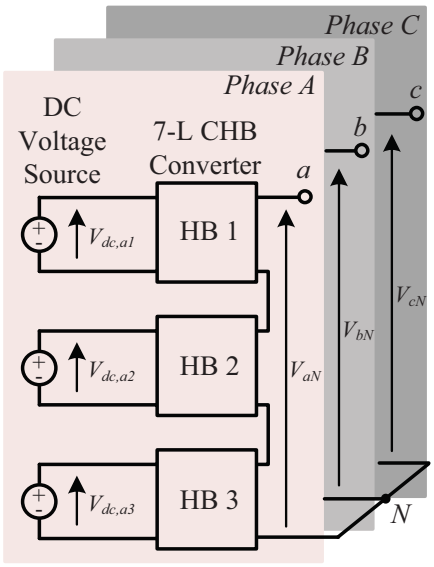

Figure 3.17. 7-L CHB converter fed with DC voltage sources

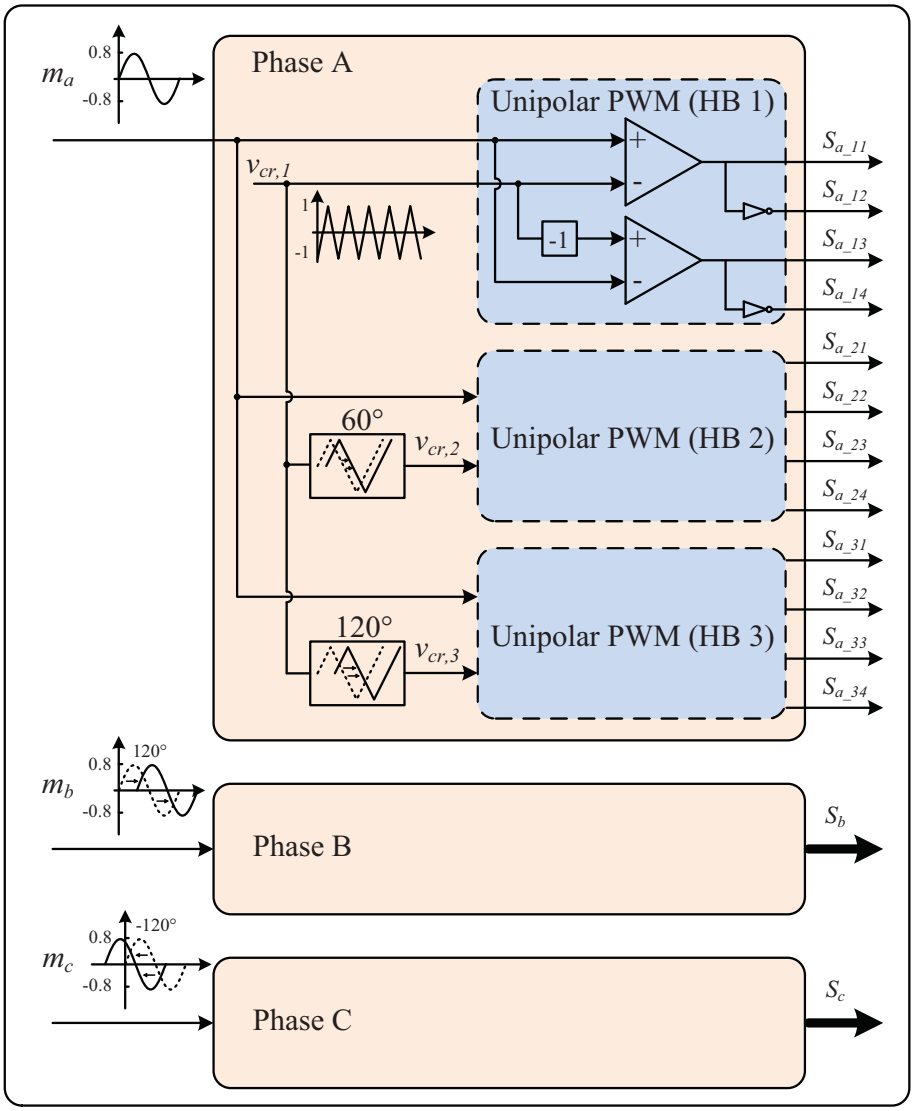

Figure 3.18. Modulation diagram of the 7-L CHB converter

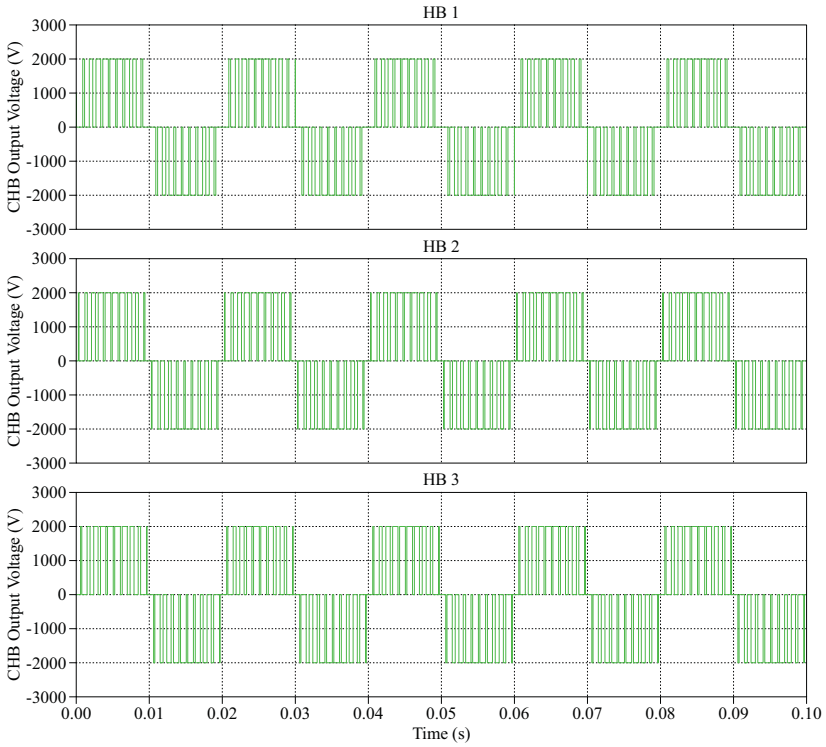

Figure 3.19. Output voltage waveforms of the H-bridge power cells (one phase)

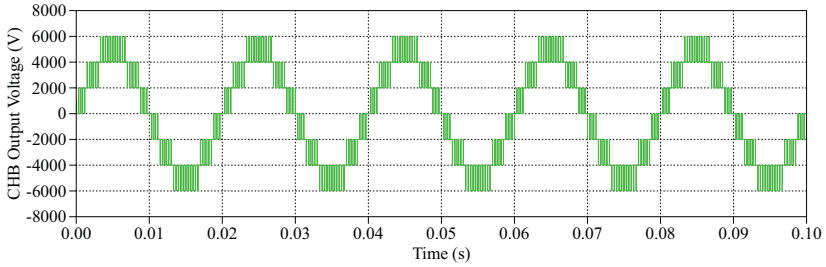

Figure 3.20. Output voltage of the 7-L CHB converter (one phase)

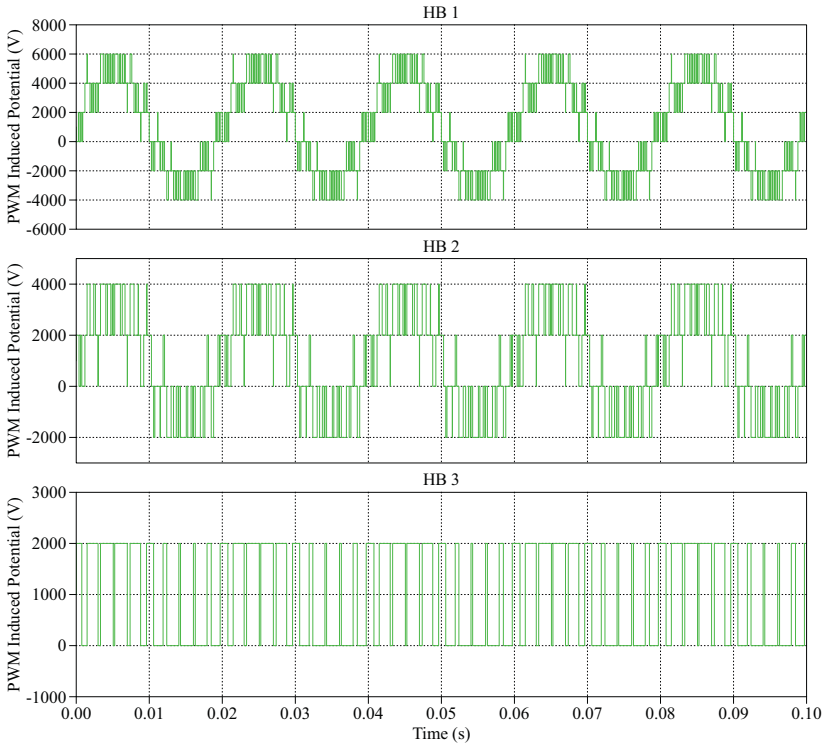

Figure 3.21. PWM induced potential at the DC-side of the CHB converter (one phase)

3.5.2 Grid-connected CHB Converter with DC Current Sources

The circuit structure of the 7-L CHB converter fed with DC current sources is given in Fig. 3.22. The control diagram of the CHB grid-connected converter is given in Fig. 3.23, based on the synchronous frame VOC method. The abc/dq transformation is given in eq. (3.3).

$$\begin{bmatrix} y_d \\ y_q \end{bmatrix} = \frac{2}{3} \begin{bmatrix} \cos\theta & -\sin\theta \\ \cos(\theta - 120°) & -\sin(\theta - 120°) \\ \cos(\theta + 120°) & -\sin(\theta + 120°) \end{bmatrix}^T \cdot \begin{bmatrix} x_a \\ x_b \\ x_c \end{bmatrix} \tag{3.3}$$

The converter is rated 300 kW for the first simulation study, and then the power rating is increased by 10 times to 3 MW with a different set of controllers and component parameters. This is to investigate the voltage and power capability of the 7-level CHB converter and its performance in regulating the DC-link voltage and grid currents both in steady-state operation and with varying power supplies.

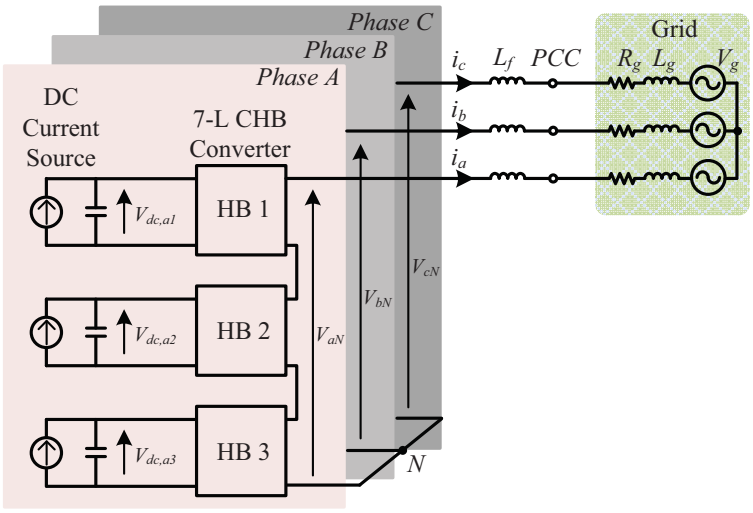

Figure 3.22. 7-L CHB converter fed with DC current sources

3.5.2.1 300 kW System

The parameters used in the simulation are listed in Table 3.5.

A. The Steady-state

The nine DC-link voltages are shown in Fig. 3.24. They are well balanced and remain at 2 kV level with less than 0.003 p.u. fluctuation, given that a 5 mF capacitor is used to maintain the DC-link voltage. The three DC-link currents of converter phase A are shown in Fig. 3.25. They are distributed evenly among the H-bridges with a mean value of 16.6 A. The phase output voltage and the line-to-line output voltage of the converter are shown in Fig. 3.26(a) and (b). Each phase output voltage contains seven levels and each line-to-line voltage contains thirteen levels. The voltage steps form nearly sinusoidal shaped waveforms.

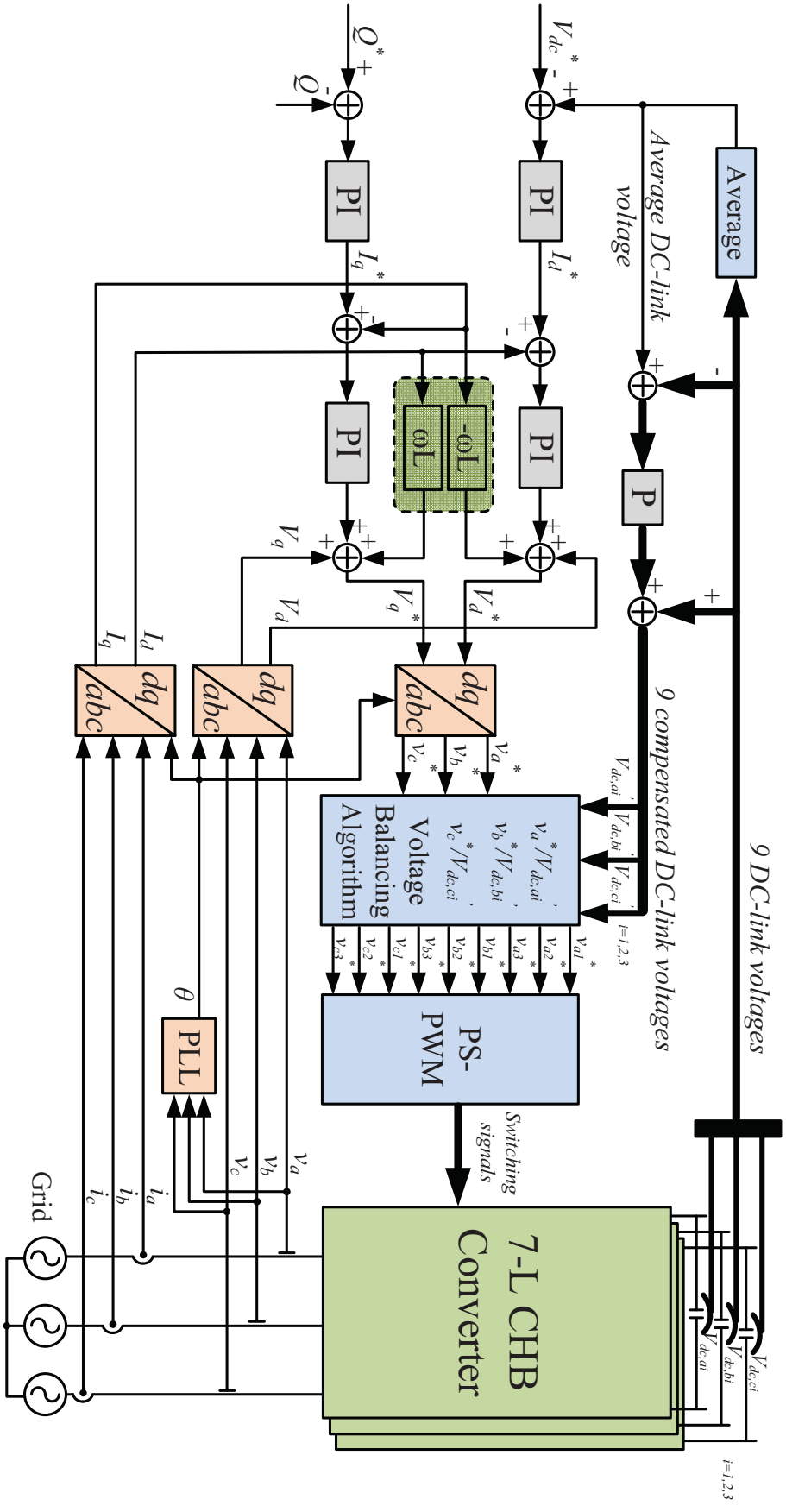

Figure 3.23. Control diagram of the 7-L CHB grid-connected converter

Table 3.5. Simulation parameters - The CHB converter with DC current sources (300 kW)

CHB Converter		Grid	
DC-link Voltage	2 kV	Grid Voltage (line-line RMS)	6 kV
Switching Frequency	1000 Hz	Fundamental Frequency	50 Hz
Rated Power	300 kW	Grid Impedance	R_g =5.4 mΩ L_g =172 μH
DC-link Capacitor	5 mF	Grid-side Filter	20 mH
PI Parameters			
Current Loop		Voltage Loop	
K_p =100	K_i =5000	K_p =20	K_i =1500
DC Voltage Balancing		K_p =20	

The three phase grid currents are shown in Fig. 3.27. They are sinusoidal with a THD of 2.68%. The THD reading in this work is directly obtained from the data analysis performed by PLECS. On the other hand, the THD can be calculated by its definition, as given in eq. (3.4).

$$\text{THD} = \sqrt{\frac{\sum_{\nu \geq 2} V_\nu^2}{V_1^2}} = \sqrt{\frac{V_{rms}^2 - V_0^2 - V_1^2}{V_1^2}} \tag{3.4}$$

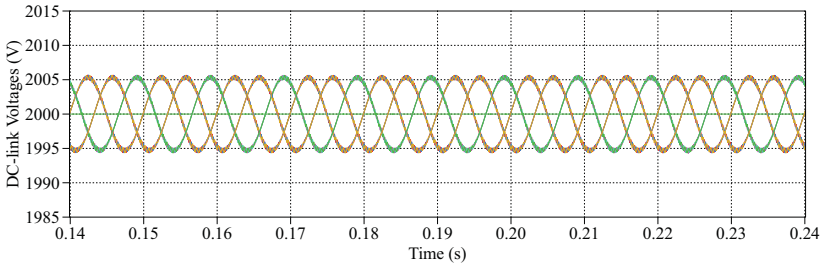

Figure 3.24. Nine DC-link voltages of the CHB converter (steady-state)

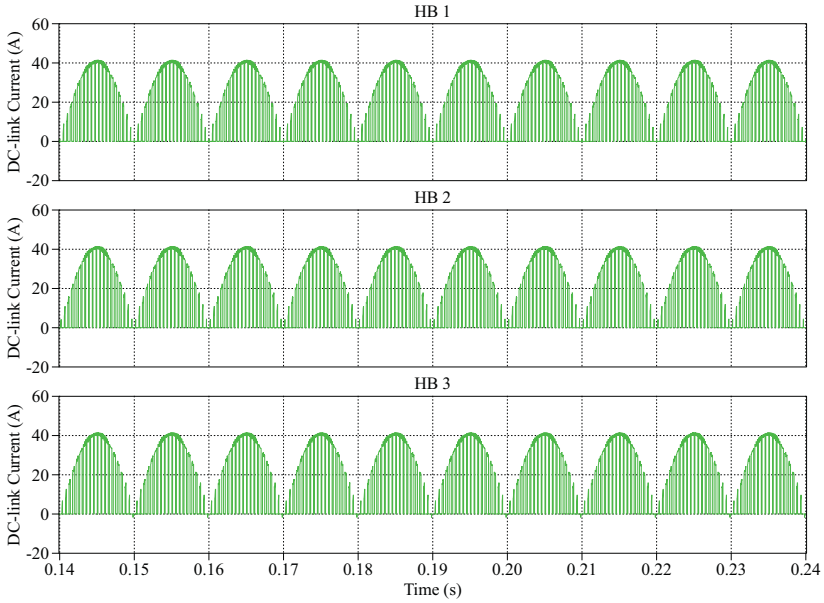

Figure 3.25. Three DC-link currents in one phase of the CHB converter (steady-state)

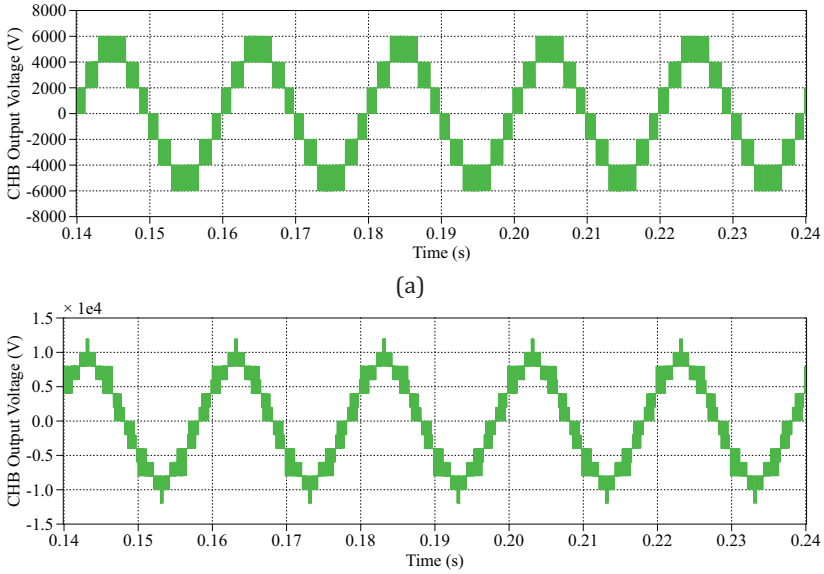

(a)

(b)

Figure 3.26. CHB output voltage (steady-state): (a) phase voltage, (b) line-to-line voltage

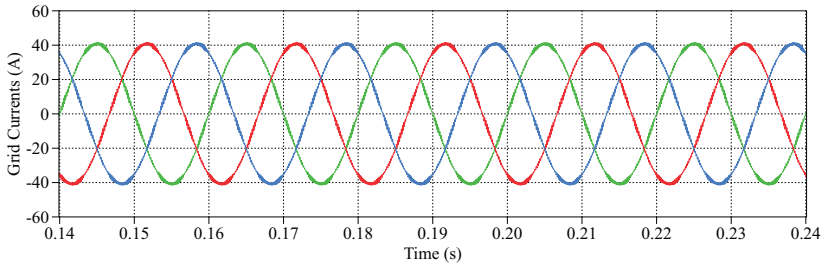

Figure 3.27. Three-phase grid currents (steady-state)

B. The Power Test

In order to evaluate the system performance under power varying conditions, changes in the DC source output currents are imposed on the converter system. The total system power supply variations are shown in Fig. 3.28. It changes from 90% of the rated power to the full power and then to 80% of the rated power. The output currents of the DC sources follow this power reference accordingly. As shown in Fig. 3.29, the output of the DC source (of one H-bridge) changes with a ramp under the variations in the power reference, in order to avoid sudden changes in the controller references. Fig. 3.30 and Fig. 3.31 show the I_d and I_q components of the system, respectively. It can be seen that the current controllers are able to regulate the I_d and I_q components according to power changes fast and accurately. Specifically, Fig. 3.30 shows that the I_d component of the system is regulated following the power reference and varies from 36.7 A to 40.8 A and then to 32.7 A with no significant overshoot (about 0.01 p.u.) and very small steady-state ripples (less than 0.01 p.u.). Fig. 3.31 shows that the I_q component is always regulated to around 0 with a fluctuation between ± 1 A. The V_d and V_q signals generated by the current controllers are shown in Fig. 3.32. The three-phase voltage referencing signals transformed from the V_d and V_q signals are shown in Fig. 3.33. It can be seen that the voltage controller is able to maintain the average of the nine DC-link voltages (measured through a 100 Hz moving-average filter) at 2 kV level, as shown in Fig. 3.34. Through DC voltage balancing algorithm, the modulation indices generated from the three-phase referencing signals for each of the H-bridges are shown in Fig. 3.35. The modulation indices goes to the PS-PWM modulator and generate the switching signals for the CHB converter.

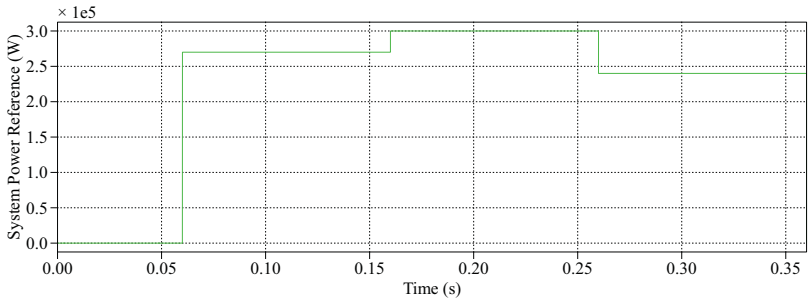

Figure 3.28. Power supply variation profile

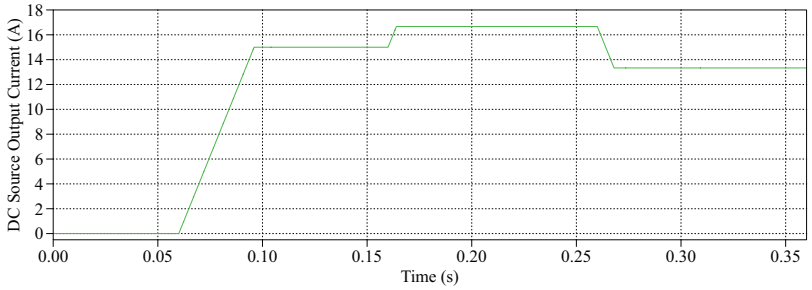

Figure 3.29. DC source output current variation profile

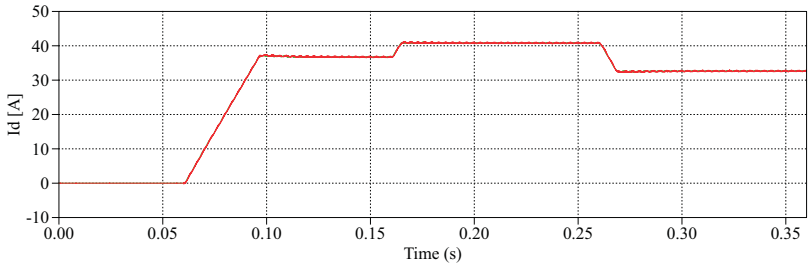

Figure 3.30. I_d component

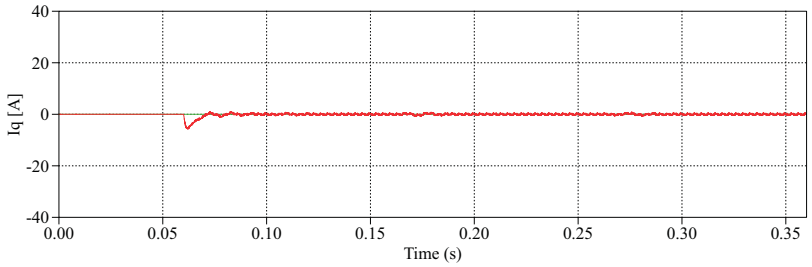

Figure 3.31. I_q component

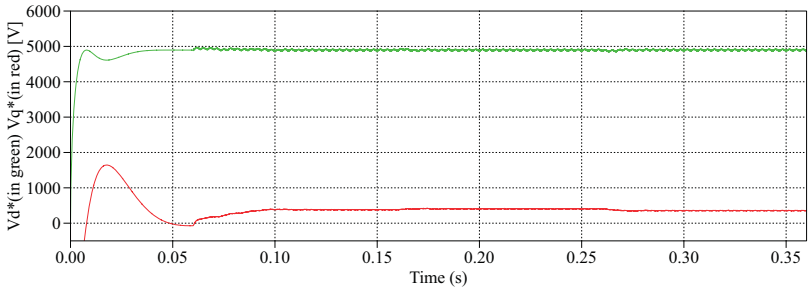

Figure 3.32. V_d and V_q control signals

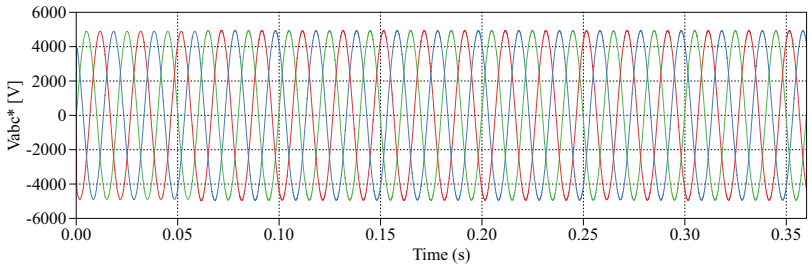

Figure 3.33. Three-phase voltage referencing signals

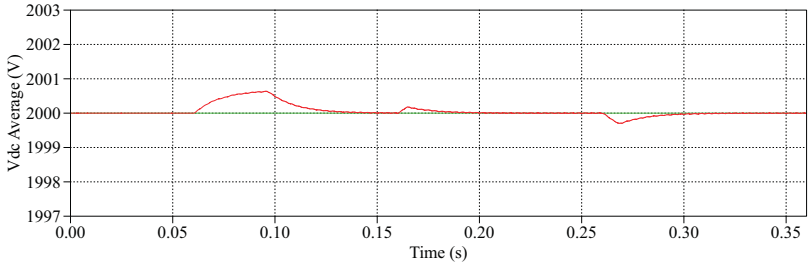

Figure 3.34. Average DC-link voltage

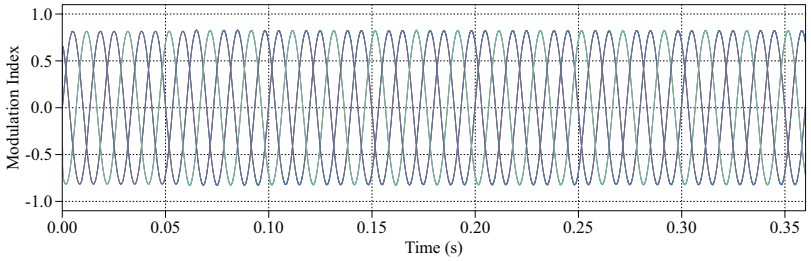

Figure 3.35. Modulation index

The CHB output phase voltage generated under the PS-PWM scheme is shown in Fig. 3.36. It contains 7 levels with no significant drift on each level of the voltage. Fig. 3.37 shows the DC-link currents of the three H-bridges in phase A. They all have a sinusoidal profile with the mean value varying from 15 A to 16.6 A and then to 13.3 A. Fig. 3.38 shows the DC-link voltages during the power variation. The DC voltages are well balanced and maintained at 2 kV level with a fluctuation less than 0.03 p.u. during the whole process. Fig. 3.39 shows the grid currents. The grid currents are regulated in good quality during the variations. The THD values of the grid currents at 90% of the rated power, the full power and 80% of the rated power are 2.97%, 2.68% and 3.34%, respectively. It can be seen that the less the power coming from the DC sources, the smaller the ripples on DC-link voltages and the amplitude of the grid currents, and meanwhile the THD of the grid currents becomes more significant.

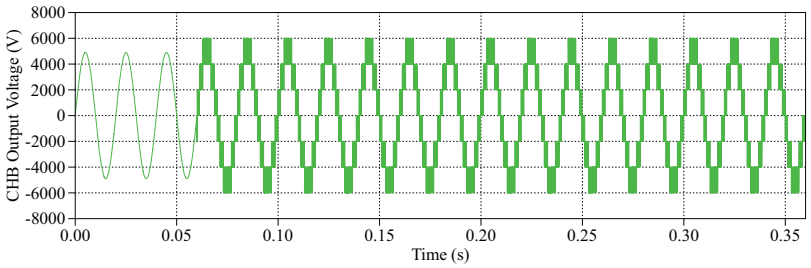

Figure 3.36. Output phase voltage of the CHB converter

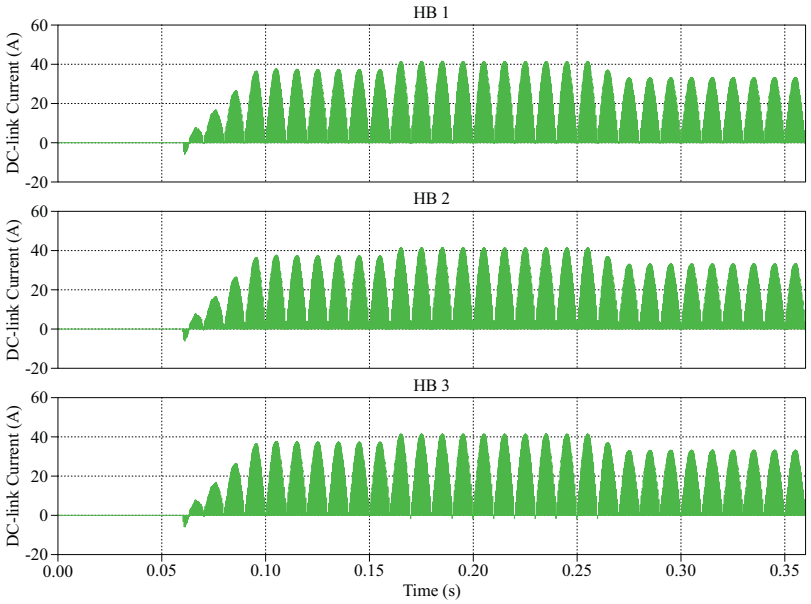

Figure 3.37. Three DC-link currents in one phase of the CHB converter

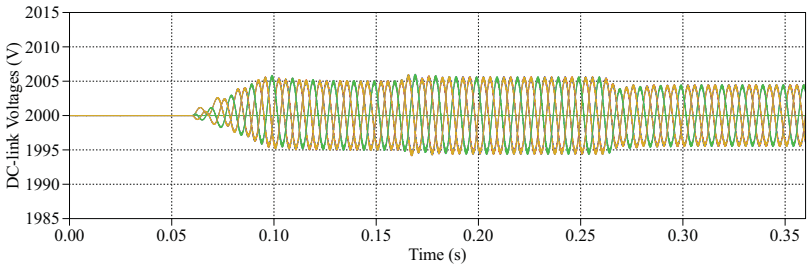

Figure 3.38. Nine DC-link voltages of the CHB converter

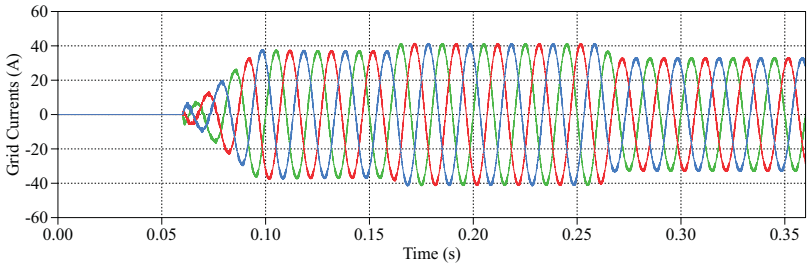

Figure 3.39. Three-phase grid currents

3.5.2.2 3 MW System

The parameters used for the simulation are listed in Table 3.6

A. The Steady-state

The nine DC-link voltages shown in Fig. 3.40 are well balanced and maintained at 2 kV level with a less than 0.03 p.u. fluctuation. The three DC-link currents of converter phase A shown in Fig. 3.41 are distributed evenly among the H-bridges with a mean value of 166.6 A. The phase output voltage of the converter shown in Fig. 3.42 is composed of seven voltage levels and the voltage steps form near sinusoidal shaped waveform. The three-phase grid currents shown in Fig. 3.43 are sinusoidal with a THD of 3.03%. Note that the 300 kW system uses a switching frequency of 1000 Hz to achieve a THD under 3% in the grid currents. When a switching frequency of 500 Hz is used in the 300 kW system, the grid currents have a THD of 5.45% and larger ripples appear on the control signals.

Compared with the 300 kW system, the harmonic components in the grid currents of the 3 MW system are relatively low with respect to the fundamental components. By increasing the power rating of the system to 3 MW, the proportion of the harmonic components in the grid currents is largely reduced and thus a lower switching frequency can be used to achieve low distortion in the grid currents. Moreover, in the 3 MW system a much smaller inductor is used as the converter output filter. This is due to the fact that the size of the filter is usually determined by the base impedance of the converter system, and normally the filter size should not exceed 10% of the base impedance in common practice. Since the power rating of the system is increased by 10 times and the grid voltage remains the same, the base impedance of the 3 MW system is one tenth of its value in the 300 kW system. Therefore the filter inductor size can be much smaller in the 3 MW system.

With a reduced switching frequency, the switching frequency harmonics shift to the side-

Table 3.6. Simulation parameters - The CHB converter with DC current sources (3 MW)

CHB Converter		Grid	
DC-link Voltage	2 kV	Grid Voltage (line-line RMS)	6 kV
Switching Frequency	500 Hz	Fundamental Frequency	50 Hz
Rated Power	3 MW	Grid Impedance	R_g =1.5mΩ L_g =48μH
DC-link Capacitor	5 mF	Grid-side Filter	3.8 mH
PI Parameters			
Current Loop		Voltage Loop	
K_p =20	K_i =5000	K_p =10	K_i =1500
DC Voltage Balancing		K_p =10	

band of 3 kHz in the 3 MW system instead of 6 kHz in the 300 kW system. Although some glitches can be seen on the grid currents waveform, the THD remains low because the amplitude of the fundamental component is relatively large and the proportion of the harmonic components is relatively small. The effect of the reduced switching frequency can also be observed on the DC-link voltage and current waveforms as shown in Fig. 3.40 and Fig. 3.41. The glitches on the DC voltages are more significant in this case. Despite this, lower switching frequency helps reduce the switching losses of the system and a smaller inductor is also easier to control.

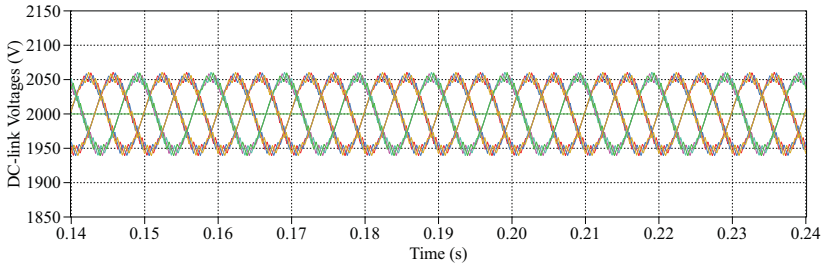

Figure 3.40. Nine DC-link voltages of the CHB converter (steady-state)

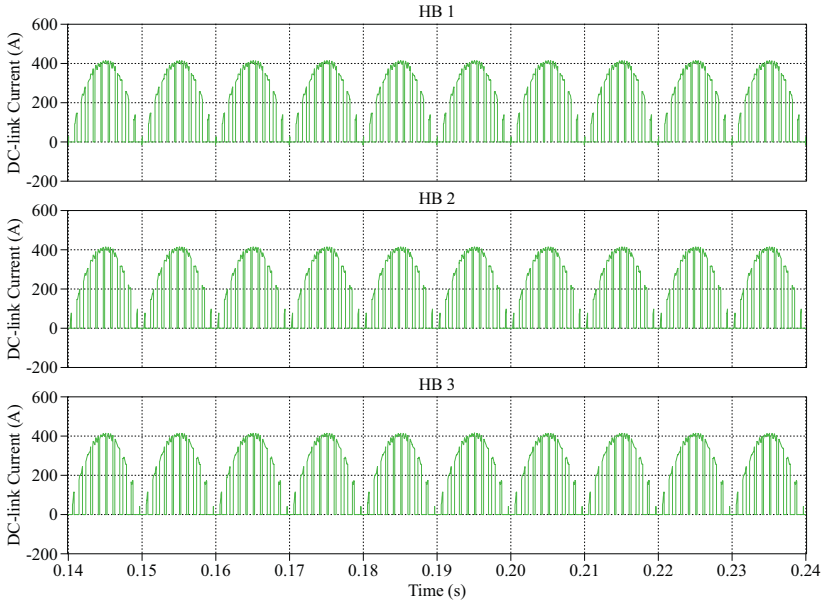

Figure 3.41. Three DC-link currents in one phase of the CHB converter (steady-state)

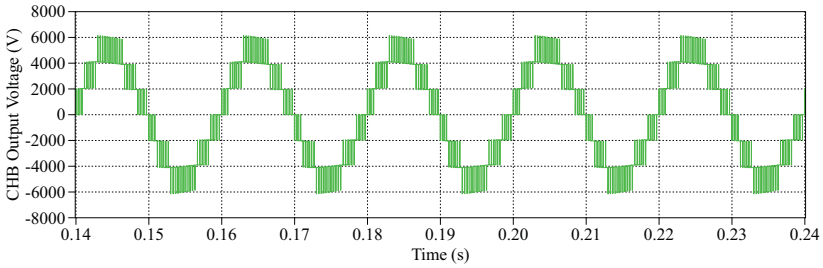

Figure 3.42. Output phase voltage of the CHB converter (steady-state)

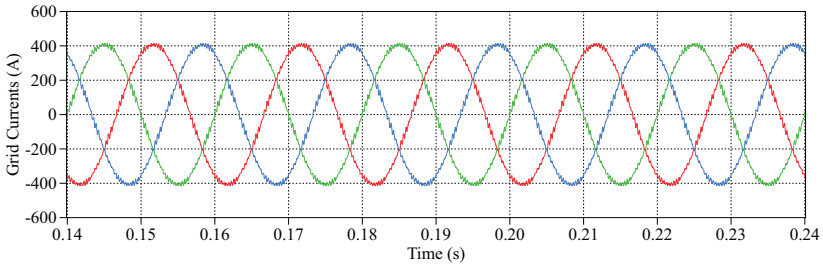

Figure 3.43. Three-phase grid currents (steady-state)

B. The Power Test

Following the power supply variations as shown in Fig. 3.44 and the subsequent variations of the DC source output current shown in Fig. 3.45, the responses of the current controllers and voltage controller of the 3 MW system are shown from Fig. 3.46 to Fig. 3.51. As the power rating is 10 times that of the 300 kW system, a smaller inductor is used as the grid-side filter and the parameters of the controllers are largely reduced. Meanwhile, the switching frequency has been reduced from 1 kHz to 500 Hz. Although the ripples on the control signals are seemingly larger, the controllers are capable of performing fast and accurate tracking of the varying references. Specifically, Fig. 3.46 shows that the I_d component of the system is regulated following the power reference and varies from 367.4 A to 408.2 A and then to 326.6 A with no significant overshoot (less than 0.05 p.u.) and small steady-state ripples (less than 0.03 p.u.). The I_q component, as shown in Fig. 3.47 is always regulated to around 0 with a fluctuation between $\pm$15 A.

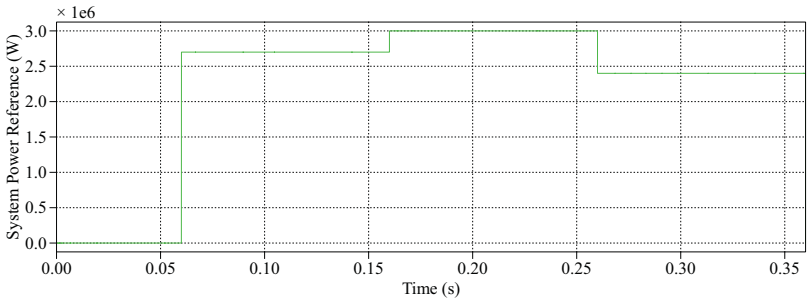

Figure 3.44. Power supply variation profile

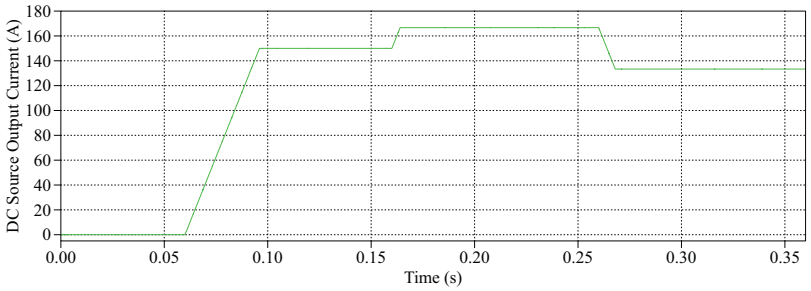

Figure 3.45. DC source output current variation profile

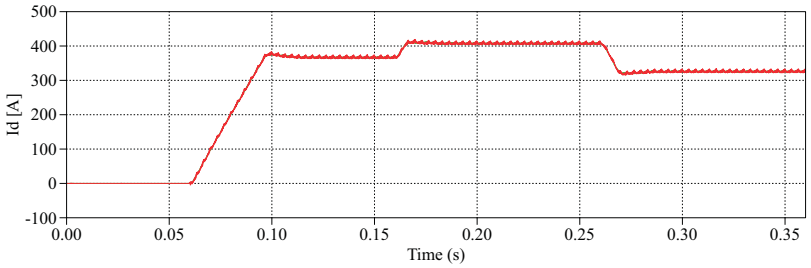

Figure 3.46. I_d component

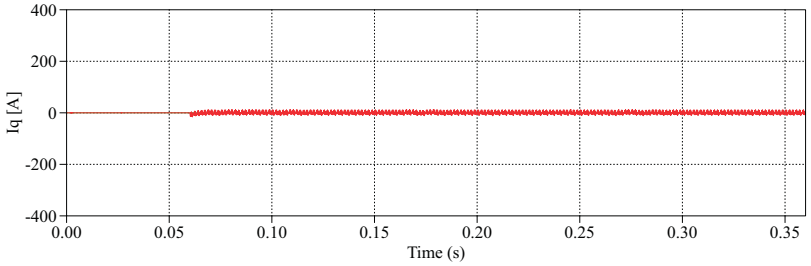

Figure 3.47. I_q component

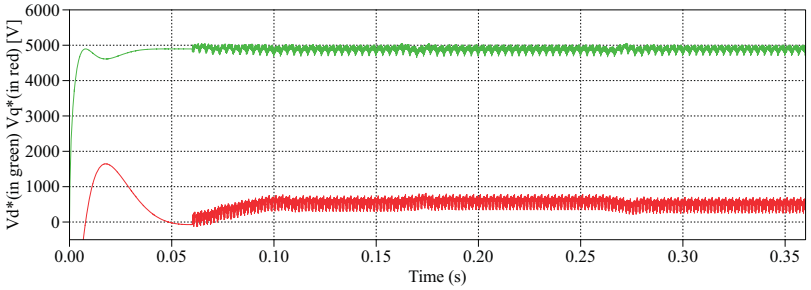

Figure 3.48. V_d and V_q control signals

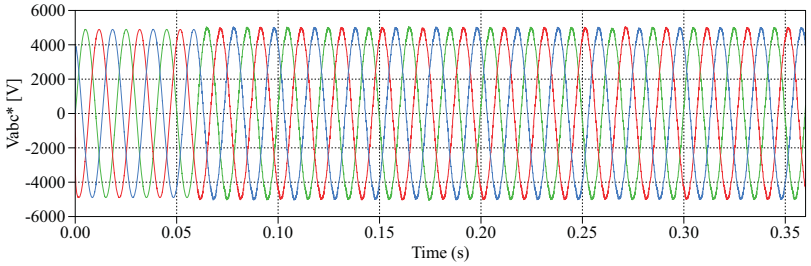

Figure 3.49. Three-phase voltage referencing signals

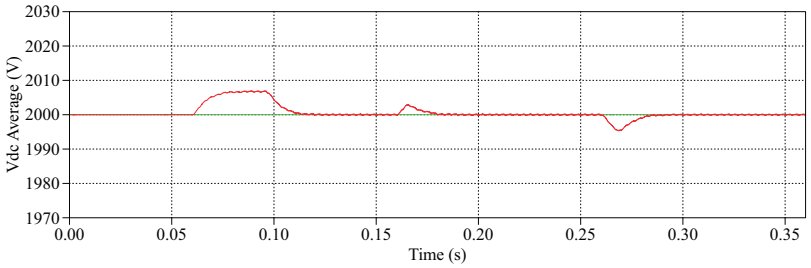

Figure 3.50. Average DC-link voltage

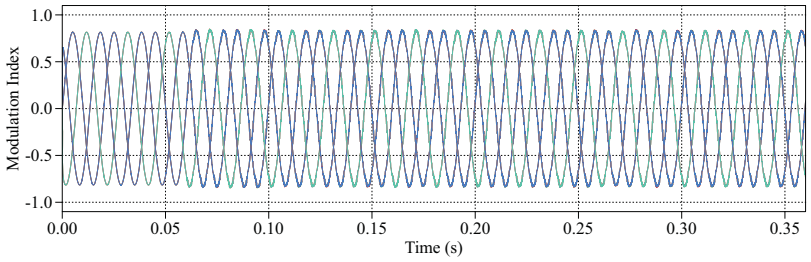

Figure 3.51. Modulation index

The system performance can be observed from Fig. 3.52 to Fig. 3.55. Drift on the output CHB voltages becomes obvious since the rated power of the system is much higher and a reduced switching frequency has been used compared to the 300 kW system. The mean value of DC-link currents varies from 150 A to 166.6 A and then to 133 A. The ripples on the DC-link voltages are bigger in amplitude as the grid currents increase by ten times. However, the fluctuation of the DC-link voltages remains under 0.03 p.u. and the grid currents are regulated in good quality during the whole process. The THD values of the grid currents at 90% of the rated power, the full power and 80% of the rated power are 3.36%, 3.03% and 3.79%, respectively.

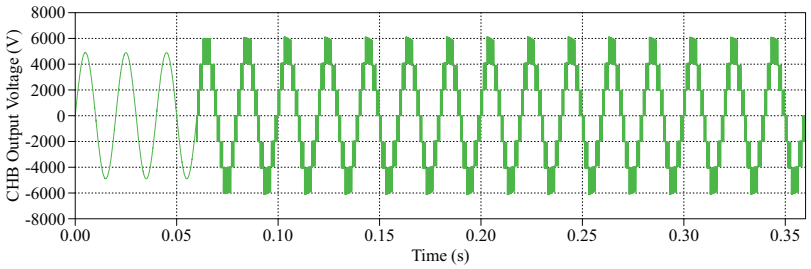

Figure 3.52. Output phase voltage of the CHB converter

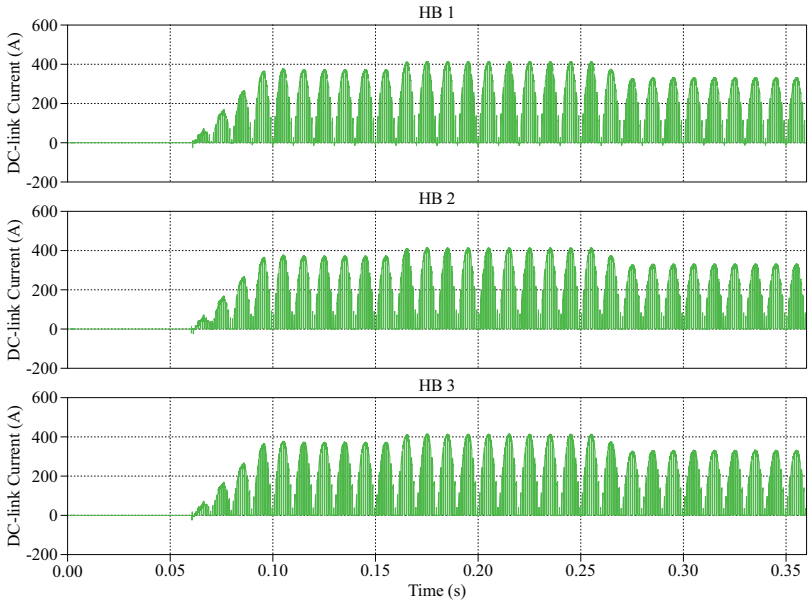

Figure 3.53. Three DC-link currents in one phase of the CHB converter

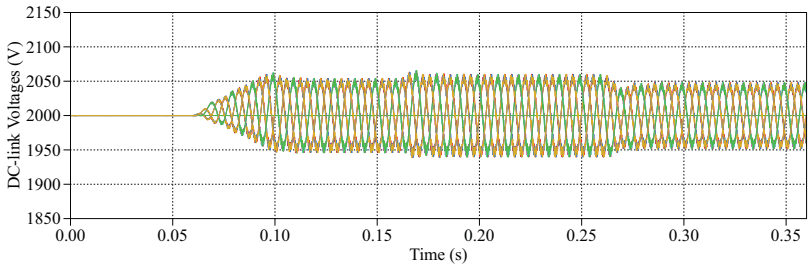

Figure 3.54. Nine DC-link voltages of the CHB converter

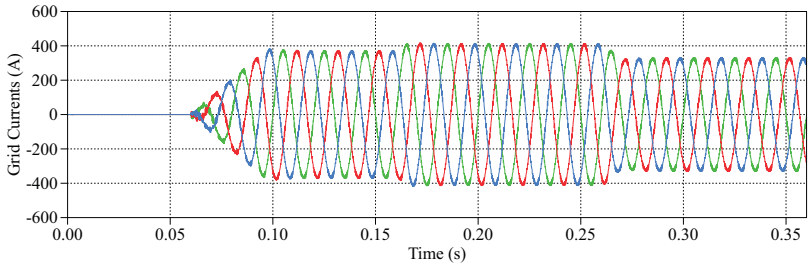

Figure 3.55. Three-phase grid currents

3.5.3 CHB Converter with Higher Number of Levels

From the study of the 7-level CHB converter in the last section, it can be seen that although the 7-level converter is capable of integrating 3 MW of power to the grid, it has some difficulties to achieve equally good power quality as with 300 kW power, especially on the grid currents THD performance. Considering that higher power and voltage capabilities can be achieved by the vertical extension of the CHB converter, the performance of a 13-level CHB converter is investigated in this section. The number of series connected H-bridges in each converter phase is doubled in this topology. Two control approaches, the VOC in the synchronous frame with PI controllers and the VOC in the stationary frame with PR controllers, are applied in the converter system. The performance of the controllers will be evaluated and discussed.

The parameters used for the simulation are listed in Table 3.7. The circuit structure of the 13-L CHB grid-connected converter fed with DC current sources is shown in Fig. 3.56. The control diagram of the system is shown in Fig. 3.57(a) and Fig. 3.57(b) for the synchronous frame VOC and the stationary frame VOC respectively.

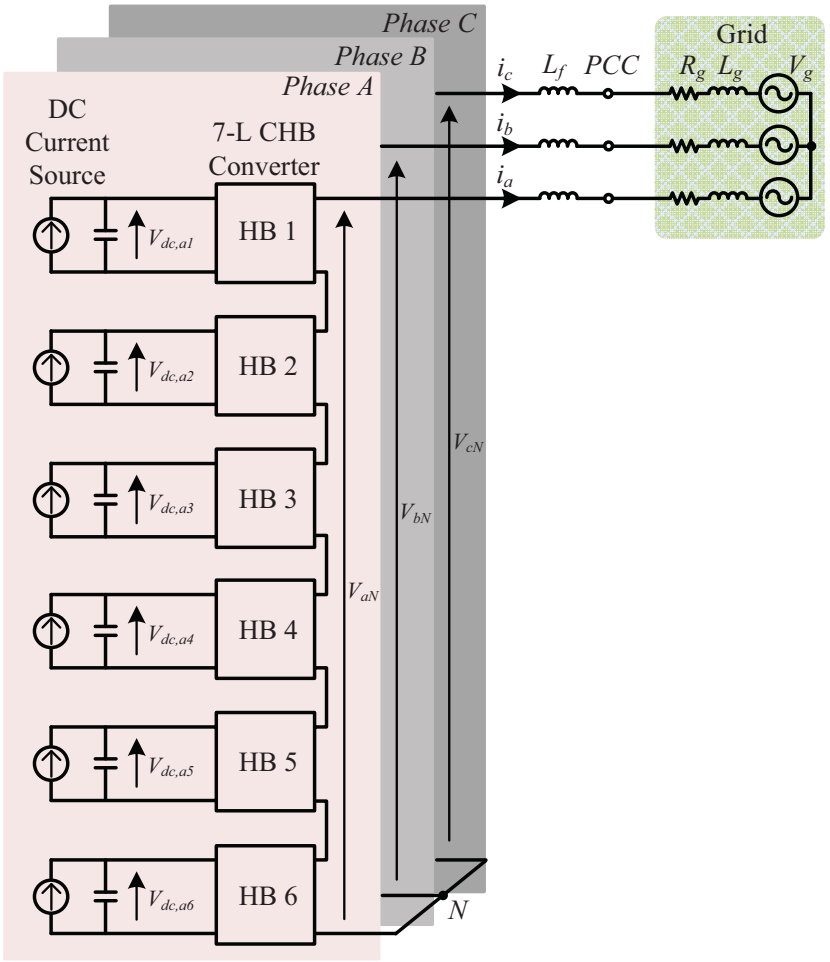

Figure 3.56. 13-L CHB converter fed with DC current sources

Variations in the power supply have been imposed on the system. The power supply reference is shown in Fig. 3.58 and the profile of the resulted DC source output current at each

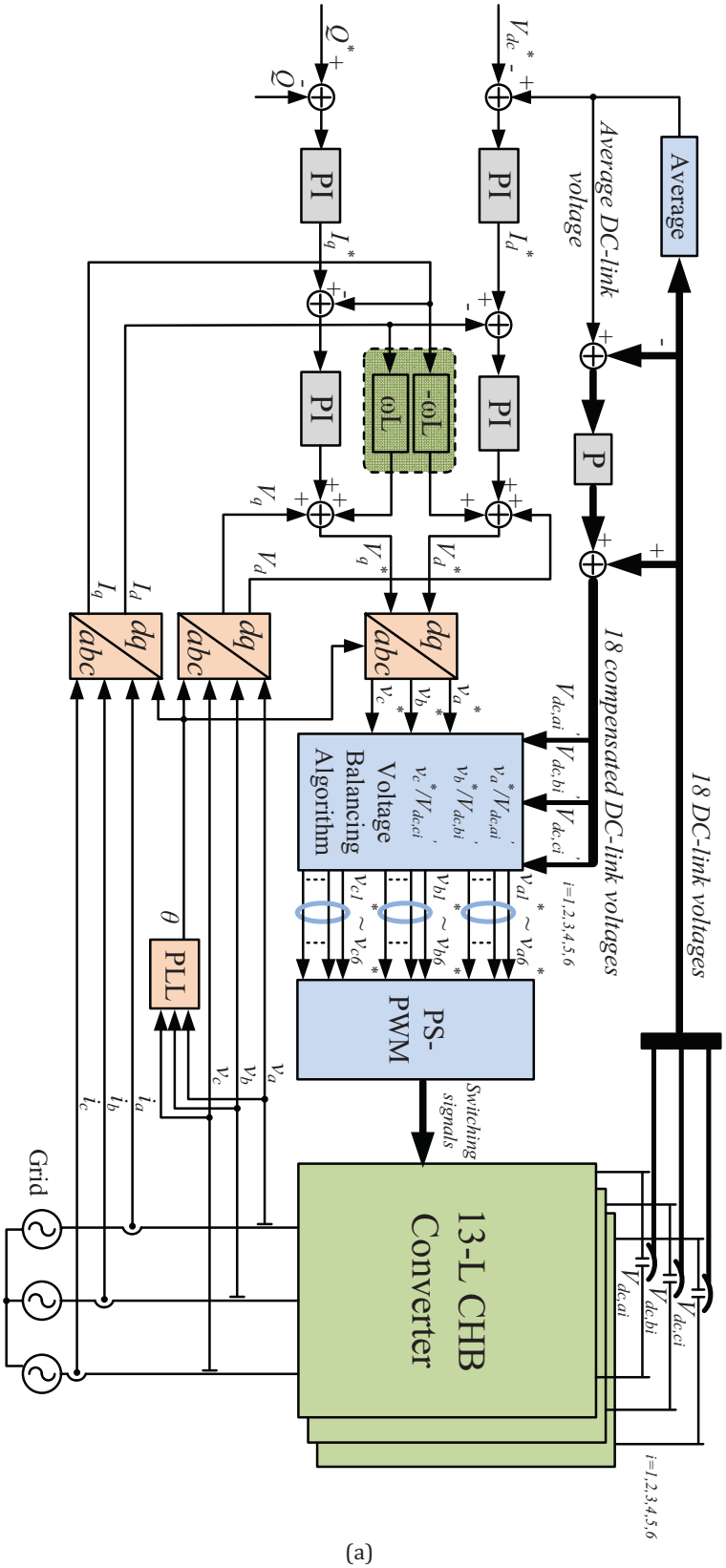

(a)

Figure 3.57. Control diagram of the 13-L CHB converter: (a) synchronous frame VOC (cont.)

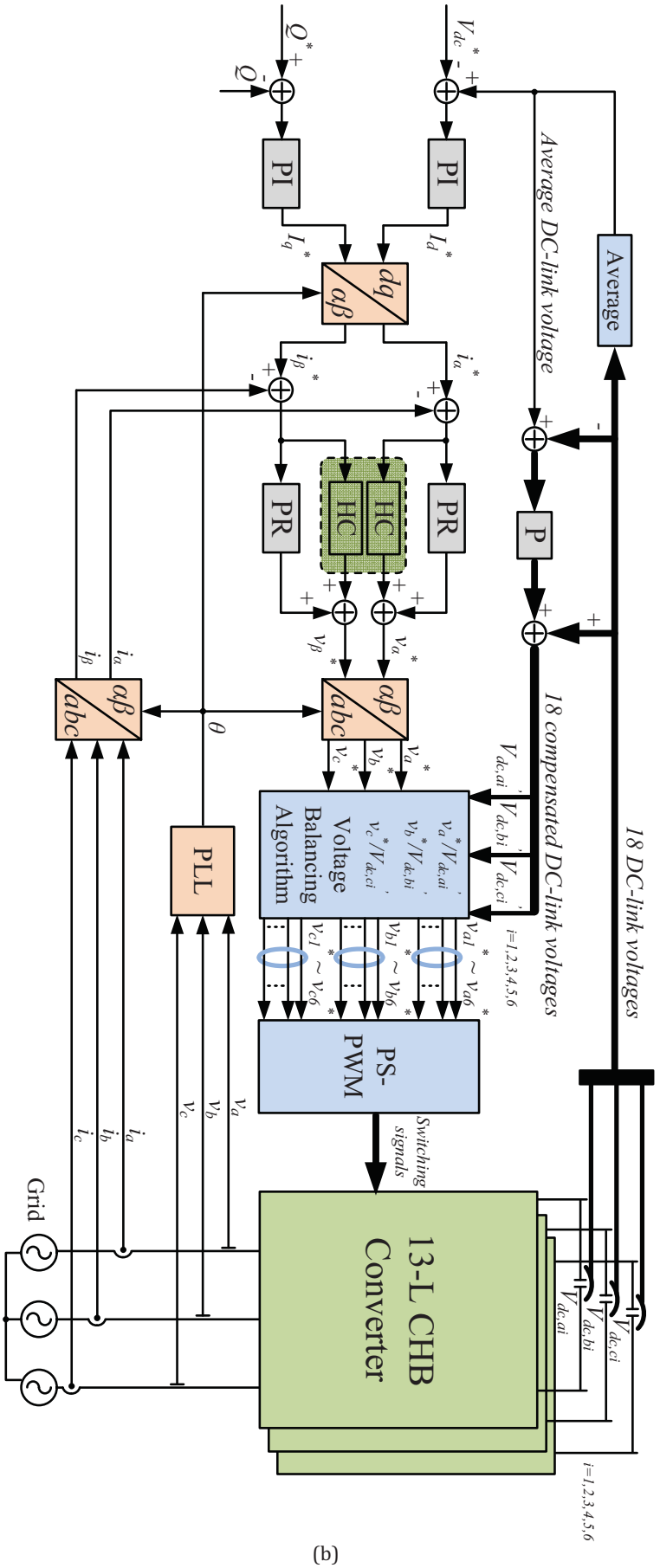

(b)

Figure 3.57. Control diagram of the 13-L CHB converter: (b) stationary frame VOC

Table 3.7. Simulation parameters - The CHB converter with higher number of levels

CHB Converter		Grid	
DC-link Voltage	1.5 kV	Grid Voltage (line-line RMS)	10 kV
Switching Frequency	500 Hz	Fundamental Frequency	50 Hz
Rated Power	3 MW	Grid Impedance	R_g =1.5 mΩ L_g = 48 μH
DC-link Capacitor	5 mF	Grid-side Filter	3 mH

H-bridge is shown in Fig. 3.59. During this process, the performance of the controllers and the system inputs and outputs are observed and analyzed.

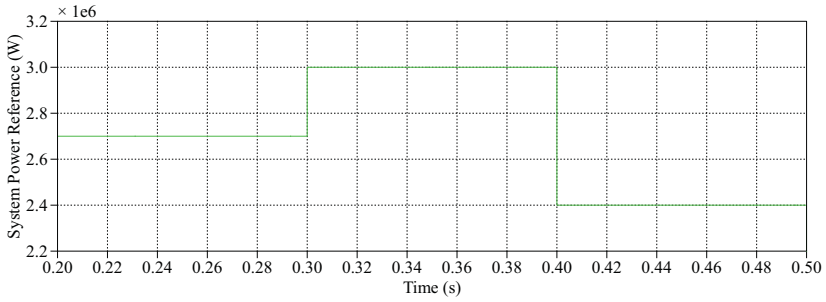

Figure 3.58. Power supply variation profile

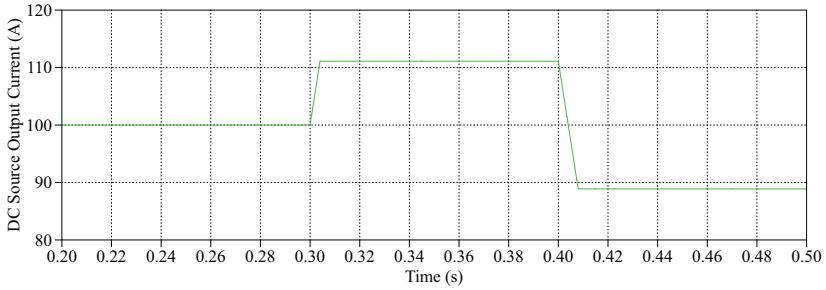

Figure 3.59. DC source output current variation profile

3.5.3.1 Synchronous Frame VOC with PI Controllers

The waveforms of the PI controllers and the converter are shown from Fig. 3.60-Fig. 3.69. The I_d and I_q waveforms are shown in Fig. 3.60 and Fig. 3.61. Both I_d and I_q components are regulated according to the power changes and the response of the PI current controllers are fast and accurate. The V_d and V_q signals generated from the PI current controllers are shown in Fig. 3.62. The three-phase voltage references transformed from the V_d and V_q signals are shown in Fig. 3.63. The PI voltage controller is able to maintain the average of the DC-link voltages at 2 kV (as shown in Fig. 3.64) and provide accurate I_d reference signals for the inner PI current controllers. Through the DC voltage balancing algorithm, the modulation indices

for the CHB converter generated from the three-phase voltage references are shown in Fig. 3.65.

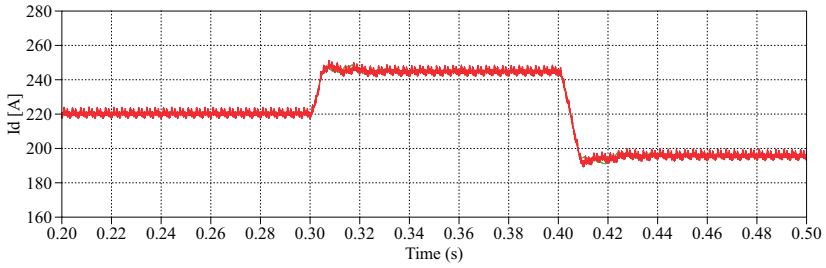

Figure 3.60. I_d component

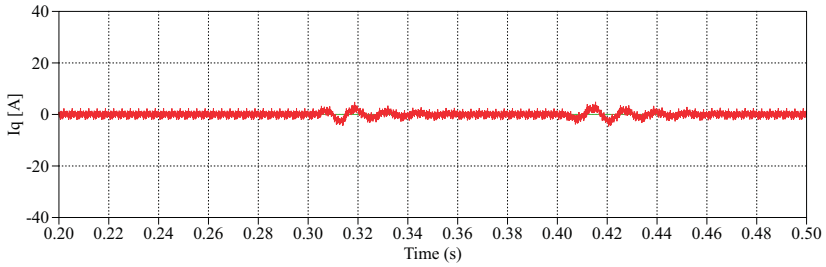

Figure 3.61. I_q component

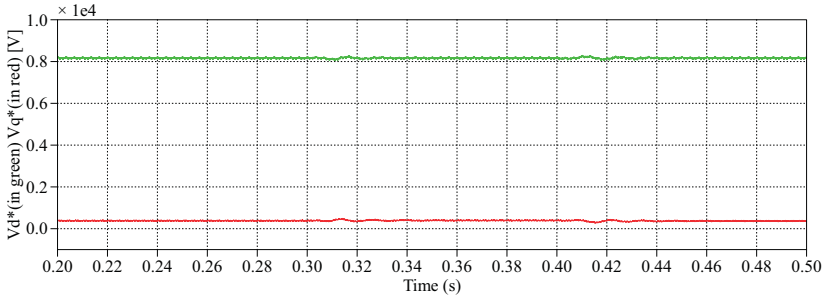

Figure 3.62. V_d and V_q control signals

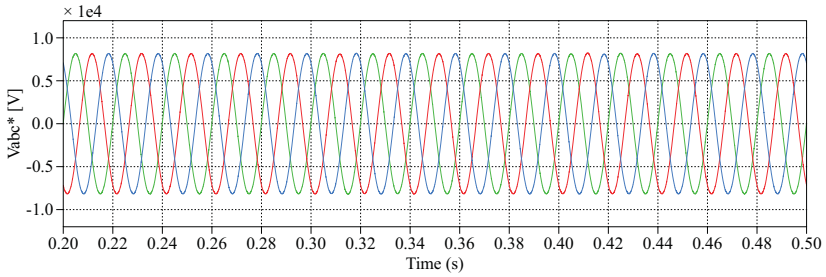

Figure 3.63. Three-phase voltage referencing signals

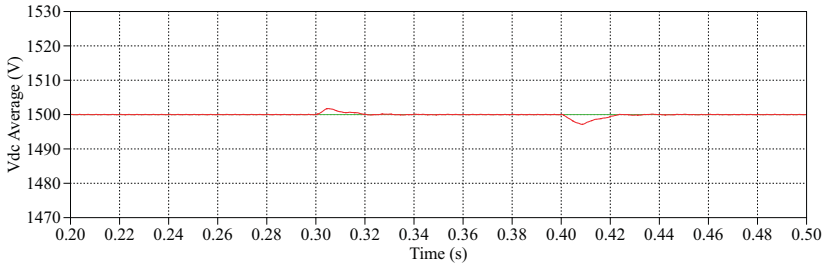

Figure 3.64. Average DC-link voltage

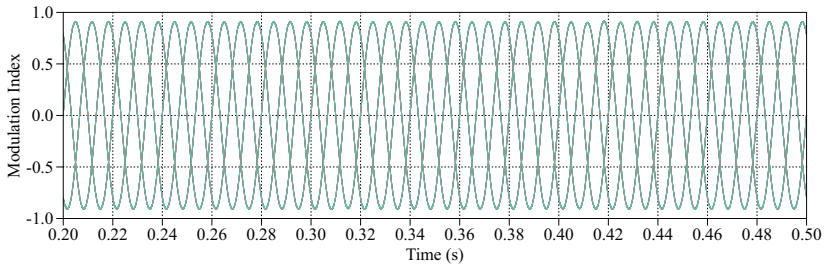

Figure 3.65. Modulation index

The 18 DC-link voltages during the power test are shown in Fig. 3.66. They are well balanced and maintained at 1.5 kV with less than 0.03 p.u. fluctuation in steady-state. The DC-link currents of the six H-bridges in phase A are shown in Fig. 3.67. They have sinusoidal profile and the mean value changes along with the variation of the power supply. The phase output voltage of the CHB converter is shown in Fig. 3.68. It is composed of 13 voltage levels and the stepped waveform is close to sinusoidal. The three-phase grid currents are shown in Fig. 3.69. They are in good sinusoidal shape with the THD under 3% during the whole process.

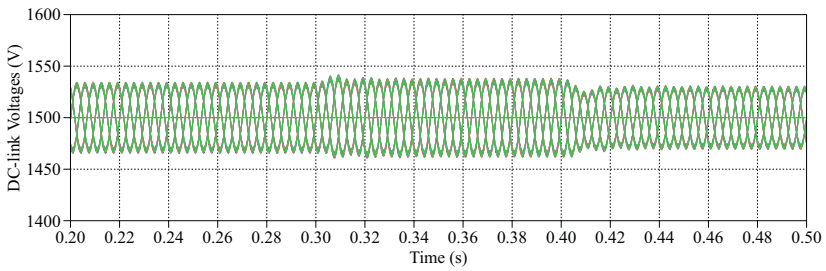

Figure 3.66. Eighteen DC-link voltages of the 13-L CHB converter

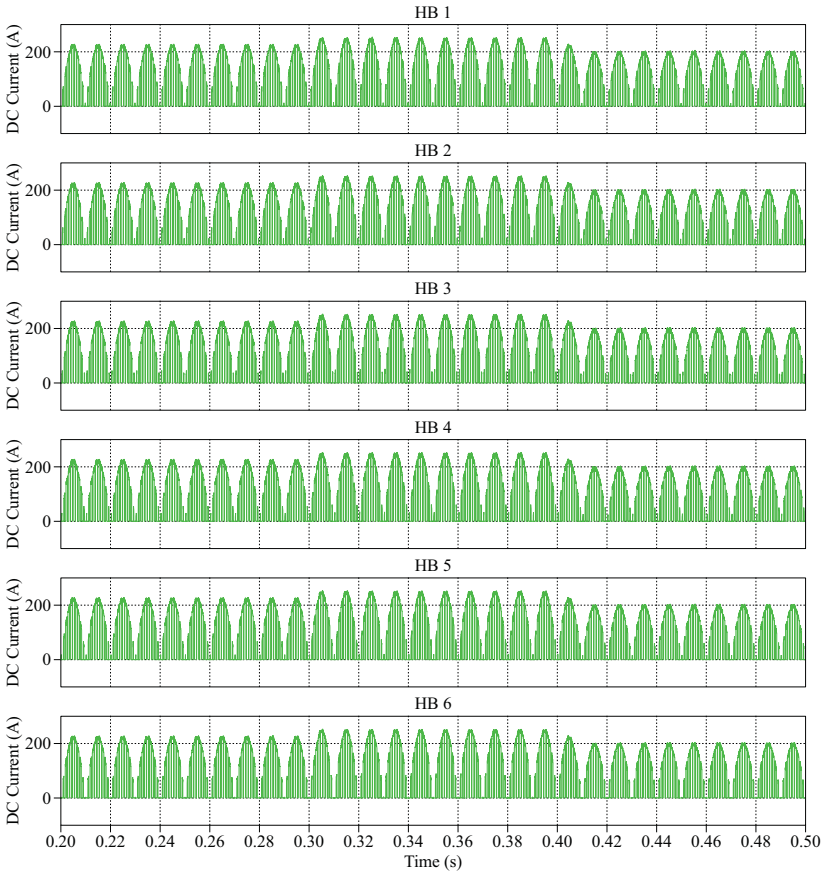

Figure 3.67. Six DC-link currents in one phase of the 13-L CHB converter

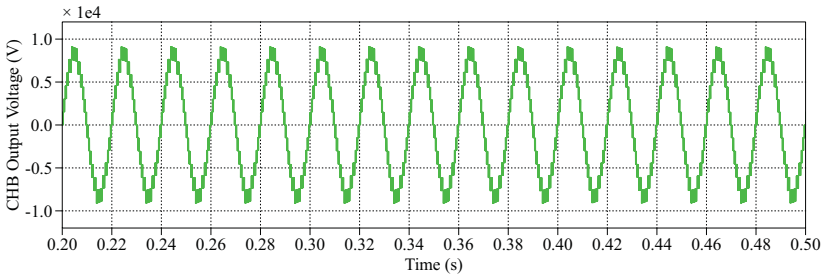

Figure 3.68. Output phase voltage of the 13-L CHB converter

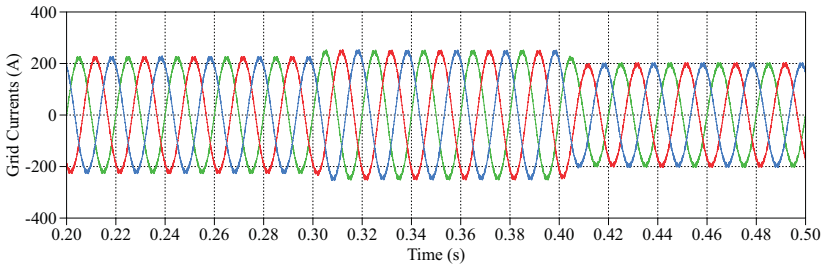

Figure 3.69. Three-phase grid currents

3.5.3.2 Stationary Frame VOC with PR Controllers

The waveforms of the PR controllers and the converter are shown from Fig. 3.70-Fig. 3.79. The i_α and i_β waveforms are shown in Fig. 3.70 and Fig. 3.71. Both i_α and i_β components are regulated according to the power changes and the response of the PR current controllers are fast and accurate. The v_α and v_β signals generated from the PR current controllers are shown in Fig. 3.72. They are sinusoidal and steady in shape. The three-phase voltage references transformed from the v_α and v_β signals are shown in Fig. 3.73. The PI voltage controller is able to maintain the average of the DC-link voltages at 2 kV (as shown in Fig. 3.74) and provide accurate I_d reference signal which is used to derive i_α and i_β reference signals for the inner PR current controllers. Through the DC voltage balancing algorithm, the modulation indices for the CHB converter generated from the three-phase voltage references are shown in Fig. 3.75.

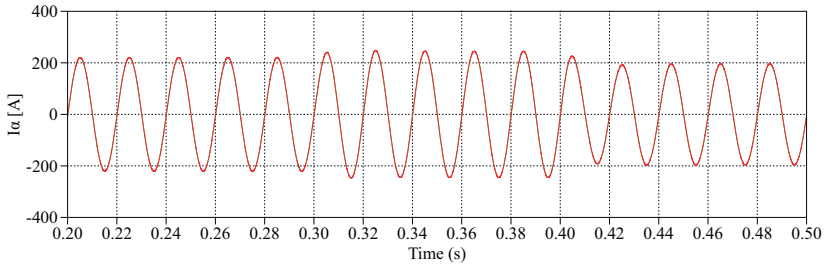

Figure 3.70. i_α component

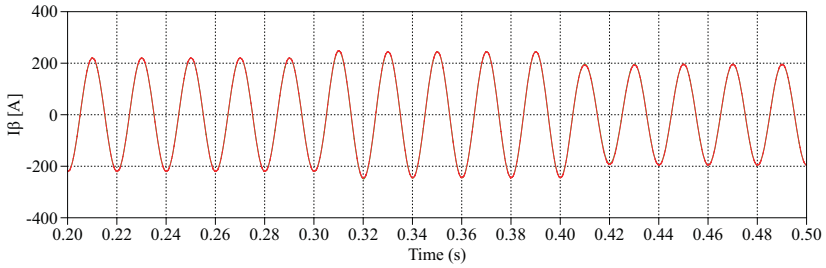

Figure 3.71. i_β component

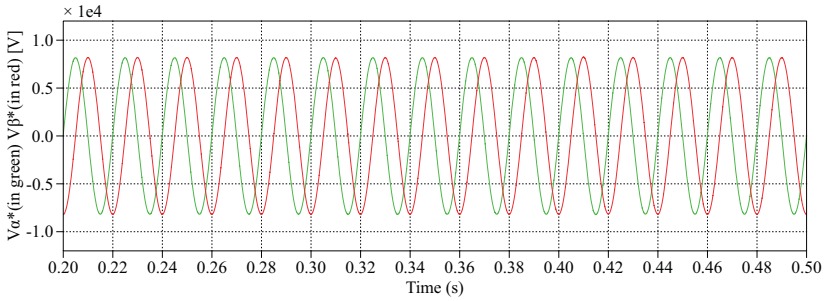

Figure 3.72. v_α and v_β control signals

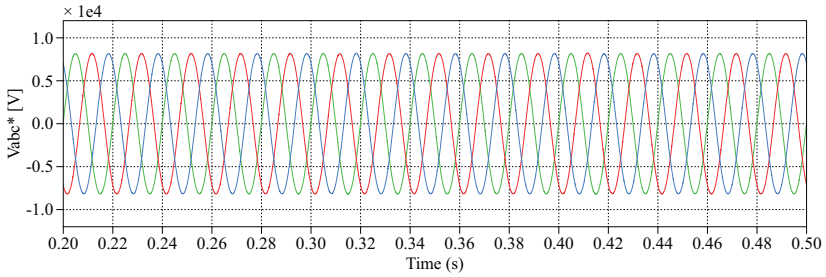

Figure 3.73. Three-phase voltage referencing signals

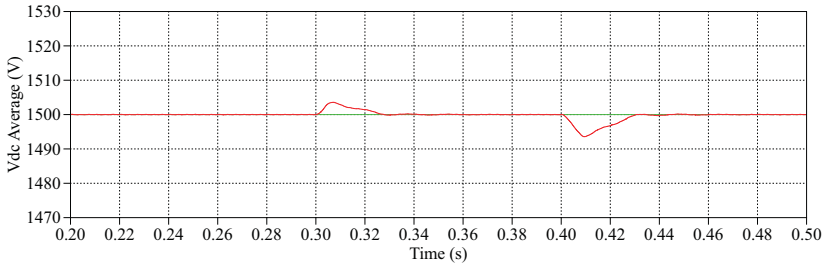

Figure 3.74. Average DC-link voltage

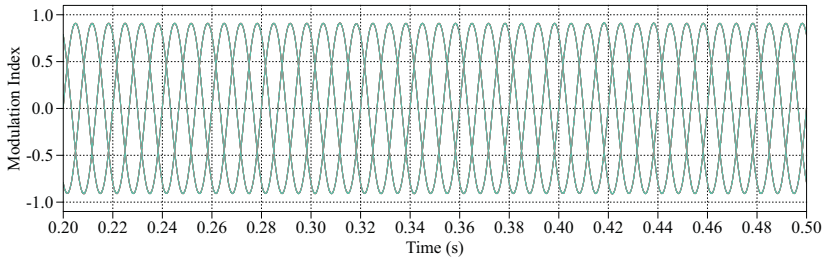

Figure 3.75. Modulation index

The 18 DC-link voltages during the power test are shown in Fig. 3.76. They are well balanced and maintained at 1.5 kV with less than 0.03 p.u. fluctuation in steady-state. The DC-link currents of the six H-bridges in phase A are shown in Fig. 3.77. Each DC-link current has a sinusoidal profile and the mean value changes along with the variation of the power supply. The phase output voltage of the CHB converter is shown in Fig. 3.78. It is composed of 13 voltage levels and the stepped waveform is close to sinusoidal. The grid currents are shown in Fig. 3.79. They are sinusoidal with the THD under 3% during the whole process. The waveforms do not have a significant difference from those under the dq frame. Both the PI and PR controllers under the synchronous frame and the stationary frame, respectively, are capable of fulfilling the system control tasks and provide accurate control signals with fast responses under power supply variations.

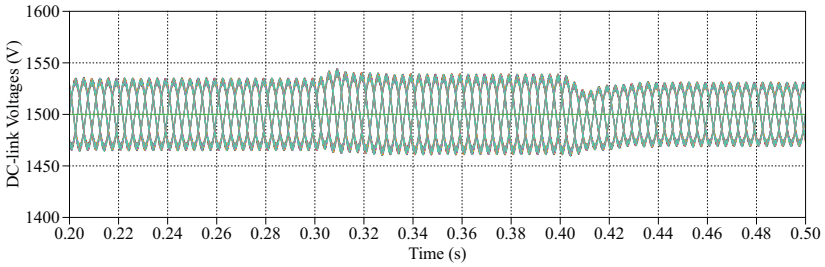

Figure 3.76. Eighteen DC-link voltages of the 13-L CHB converter

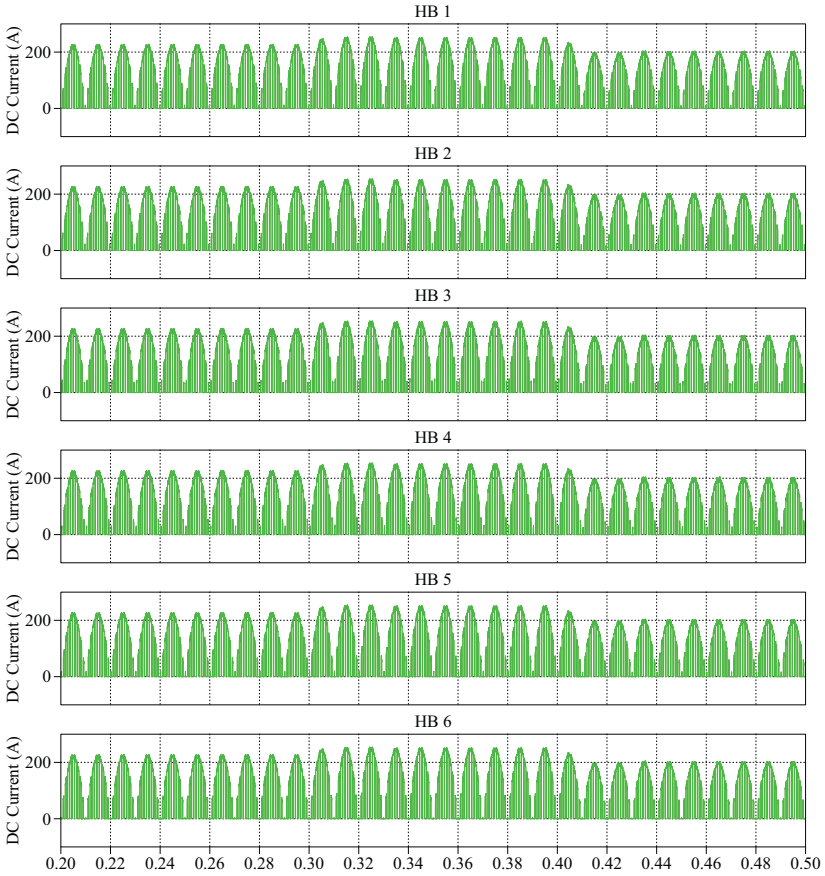

Figure 3.77. Six DC-link currents in one phase of the 13-L CHB converter

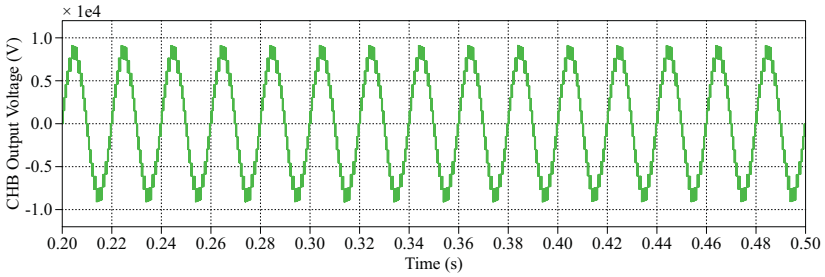

Figure 3.78. Output phase voltage of the 13-L CHB converter

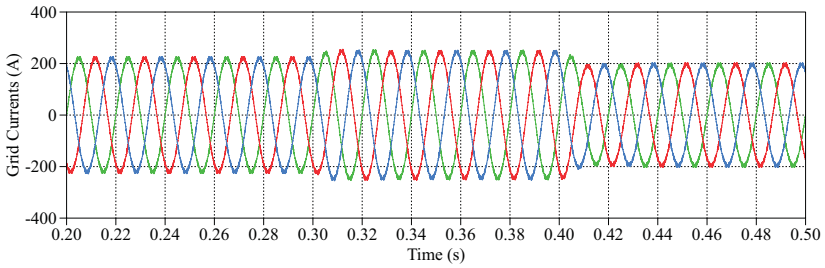

Figure 3.79. Three-phase grid currents

Chapter 4

Isolated DC/DC Converters

4.1 Introduction

The cascaded H-bridge multilevel topology for large-scale PV power systems requires isolated DC sources to feed the H-bridges. The galvanic isolation is preferred at the DC-side and meanwhile MPPT for the PV arrays needs to be achieved by the implementation of DC/DC converters. Therefore isolated DC/DC converters are introduced into the CHB converter system for the solar PV integration to the grid. Two isolated DC/DC topologies, namely the flyback and the boost-half-bridge (BHB), are discussed in this chapter.

4.1.1 Flyback Converter

The flyback converter is an isolated DC/DC topology derived from the buck-boost converter. It provides a simple implementation with small component count and it is widely used in low-power switch-mode power supplies. It can be used to provide isolation on the DC-side of the grid-connected inverter topologies for low-power PV applications [16]. It has also been proposed as a candidate topology for the DC/DC stage of large-scale PV systems based on the CHB converter [94]. The configuration of the flyback topology is given in Fig. 4.1(a).

The voltage transfer ratio, which is the converter gain, depends on the power switch duty ratio and transformer turns ratio, as shown in (4.1).

$$\frac{V_{out}}{V_{in}} = \frac{D}{1-D}\frac{N_s}{N_p} \tag{4.1}$$

4.1.2 Boost-half-bridge (BHB) Converter

The topology of the BHB converter is shown in Fig. 4.1(b). It consists of a boost chopper, a half-bridge inverting circuit, a high-frequency transformer, and a voltage-doubler rectifying circuit [76]. There is an inductor filter L, two power switches S_U and S_L with two split capacitors C_{IU} and C_{IL} at the input; a voltage-doubler diode bridge composed of D_U and D_L, with two capacitors C_{OU} and C_{OL}, at the output; and a high-frequency transformer providing the isolation between the input and the output of the converter. The BHB converter has several special features: a) small input filter size due to the continuous input current; b) ZVS

(zero-voltage switching) turn-on of the power switches realized by utilization of the leakage inductor L_k; c) ZCS (zero-current switching) turn-off of the rectifier diodes achieved through natural commutation during the operation of the converter; d) wide input voltage range due to the wide operational duty cycle range. The converter gain is determined by (4.2), with D being the duty ratio of the upper switch S_U.

$$\frac{V_{out}}{V_{in}} = \frac{1}{1-D}\frac{N_s}{N_p} \tag{4.2}$$

The BHB converter can be used as the building block of multiphase DC/DC converters [77], as shown in Fig. 4.1(c). Multiphase DC/DC converters are constructed by connecting the BHB cell and the voltage-doubler at the primary and secondary of the high-frequency transformer following certain patterns. The resulting converter has the advantages of reduced voltage and current ratings of the power devices by series and parallel connections, reduced size of the input and output filters by interleaved switching, and reduced turns ratio of the step-up transformer, given that the total rated power remains constant. On the other hand, the multiphase DC/DC converter is suitable for high-voltage high-power applications by stacking the power cells in series and parallel. Additionally, the interleaved structure accommodates the modularity and flexibility of PV power systems, especially with multilevel converters such as the cascaded H-bridge converter, which also has a modular structure.

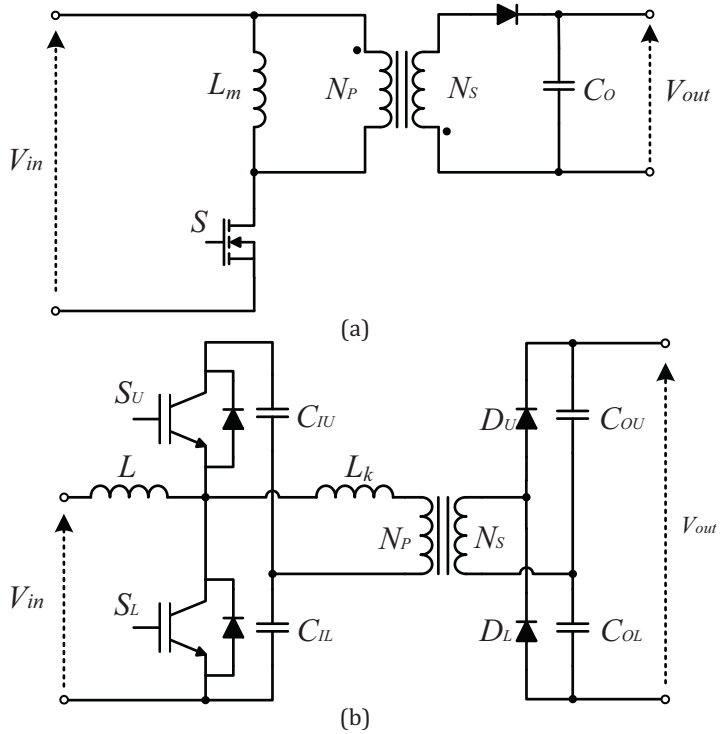

Figure 4.1. Isolated DC/DC topologies: (a) flyback, (b) boost half-bridge (BHB) (cont.)

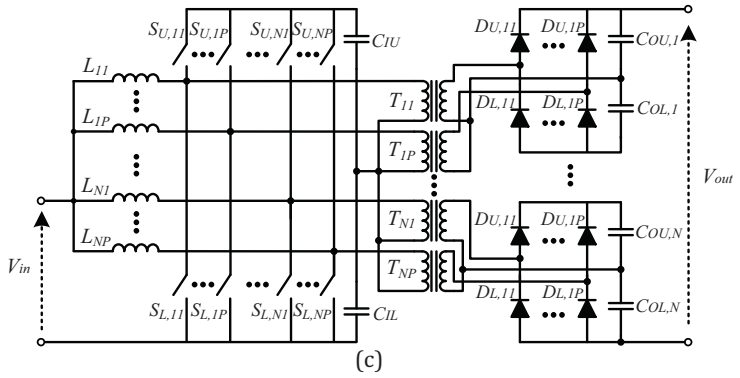

(c)

Figure 4.1. Isolated DC/DC topologies: (c) multiphase DC/DC

4.2 MPPT Algorithms

Solar PV energy supply has an intermittent nature. The output of the PV modules is highly dependent on the environmental conditions, particularly the solar irradiance and the ambient temperature. The power extracted from the PV sources is also subject to other factors such as shading, mismatch, cabling, soiling and so on. Solutions for the associated technical issues aim at the improvement of PV cell efficiency, maximum power harvesting techniques and the optimization of the solar PV system structure to maximize the energy yield under various conditions [78].

The current-voltage (I-V) and power-voltage (P-V) characteristics of a PV cell are shown in Fig. 4.2 [79]. It can be seen that the output power reaches maximum at a particular operating point of the PV cell under certain irradiance and temperature. The variations of the I-V curve of a PV cell under different irradiance and temperature conditions are shown in Fig. 4.3(a) and Fig. 4.3(b), respectively [79]. The MPP of the PV module changes with irradiance and temperature. Specifically, the PV output current is largely reduced under decreasing irradiance while the PV output voltage is only slightly affected by this matter. On the other hand, the PV output voltage varies in a relatively large range when the temperature changes while the PV output current is not very sensitive to this factor. Therefore, a proper algorithm to calculate and track the MPP of the PV module under different environmental conditions is essential to PV systems in order to obtain the optimal energy yield. A switch-mode power converter, which performs this algorithm and maintains the PV module's operating point at MPP regardless of the load, serves as an MPP tracker.

A number of MPPT algorithms have been proposed so far, such as the perturb and observe (P&O), incremental conductance (INC), constant voltage (CV), pilot cell and parasitic capacitance (PC) method, to name a few [80]. The first two are the most commonly used methods and are discussed in the following sections.

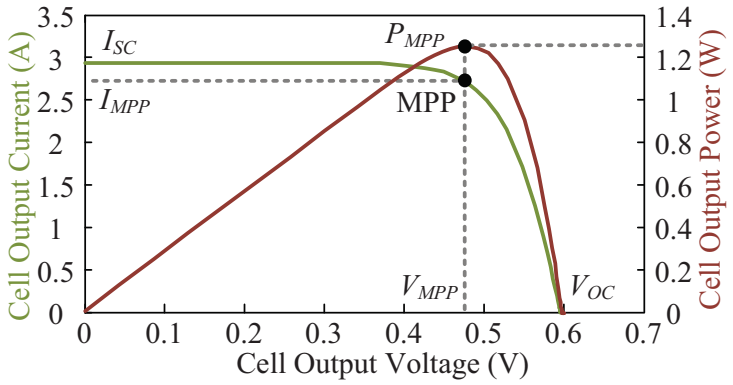

Figure 4.2. I-V and P-V characteristics of a PV cell

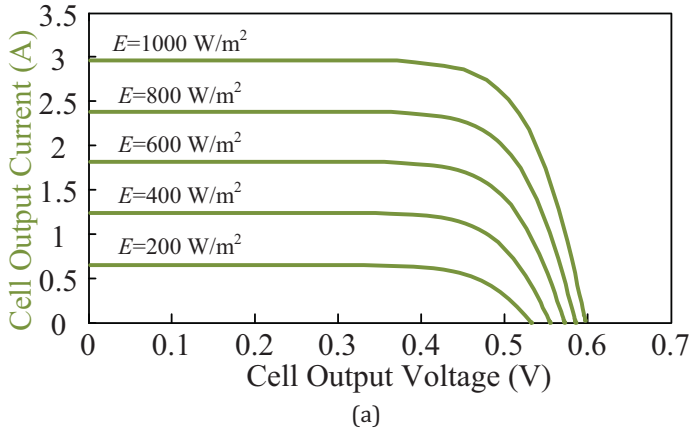

(a)

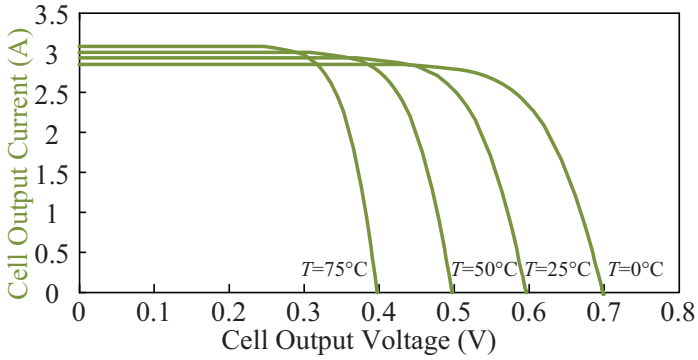

(b)

Figure 4.3. Effects of atmospheric factors on the PV cell energy yield: (a) Influence of solar irradiance (b) Temperature dependence

4.2.1 Perturb and Observe (P&O)

The perturb and observe (P&O) is by far the most popular MPPT algorithm in practice [80]. In this algorithm, the operating voltage of the PV module is perturbed by a small increment, and the resulting change in power, ΔP, is measured. If this ΔP is positive, it means that the perturbation of the operating voltage has moved the PV module's operating point towards its MPP at this particular irradiance and temperature condition. Further perturbations in the same directions will follow subsequently in order to approach the MPP. The principle of this algorithm is illustrated in Fig. 4.4.

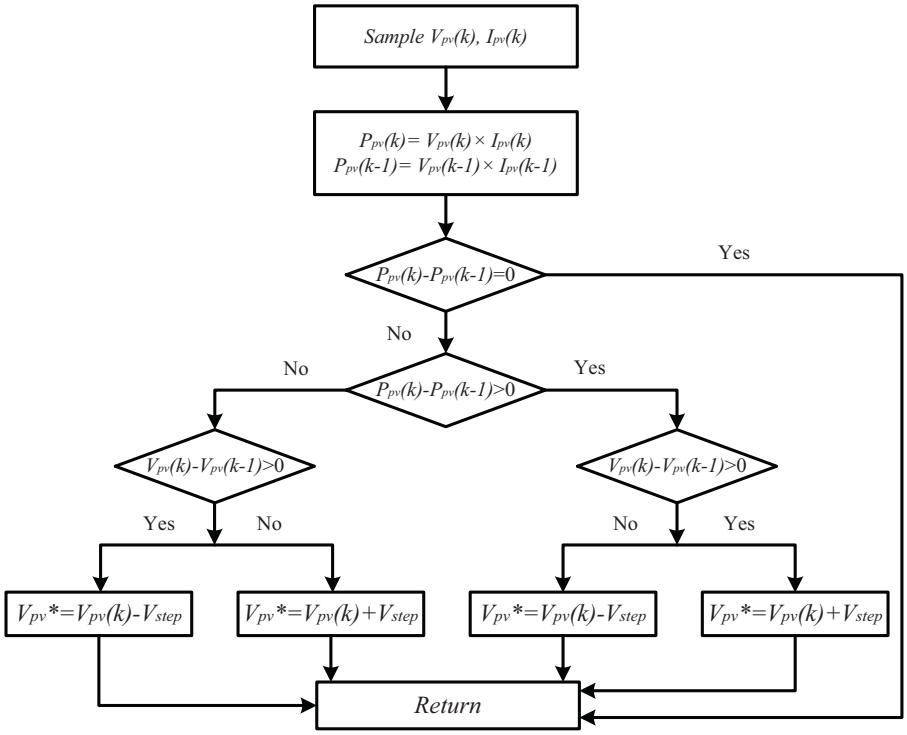

Figure 4.4. Flowchart of the perturb and observe (P&O) algorithm

The advantage of the P&O algorithm is its simplicity and easy to approach; the disadvantage is that it has limited accuracy [37]. Firstly, the P&O cannot locate the exact MPP. Instead, it oscillates around the MPP, altering the sign of the perturbation with each ΔP measurement. Secondly, since the P-V curve flattens with decreasing solar irradiance, it is difficult to discern the location of the MPP due to the minor change of power with respect to the perturbation of the voltage. Also, the P&O is likely to exhibit erratic behavior under rapidly changing irradiance levels. This could cause the MPPT to fail under partly clouded conditions. Nevertheless, several improvements have been proposed to address the problems of the P&O. For example, a waiting function, which imposes a momentary cessation of perturbations once its algebraic sign had reversed several times in a row, can be used to reduce the oscillation when a MPP is reached.

4.2.2 Incremental Conductance (INC)

The incremental conductance (INC) algorithm is derived by differentiating the PV power with respect to its voltage and setting the result equal to zero [80], as shown in (4.3).

$$\frac{dP}{dV} = \frac{d(VI)}{dV} = I + V\frac{dI}{dV} = 0. \tag{4.3}$$

Giving (at the MPP),

$$-\frac{I}{V} = \frac{dI}{dV}. \tag{4.4}$$

Note that the left side of (4.4) represents the negative PV instantaneous conductance, and the right side of the equation represents the PV incremental conductance. These two quantities are equal in magnitude while opposite in sign at the MPP. The following set of inequalities can be derived from (4.4) to decide the relationship between the PV operating voltage and the MPP voltage, indicating whether an MPP has been reached. These can be used to determine the direction in wich the next perturbation should occur to move the PV operating point towards the MPP. The perturbation is repeated until (4.4) is satisfied. Once the MPP is achieved, the algorithm continues to operate at this point until a change in current is measured and a new MPP needs to be found.

$$\frac{dI}{dV} = -\frac{I}{V}; \quad (\frac{dP}{dV}) = 0 \tag{4.5.1}$$

$$\frac{dI}{dV} > -\frac{I}{V}; \quad (\frac{dP}{dV}) > 0 \tag{4.5.2}$$

$$\frac{dI}{dV} < -\frac{I}{V}; \quad (\frac{dP}{dV}) < 0 \tag{4.5.3}$$

A flowchart of the algorithm is shown in Fig. 4.5. The present and previous values of the PV array voltage and current are used to calculate the dI and dV. When $dV = 0$ and $dI = 0$, the PV array operates at the MPP and the environmental conditions remains the same. If $dI > 0$ while $dV = 0$, it means that the solar irradiance has increased and the MPP voltage will rise. The algorithm then increases the PV operating voltage in order to track the new MPP. On contrary, if $dI < 0$ when $dV = 0$, it means the solar irradiance has decreased and the PV operating voltage should reduce accordingly to track the new MPP. If $dV \neq 0$, the PV array is not yet at MPP. Equations (4.5.2) and (4.5.3) can be used to determine the direction towards which the voltage should be changed in order to reach MPP. When $dI/dV > -I/V$, which means $dP/dV > 0$, the PV voltage should be increased to move towards MPP. On the contrary, when $dI/dV < -I/V$, which means $dP/dV < 0$, the PV voltage should be dereased in order to reach MPP. This shows the advantage of this method over the P&O, that the INC can actually calculate the direction in which to perturb the PV operating point in order to approach the MPP. Morover, the INC can determine when exactly the PV has reached its MPP without the constant oscillation around the MPP as in the P&O. Thus under rapidly changing weather conditions, the INC is able to track the MPP accurately.

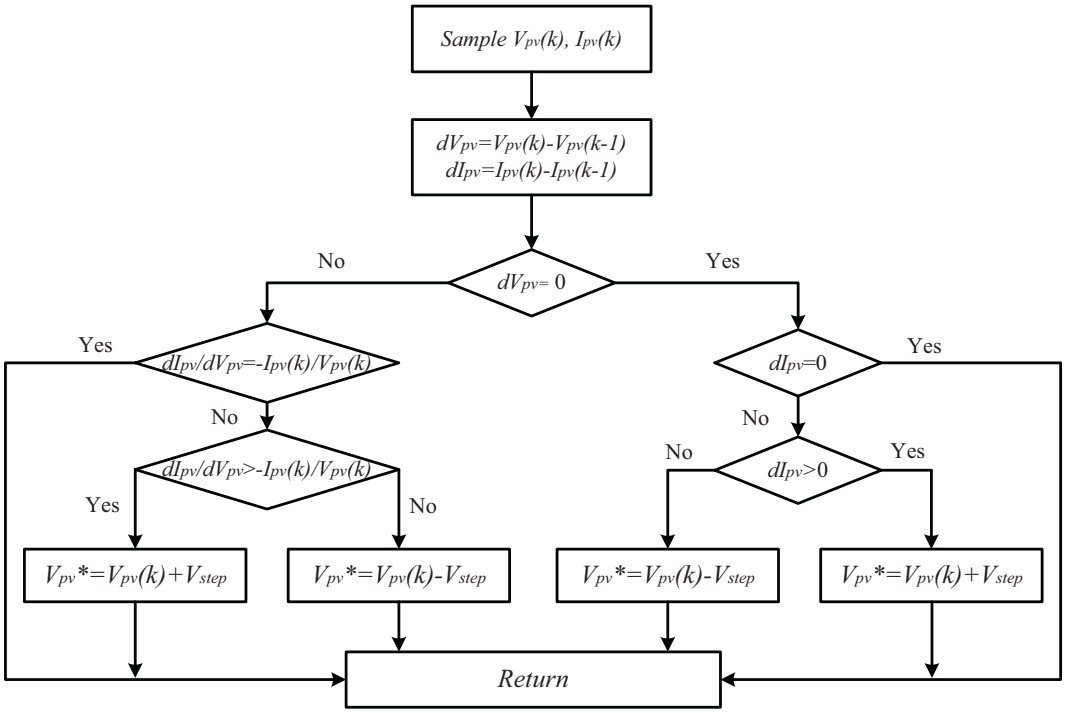

Figure 4.5. Flowchart of the incremental conductance (INC) algorithm

4.3 Simulation Studies of the DC/DC Converters

The simulation of the isolated DC/DC converters, the BHB and the flyback, is performed in MATLAB/Simulink and the PLECS Blockset. The component parameters used for the simulation studies are listed in Table 4.1. The PV array used for both simulation models is composed of 10 parallel connected PV strings; each string is comprised of 45 PV modules connected in series. The model of the PV array is based on the characteristics of the BP365 PV module [81]. This configuration constitutes a 29.25 kW_p PV power system. The control diagram of the DC/DC converter is shown in Fig. 4.6. The PV voltage reference signal V_{pv}^* can be given directly for testing under certain conditions (section 4.3.1 and 4.3.2) or calculated through MPPT algorithms under varying conditions (section 4.3.3).

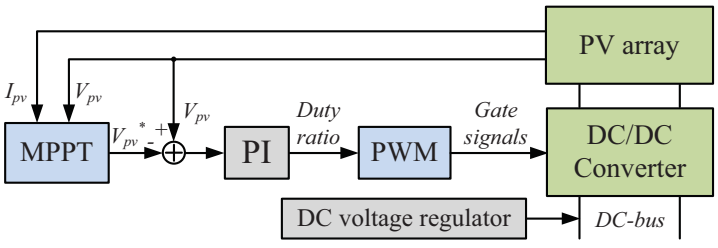

Figure 4.6. Control diagram of the DC/DC converter

Table 4.1. Simulation parameters - Isolated DC/DC converters

PV module (BP 365)		**PV array**	
Maximum Power P_{MPP}	65 W	Maximum Power P_{MPP}	29.25 kW
MPP Voltage V_{MPP}	17.67 V	MPP Voltage V_{MPP}	794.6 V
MPP Current I_{MPP}	3.68 A	MPP Current I_{MPP}	36.8 A
Open circuit voltage V_{OC}	22.04 V	Open circuit voltage V_{OC}	994.5 V

Isolated DC/DC converters		
Converter topology	Boost-half-bridge (BHB)	Flyback
Switching frequency	20 kHz	20 kHz
Input voltage range	450 ~800 V	450 ~800 V
Input inductor	L =1.2 mH, L_k =1 μH	L_m =1.2 mH
Input filter capacitor	C_I =1 mF, $C_{IU} = C_{IL}$ =50 μF	C_I =1 mF
Output capacitor	$C_{OU} = C_{OL}$ =2.5 mF	C_O =1.25 mF
DC-link voltage (V_{dc})	2 kV	2 kV
High-frequency transformer turns ratio ($N_S : N_P$)	1:1	1:1
PI Parameters	K_p =0.01, K_i =17	K_p =0.01, K_i =17

4.3.1 Steady-state Performance

The system is simulated under 1 kW/m^2 solar irradiance and 25°C temperature. The PV output voltage and current waveforms of both converters are shown in Fig. 4.7 and Fig. 4.8 respectively. Both converters are capable of achieving the MPP operation in steady-state under this atmospheric condition. The flyback has a higher fluctuation around the operating point compared with the BHB, indicating the MPPT efficiency difference between the two converters. The PV output current in the BHB topology is directly associated with the input inductor current of the converter and therefore is smooth with smaller ripples. The PV output current in the flyback topology is shaped by several components including the input inductor and output diode due to the working principle of the flyback transformer. Additionally, filter capacitors of the same size are used at the input of both DC/DC converters (in fact integrated with the PV source, thus not shown in the DC/DC converter topologies) in order to smooth the PV output voltage and current. Therefore, although the flyback converter input current is chopped by the switch constantly, the actual PV output current remains continuous, despite the fact that the PV output current ripple in the flyback converter is still larger than that of the BHB converter.

The inductor currents of both converters are shown in Fig. 4.9. The flyback works at a higher range of current than that of the BHB. This is due to the circuit structure. The inductor current in the flyback converter is the sum of converter input current and a fraction of output diode current, while the inductor current in the BHB converter equals to the converter input

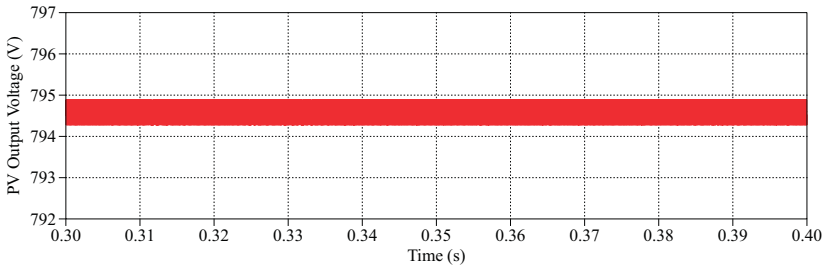

(a)

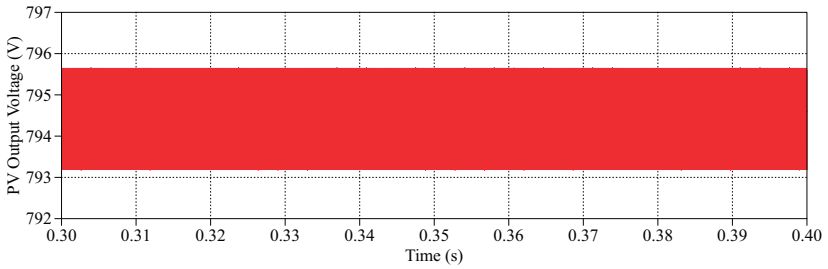

(b)

Figure 4.7. Steady-state PV voltage: (a) BHB, (b) flyback

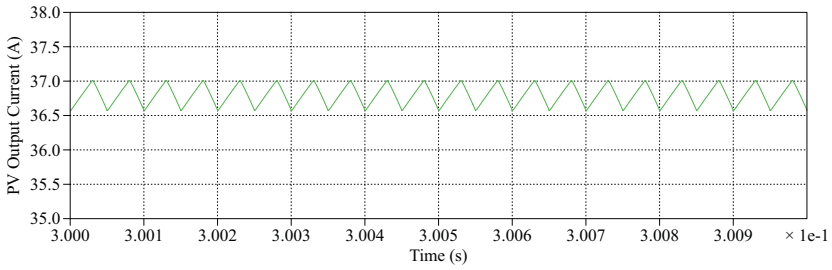

(a)

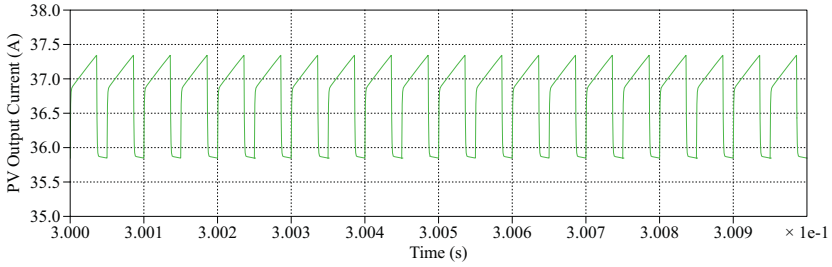

(b)

Figure 4.8. Steady-state PV current: (a) BHB, (b) flyback

current. Given that the converter input current equals to the PV output current and the mean PV output currents are nearly the same in both topologies, the inductor current of the flyback is thus shifted up to a higher range than that of the BHB.

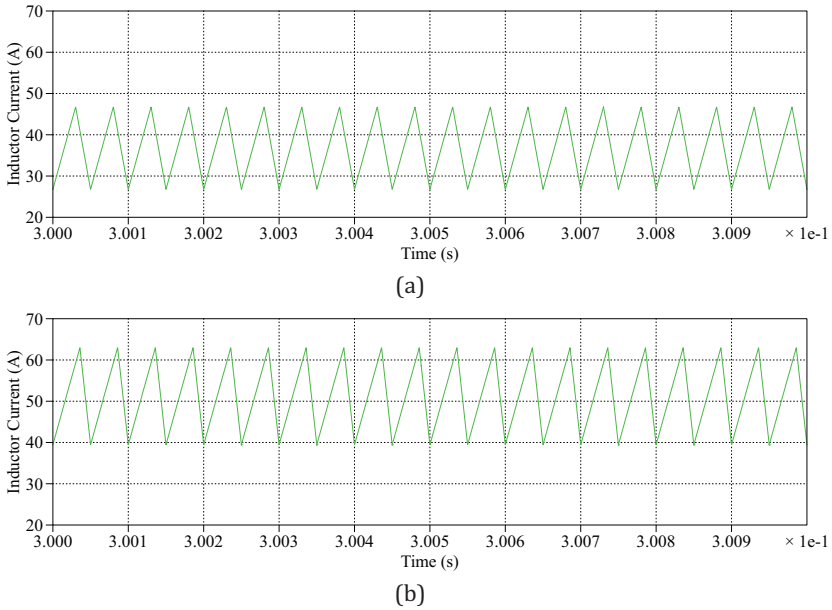

Figure 4.9. Steady-state inductor current: (a) BHB, (b) flyback

Meanwhile, the duty ratio of the flyback is also in a higher range than that of the BHB, as shown in Fig. 4.10. The reason can be seen from (4.1) and eq. (4.2) which represent the converter gain of both converters respectively. Given that the converter input voltage is the PV output voltage and the converter output voltage is the DC-link voltage, and both voltages are regulated to be the same for both converters, the voltage gain of both converters should be nearly the same. According to the calculation of (4.1)and (4.2), the duty ratio of the flyback is theoretically larger than that of the BHB, given the same voltage gain of both converters, and the waveforms of Fig. 4.10 proved this point.

The DC-link voltage and current waveforms are shown in Fig. 4.11 and Fig. 4.12 respectively. The DC voltages remain nearly constant and roughly the same for both of the converters. The DC current of the BHB is slightly lower than that of the flyback. The extracted PV power and converter output power of both converters are shown in Fig. 4.13 and Fig. 4.14, respectively. It can be seen that the BHB extracted slightly higher PV power than the flyback, which endures higher fluctuation during the process. However, the converted DC power of the BHB is not as much as that of the flyback. The power loss in the BHB topology is mainly resulted from the leakage inductance. This inductance is for energy storage in the circuit in order to achieve zero voltage switching of the main switches but clearly it comes with a crucial impact on the converter efficiency.

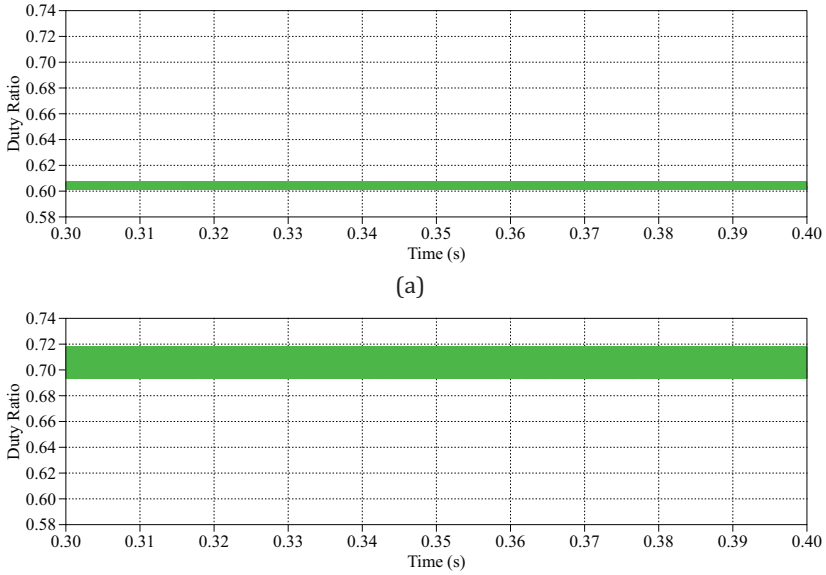

(a)

(b)

Figure 4.10. Steady-state DC/DC duty ratio: (a) BHB, (b) flyback

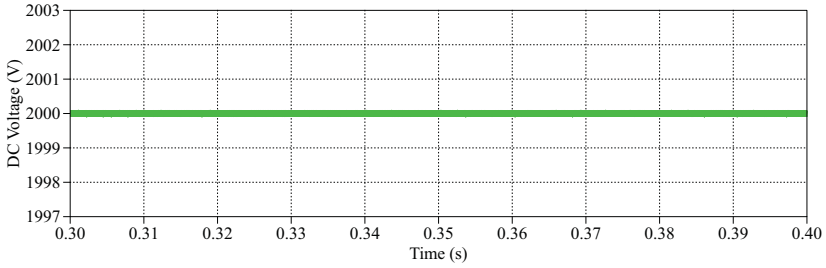

(a)

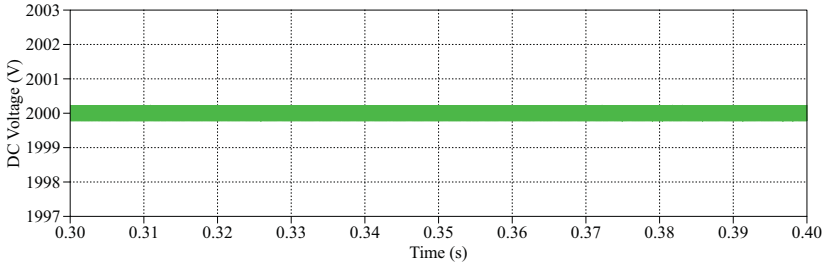

(b)

Figure 4.11. Steady-state DC-link voltage: (a) BHB, (b) flyback

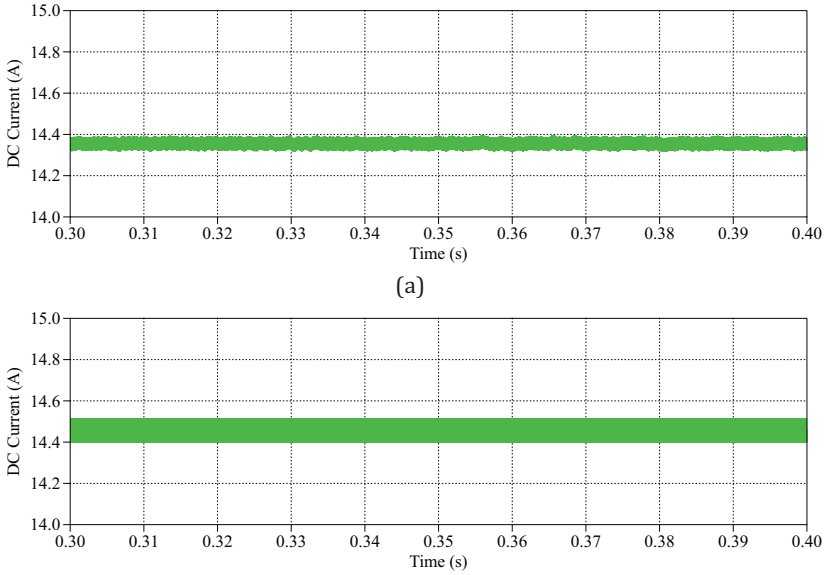

(a)

(b)

Figure 4.12. Steady-state DC-link current: (a) BHB, (b) flyback

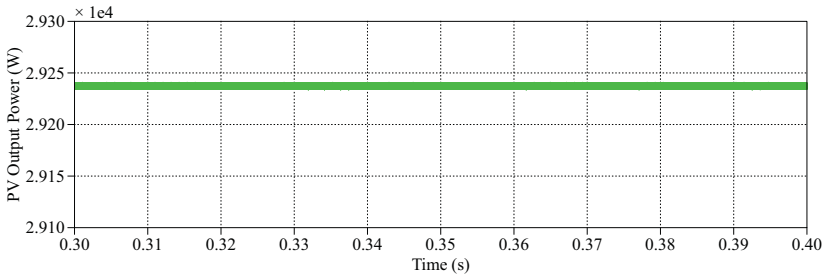

(a)

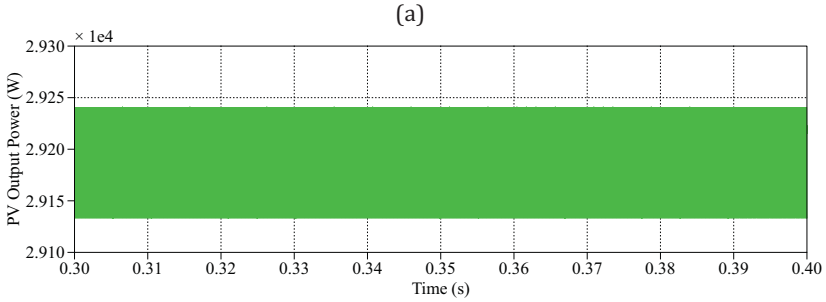

(b)

Figure 4.13. Steady-state PV output power: (a) BHB, (b) flyback

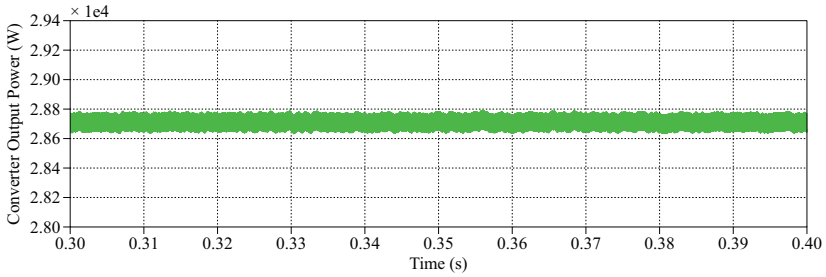

(a)

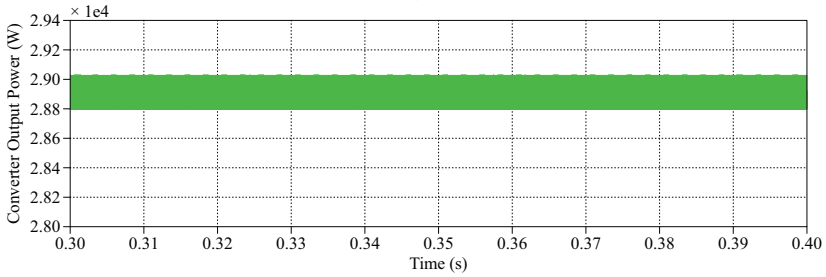

(b)

Figure 4.14. Steady-state converter output power: (a) BHB, (b) flyback

4.3.2 Operation with a Wide Input Voltage Range

Considering that the MPP of the PV modules changes significantly under varying atmospheric conditions and partial shading, the DC/DC converters should be able to track a wide range of MPPs. This means a wide range of PV operating voltages should be located precisely and as fast as possible under varying conditions. Therefore, a study on tracking varying input voltages across a wide range is conducted in this section.

In this case study, the PV array starts operation from open-circuit and follows a ramp reference voltage signal to reach the MPP at 1kW/m^2, 25°C. Then assuming that the ambient conditions changed and the new MPP voltage is to be located at 450 V. The PV array will follow another ramp reference voltage signal to reach the new operating point. By changing the converter voltage gain, the MPP voltages can be tracked during this procedure. The DC/DC converters should be able to follow the voltage reference signal during the whole process by adjusting the duty ratio fast and precisely.

The PV output voltage and current waveforms of both converters are shown in Fig. 4.15 and Fig. 4.16 respectively. Both converters are able to follow the reference fast and accurately. As shown in Fig. 4.17, the duty ratio of both converters is well controlled to adjust to the new working points. The inductor currents remain continuous, as shown in Fig. 4.18, and the DC-link voltage is maintained constant during the process as shown in Fig. 4.19. This is important for the DC/DC converters to track different input voltages through duty cycle adjustment. The extracted PV power is closely related to the PV output voltage and the profile is shown in Fig. 4.20. The variation of the DC current and the DC power can be observed from Fig. 4.21 and Fig. 4.22 respectively. Both converters are able to absorb most of the PV power and inject the DC power to the load. Some jumps can be observed on the DC current and power waveformes during transients, because the PI controllers used in the system are

not able to eliminate the error when following a fast changing ramp reference signal. Nevertheless, the system is stable during transients and behaves well without steady-state error.

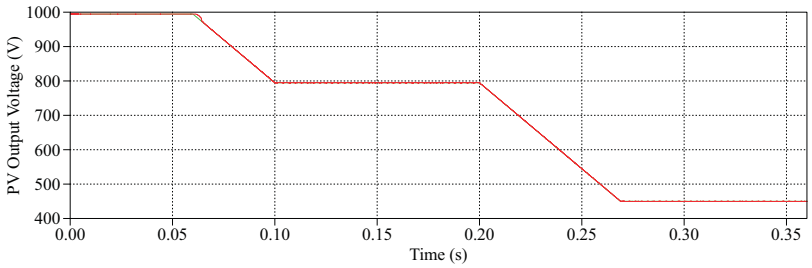

(a)

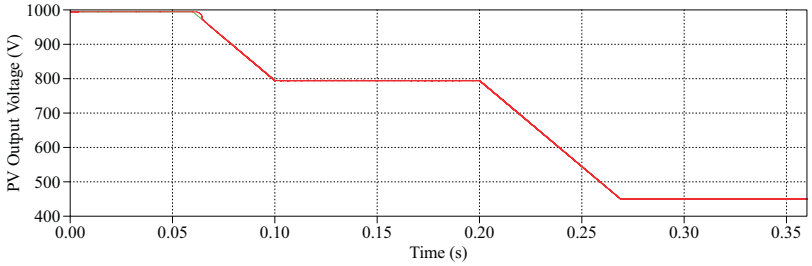

(b)

Figure 4.15. PV voltage: (a) BHB, (b) flyback

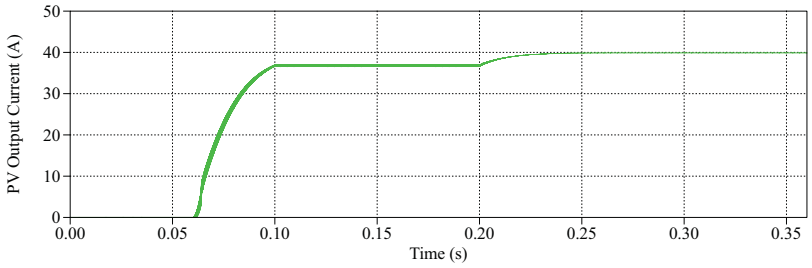

(a)

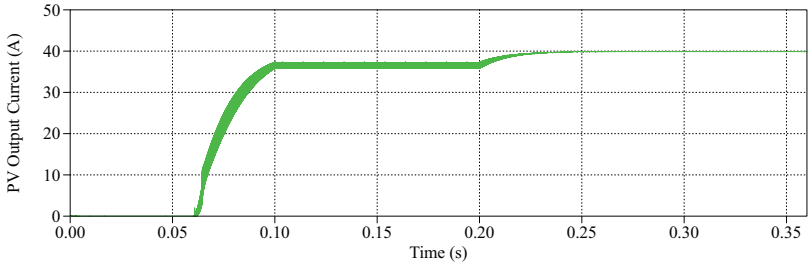

(b)

Figure 4.16. PV current: (a) BHB, (b) flyback

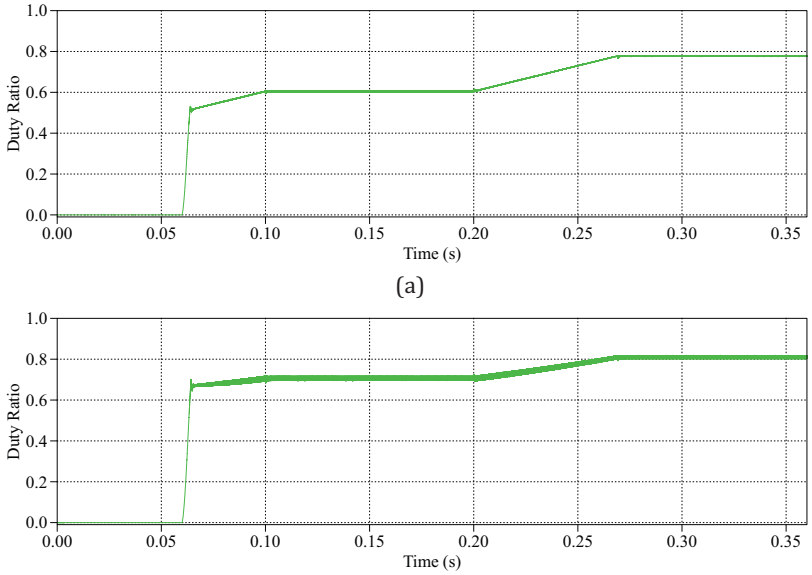

(a)

(b)

Figure 4.17. Duty ratio: (a) BHB, (b) flyback

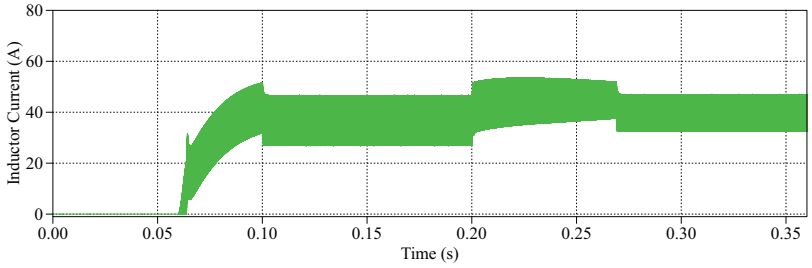

(a)

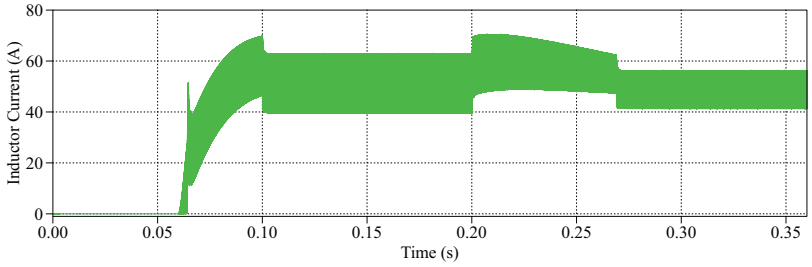

(b)

Figure 4.18. Inductor current: (a) BHB, (b) flyback

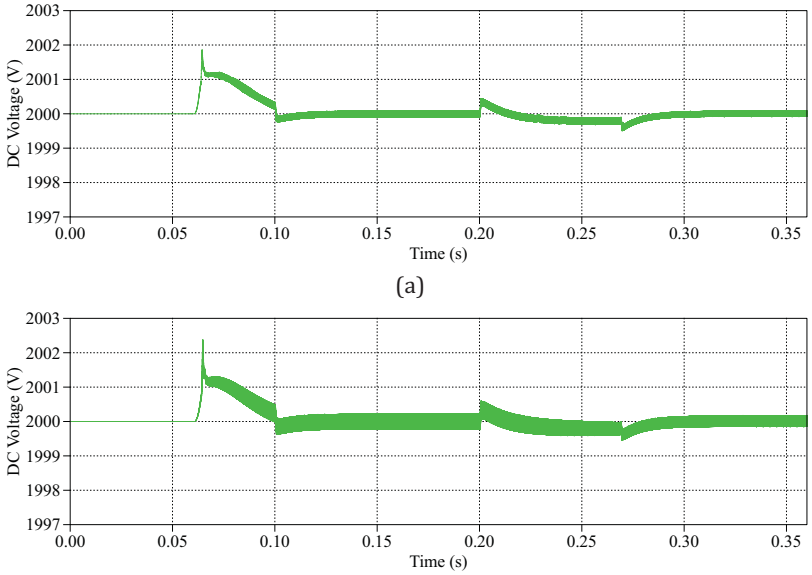

(a)

(b)

Figure 4.19. DC-link voltage: (a) BHB, (b) flyback

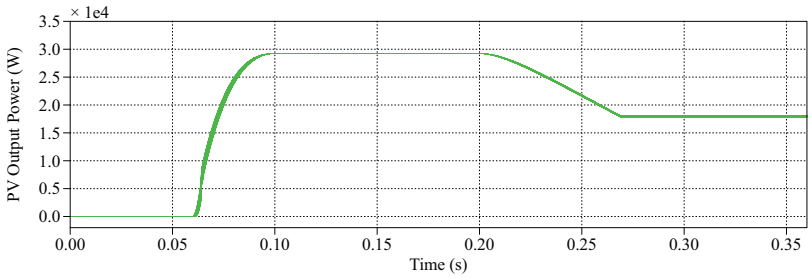

(a)

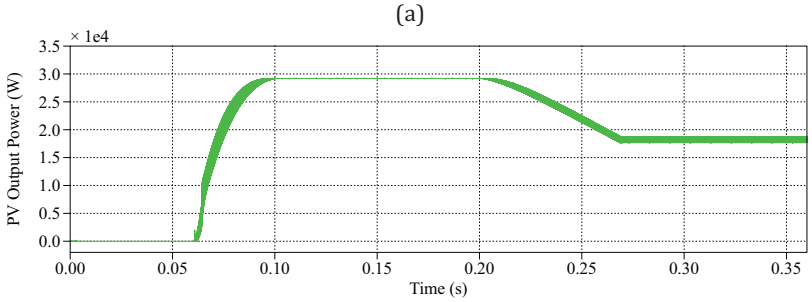

(b)

Figure 4.20. PV output power: (a) BHB, (b) flyback

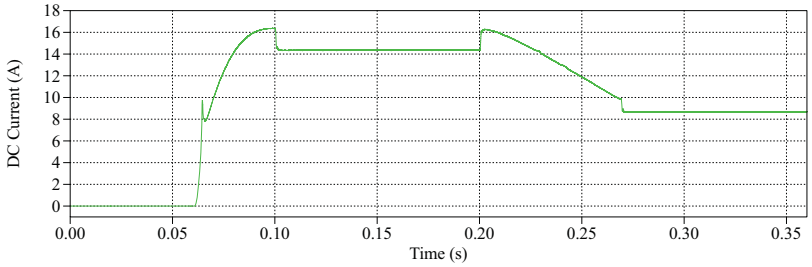

(a)

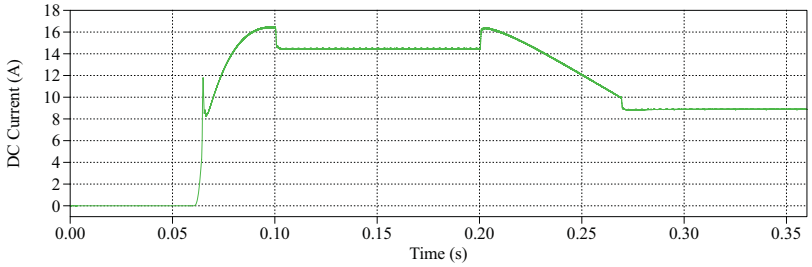

(b)

Figure 4.21. DC-link current: (a) BHB, (b) flyback

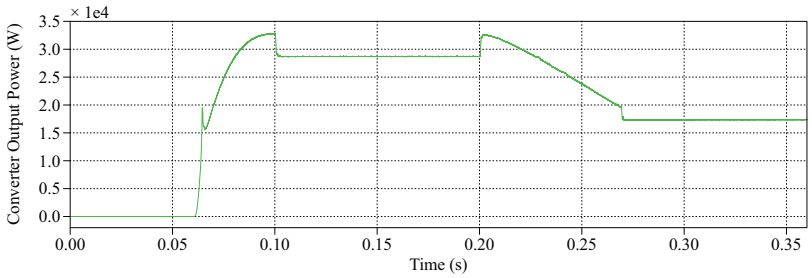

(a)

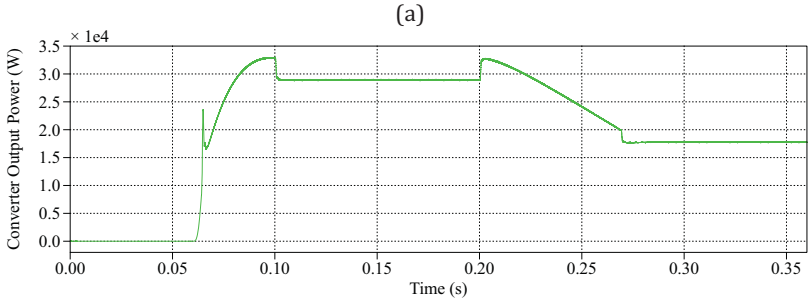

(b)

Figure 4.22. Converter output power: (a) BHB, (b) flyback

4.3.3 MPPT Operation

In this section, both DC/DC converters are simulated on performing MPPT using the incremental conductance (INC) algorithm. The MPPT operating frequency is 100 Hz (sampling period 0.01 s) and the incremental step is 0.1 V. The solar irradiation profile is shown in Fig. 4.23. The PV array outputs and the response of the DC/DC converters can be observed from the simulation results.

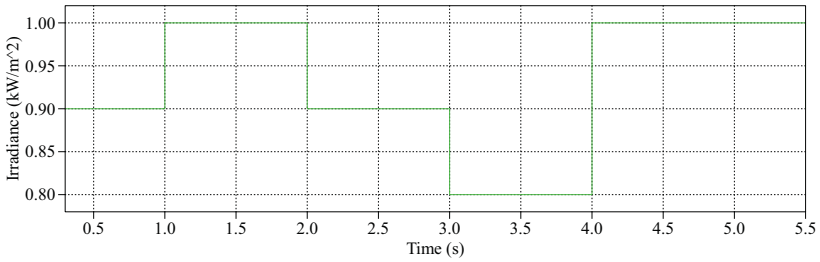

Figure 4.23. Solar irradiance profile

The PV output voltage reference signals for both converters calculated by the MPPT algorithm are shown in Fig. 4.24. It takes 0.1 s for the MPPT algorithm to track 1 V of change in the PV voltage and the accuracy of the algorithm depends on the incremental step size. The PV output voltage and current waveforms are shown in Fig. 4.25 and Fig. 4.26 respectively. The PV voltages of both converters are capable of following their references given by the individual MPPT. The flyback has lower average calculated MPP voltages and larger fluctuation around each working point compared with the BHB. It can be seen from Fig. 4.26 and Fig. 4.27, that the PV output current and power yield both drop immediately following each irradiation change, and slowly climb up while the PV voltage moves in the direction towards the MPP. The inductor current and duty ratio of the converters vary accordingly as shown in Fig. 4.28 and Fig. 4.29 respectively. The values of the flyback are in a higher range than those of the BHB, as determined by their circuit structure and working principles. The DC-link voltage remains relatively constant for both converters during the process as shown in Fig. 4.30. The output DC current and power of both converters are shown in Fig. 4.31 and Fig. 4.32 respectively. The BHB achieves lower yield compared with the flyback because of the loss induced by the leakage inductance in the circuit.

It is also worth noticing that the calculated PV MPP voltage reference values from the MPPT algorithm are slightly different for the two converters. The MPPT algorithm for the flyback ended up with values slightly deviated from the theoretical value. It seems that through the adjustment of duty ratio, the two converters find each of their own working point to accommodate the input from the PV to the load. The flyback managed to adjust the PV voltage lower but gives higher load current than the BHB; while the BHB adjust the PV voltage higher, which is closer to the theoretical MPP voltage, but gives lower load current due to the effect of the leakage inductance. Since the non-ideal characteristics of the devices is not considered in this study, the switching losses and conduction losses are not present. In this case, it is uncertain if the overall energy conversion efficiency of the BHB is lower than that of the

flyback, because the BHB also offers ZVS and ZCS features which can significantly reduce the switching losses associated with the devices.

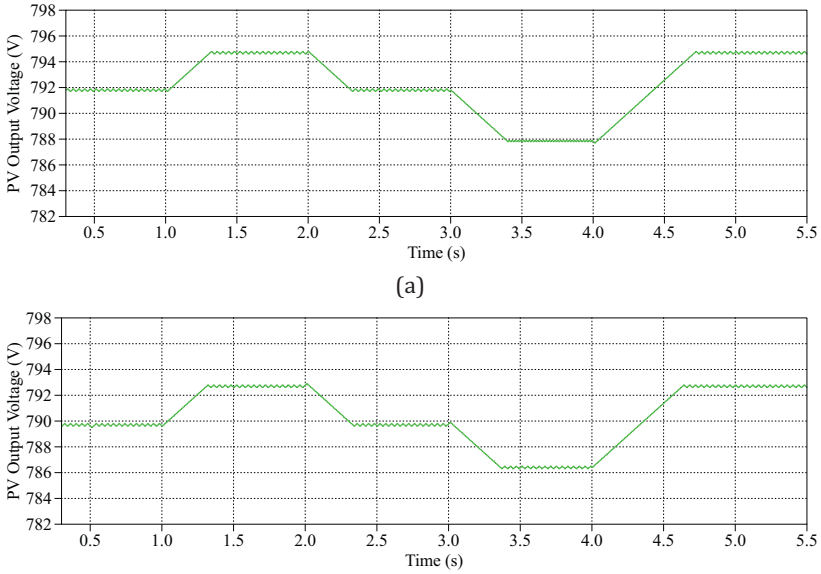

(a)

(b)

Figure 4.24. PV voltage reference signal calculated by the MPPT algorithm: (a) BHB, (b) flyback

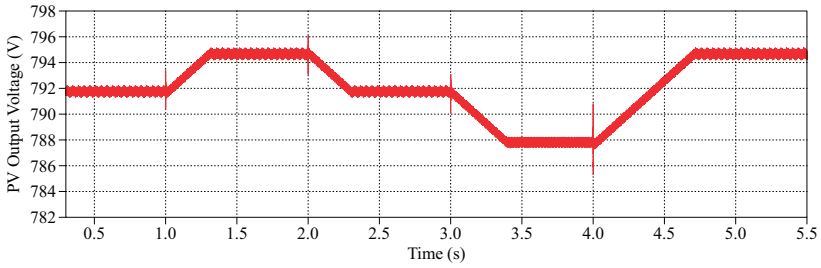

(a)

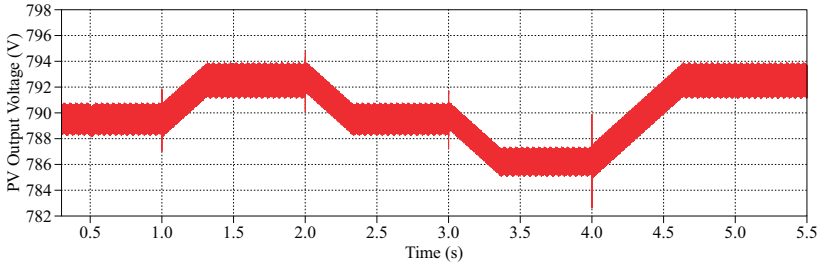

(b)

Figure 4.25. PV voltage: (a) BHB, (b) flyback

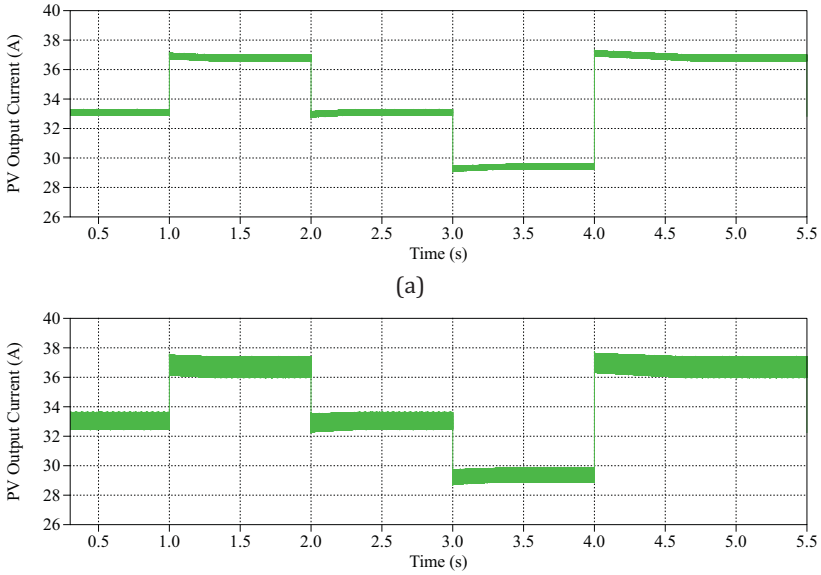

Figure 4.26. PV current: (a) BHB, (b) flyback

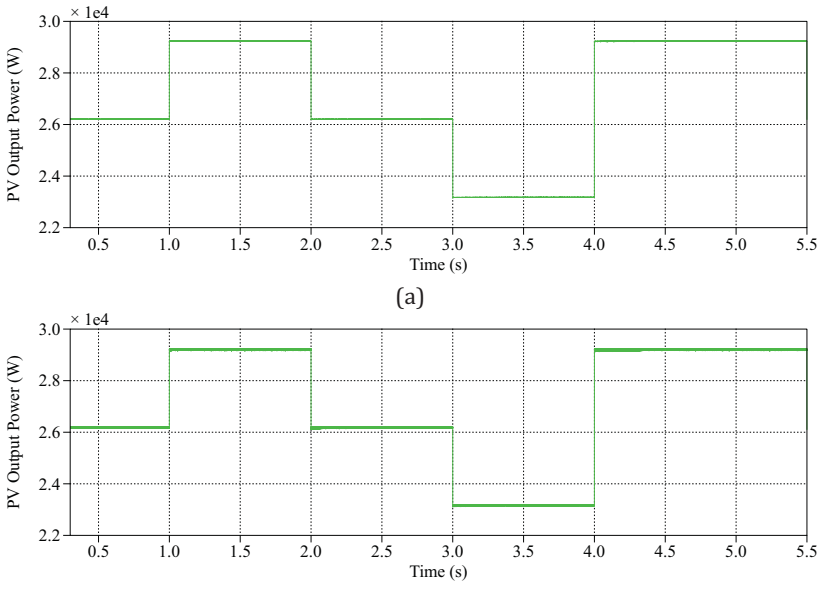

Figure 4.27. PV power: (a) BHB, (b) flyback

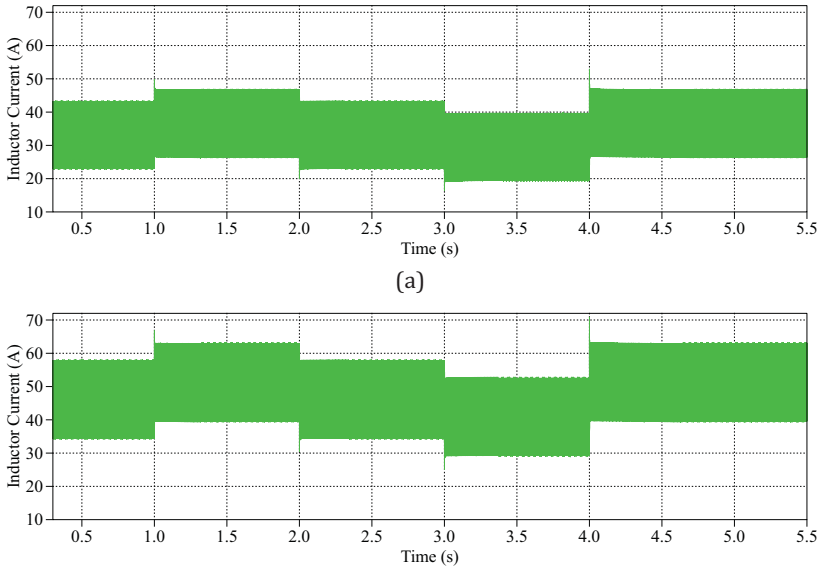

Figure 4.28. Inductor current: (a) BHB, (b) flyback

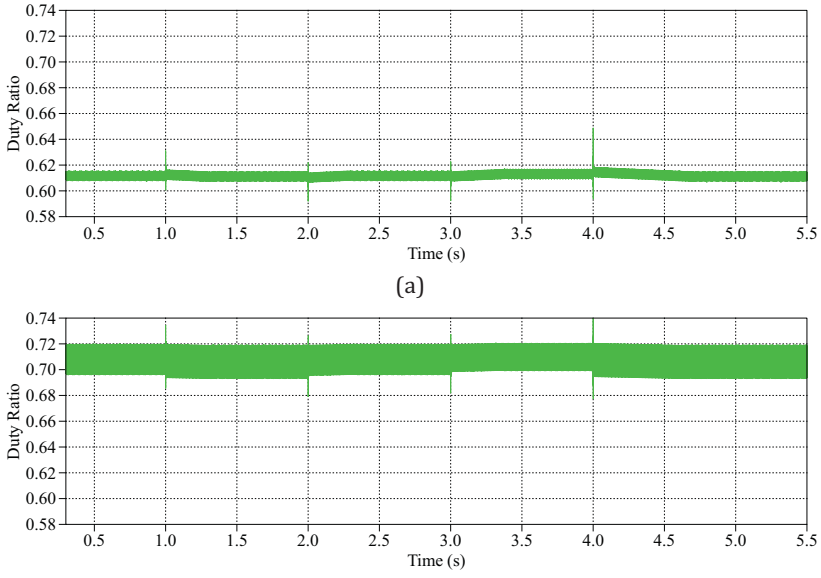

Figure 4.29. Duty ratio: (a) BHB, (b) flyback

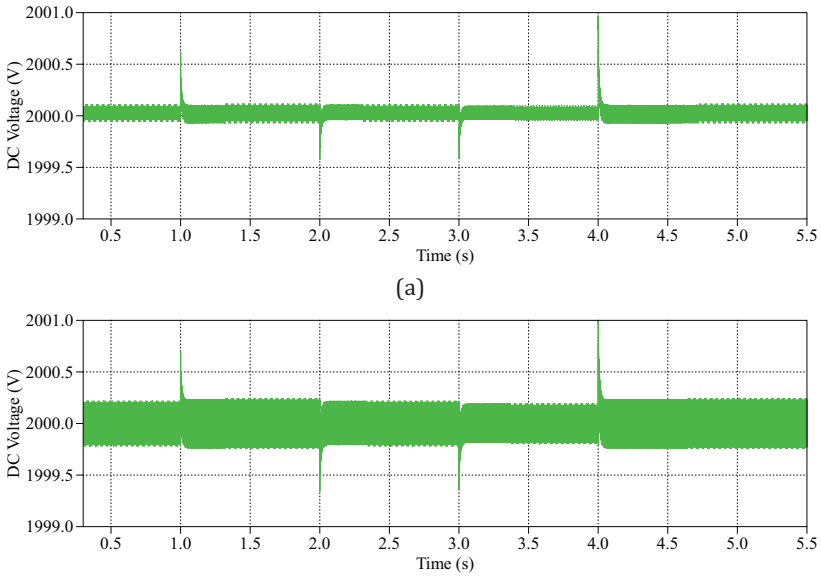

(a)

(b)

Figure 4.30. DC-link voltage: (a) BHB, (b) flyback

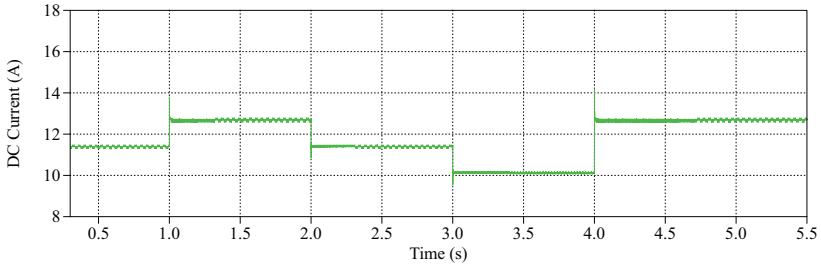

(a)

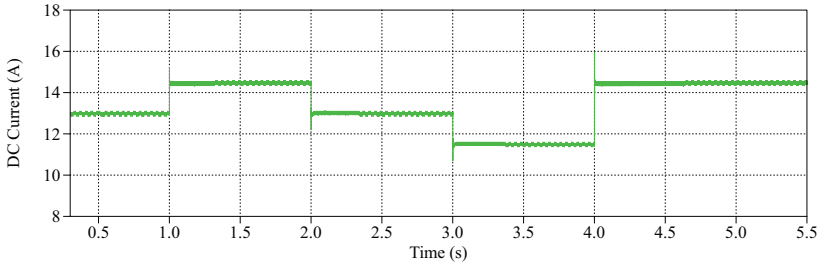

(b)

Figure 4.31. DC-link current: (a) BHB, (b) flyback

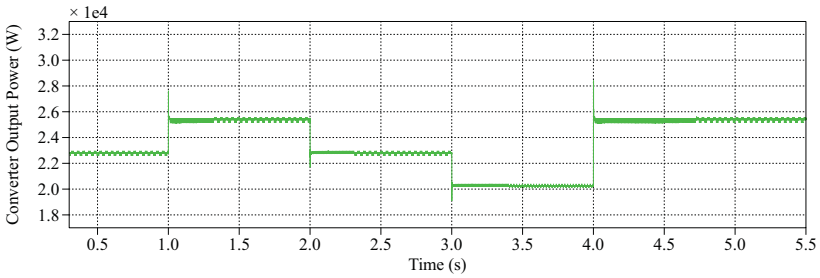

(a)

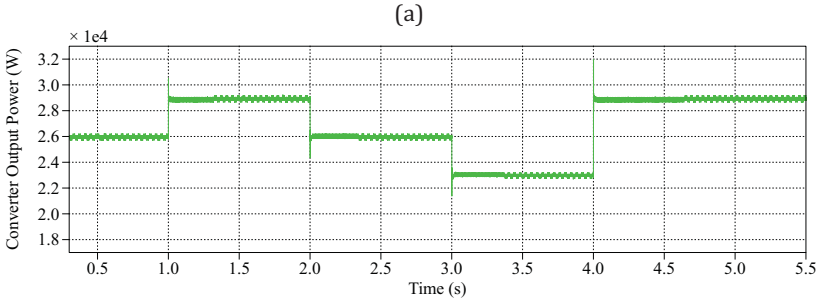

(b)

Figure 4.32. Converter output power: (a) BHB, (b) flyback

Chapter 5

CHB Multilevel converter with isolated DC/DC converters for grid connection of large scale PV generation

5.1 Introduction

The CHB converter offers a modular solution for the large-scale PV system integration to medium-voltage grids. A large number of PV modules are divided into arrays and equipped with isolated DC/DC converters which perform MPPT to obtain the optimal energy yield. The DC/DC converters work as separate DC sources for the CHB converter and isolate the PV modules from the grid, in order to prevent the PV panel-to-ground leakage currents from flowing through. The CHB central inverter collects the PV power from the DC-links and converts the DC power to grid-compatible AC power. The PV power from the converter system is injected to the grid through filters. The overall system topology is shown in Fig. 5.1. It features high voltage and power capability and good power quality.

The topologies and operating principles of the CHB converter and the isolated DC/DC converters have been described in the previous chapters, where the performance of the converters was also fully investigated through simulation studies. In this chapter, simulations are conducted in MATLAB/Simulink and PLECS Blockset [82], in order to verify the presented system topology as a whole. Several case studies are carried out to validate the system topology from different aspects, featuring the evaluation of the DC-side isolation, the MPPT operation under varying solar irradiance, the overall system performance comparison between the utilization of two isolated DC/DC converter topologies, namely the flyback and the BHB converter [76], and finally the high power capability achieved by means of expanding the CHB converter voltage level, featuring different control approaches, specifically, with PI controllers applied in the dq frame and PR controllers applied in the $\alpha\beta$ frame [115].

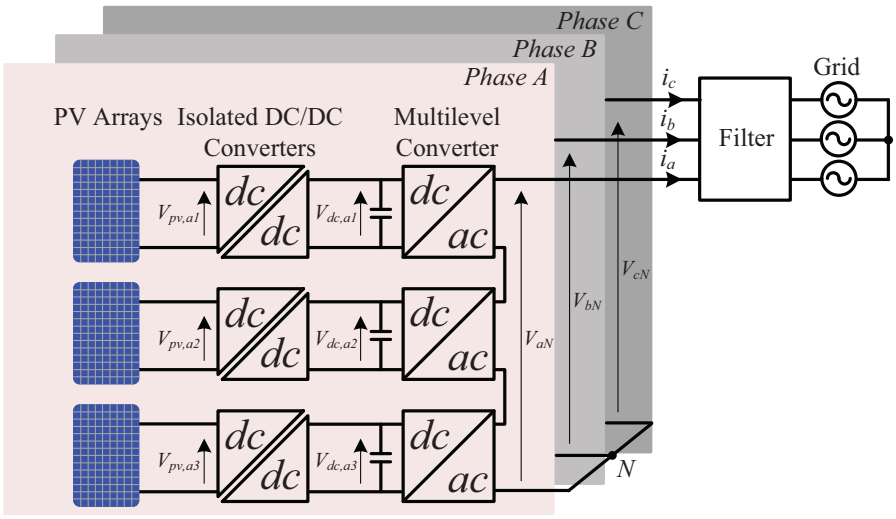

Figure 5.1. Topology of the grid-connected PV system featuring the CHB converter with isolated DC/DC converters

5.2 Case study 1: DC-side isolation

5.2.1 Case study description

Considering the parasitic capacitance and leakage current effect of the PV panels as well as the requirements from grid standards that the PV system must be grounded, galvanic isolation is applied in this system [26]. Compared with line-frequency transformers, high-frequency transformers are lighter in weight and smaller in size. Advanced power electronics technologies are adopted to achieve better performance and higher efficiency. Therefore, DC-side isolation is applied by means of high-frequency transformers integrated in the isolated DC/DC converters.

The PV modules are divided into nine PV arrays, each feeding an isolated DC/DC converter. These DC/DC converters are connected to the common CHB converter through nine different DC-links, serving as the nine isolated DC sources for the CHB converter. Each PV array is composed of 10 parallel connected PV strings, while each string is comprised of 45 series connected PV modules. The PV module used for the simulation is based on the characteristics of the BP 365 module [81]. This configuration constitutes a 263 kW_P PV power plant. Detailed system configuration is shown in Fig. 5.2.

The simulation is under standard test conditions (STC). The solar radiation level and ambient temperature considered in the simulations remain constant at 1 kW/m^2 and 25°C. All components in the system are ideal and no power imbalance between the H-bridges or phases of the CHB converter is considered.

A 7-level, three-phase CHB converter is applied in the simulation. Each phase of the converter consists of three series connected H-bridges (k=3), synthesizing a 7-level output phase voltage waveform (n=2k+1). Based on the commonly used PS-PWM, three carriers phase-shifted between one another by 60° ($= 180°/k$) are applied to each H-bridge in the three

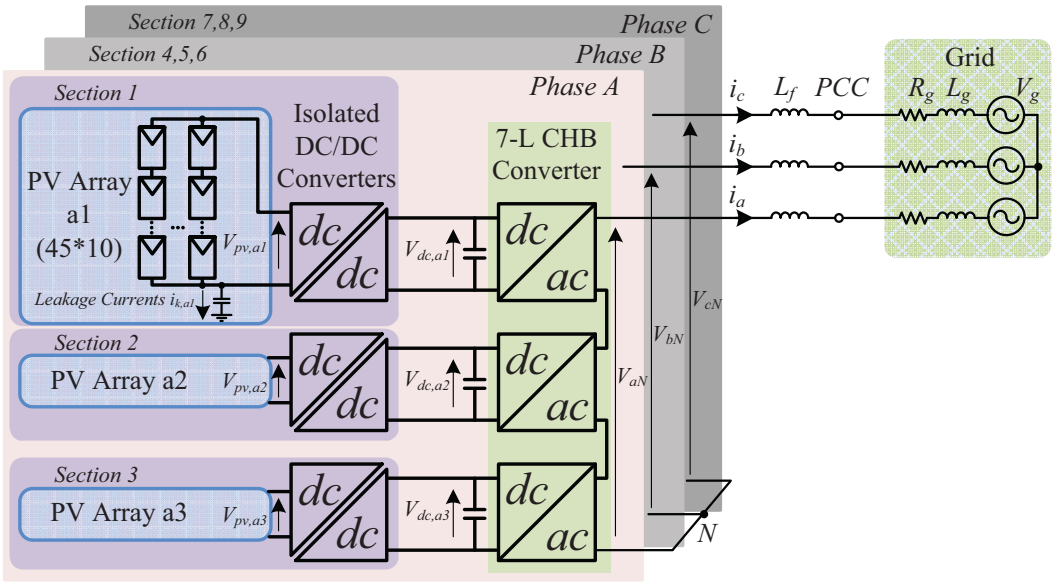

Figure 5.2. Configuration of the grid-connected PV system featuring the 7-L CHB converter with isolated DC/DC converters

phases. The unipolar switching pattern gives each H-bridge an equivalent output frequency twice the actual device switching frequency, and the multiplicative effect achieved by the phase-shifted carriers contributes to a triple equivalent frequency at each phase output of the converter. Thus the PS-PWM scheme gives an equivalent converter output frequency six times the power semiconductor actual switching frequency, and the sideband harmonics are moved to higher frequency range and are easier to filter out.

The control structure of the system is depicted in Fig. 5.3. It mainly involves two parts. One is the control of the DC/DC converters in order to perform MPPT; the other is the control of the CHB converter which involves grid synchronization, DC voltage regulation and grid current control. The MPPT algorithm used in this work is the well-known incremental conductance (INC) method, which was introduced in Chapter 4. The duty ratio of the DC/DC converter is adjusted by a PI controller in order to reach the PV voltage reference value calculated by the MPPT algorithm. The synchronization of the converter system to the grid is provided by a three-phase PLL and the connection to the grid is through an inductor (0.05 p.u.). The VOC control method is implemented in the CHB converter. In this work, the VOC is performed in the synchronous rotating reference frame, including two control loops. The inner loop regulates the grid currents by PI controllers through $dq \rightarrow abc$ transformation, with decoupling between I_d and I_q control. The generated control signals V_d^* and V_q^* are then transformed from the dq frame back to the abc frame as the three phase voltage reference signals v_a^*, v_b^*, and v_c^*. The outer loop is used to maintain the average of the nine DC-link voltages. The deviation of the average DC-link voltage from the reference value is reflected in the inner current loop, to adjust the control signals V_d^* and V_q^*. The resulting three phase voltage reference signals v_a^*, v_b^* and v_c^* are used to generate the modulation indices which go through the modulator to generate the switching signals for the H-bridges. As the CHB converter involves a number of isolated DC sources, DC-link voltage balancing is an important consideration in the control design. In this work, a feed-forward compensation algorithm

is applied. The nine DC-link voltages first go through a Proportional (P) controller, the output of which reflects each deviation of the corresponding DC-link voltage from the reference average value. The three phase voltage reference signals v_a^*, v_b^* and v_c^* are divided by the adjusted DC-link voltages from the P controller, generating individual modulation index for each H-bridge. The changes to individual modulation indices affect the current that the converter draws from the corresponding DC-link capacitors and thus alter the DC-link voltages. In this way the DC-link voltages are regulated accordingly and maintained at a constant average value.

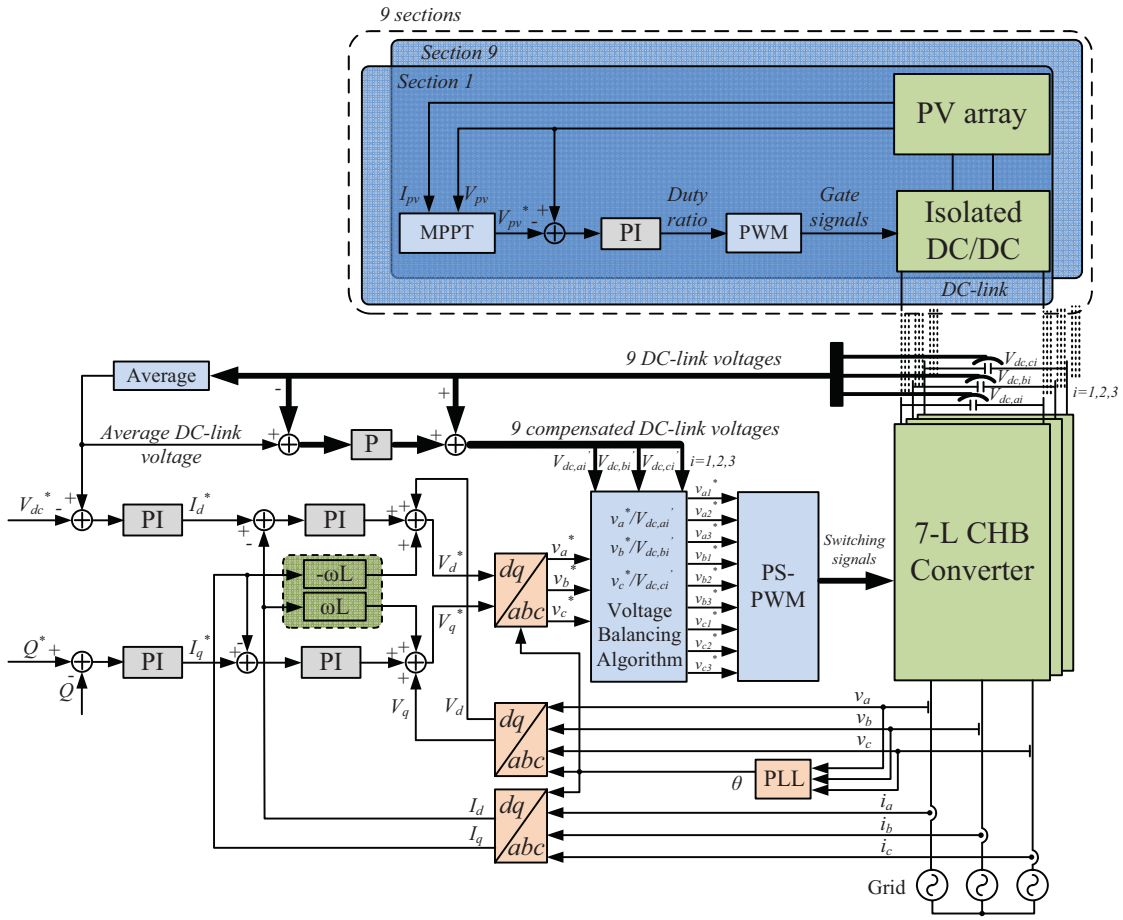

Figure 5.3. Control structure of the 7-L CHB grid-connected PV system

In order to verify the importance of the DC-side isolation, a comparison is made between the utilization of the non-isolated boost converter and the isolated flyback converter. The topologies of the two DC/DC converters are shown in Fig. 5.4. The converter voltage gain is given by (5.1) and (5.2) for the boost and the flyback respectively.

$$\frac{V_{out}}{V_{in}} = \frac{1}{1-D} \tag{5.1}$$

$$\frac{V_{out}}{V_{in}} = \frac{D}{1-D}\frac{N_S}{N_P} \tag{5.2}$$

The parameters used for the simulation and the system specifications are listed in Table

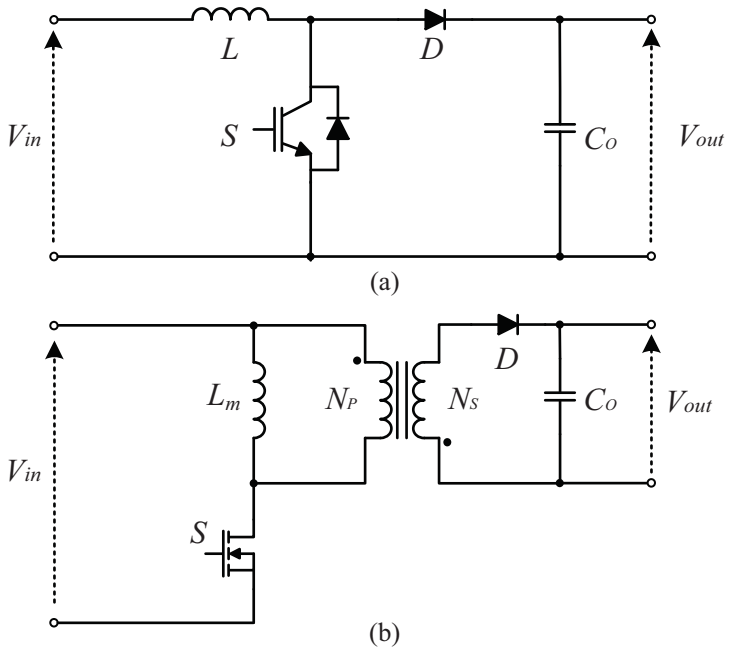

Figure 5.4. DC/DC topologies: (a) non-isolated boost converter, (b) isolated flyback converter

5.1. Note that there is a PV panel-to-ground resistance considered in the simulations which is set very differently for the two types of DC/DC converters. The value for the non-isolated converter is significantly higher than that for the isolated converter, in order to provide physical insulation to withstand the high voltage induced on the DC side and limit the leakage currents within 30 mA as required by the German standard VDE-0126-1-1 [29]. The resistance value for the flyback converter is very low and can be ignored. It is simply set as a series resistance of the PV parasitic capacitor, to help the PLECS solver to solve the system functions.

5.2.2 Simulation results

The simulations results of the system are shown in the below sections, which are divided into the results from the PV generators, from the DC/DC converters, and from the CHB converter and the grid interconnection.

A. The PV Generators

As previously discussed, the PV arrays in the non-isolated system prove to withstand the high voltages induced on the DC side by the PWM of the CHB converter. The profile of the PWM induced potential at each input of the three series connected H-bridges of the CHB converter phase A is shown in Fig. 5.5, which is also the voltage across the corresponding PV array and its parasitic capacitor plus the insulation resistor. The three waveforms in Fig. 5.5 are in sequence of the top H-bridge cell (HB 1), the middle cell (HB 2) and the bottom cell (HB 3). The PV panel-to-ground voltage and leakage current for both topologies (top H-bridge power cell in phase A as an example) are shown in Fig. 5.6. The panel-to-ground voltage steps between -6 kV and 4 kV and the leakage current of the PV panel fluctuates between -20

Table 5.1. Simulation parameters - Case study 1

PV module (BP 365)		**CHB converter**	
Maximum Power P_{MPP}	65 W	Number of series-connected H-bridges per phase (k)	3
MPP Voltage V_{MPP}	17.67 V	Levels of the converter ($n = 2k + 1$)	7
MPP Current I_{MPP}	3.68 A	Switching frequency f_s	1 kHz
Open circuit voltage V_{OC}	22.04 V	DC-link voltage V_{dc}	2 kV
PV array		Rated Power	300 kW
Array configuration (Series $\times$ Parallel)	45$\times$10	Grid-side filter L_f	20 mH
Maximum Power P_{MPP}	29.25 kW	**Grid**	
MPP Voltage V_{MPP}	794.6 V	Grid voltage (line-line RMS)	6 kV
MPP Current I_{MPP}	36.8 A	Fundamental frequency	50 Hz
Open circuit voltage V_{OC}	994.5 V	Grid impedance	R_g =5.4 mΩ, L_g =172 μH

DC/DC converter		
Converter topology	Boost (non-isolated)	Flyback (isolated)
Switching frequency	20 kHz	20 kHz
Input inductor	1.22 mH	1.22 mH (L_m)
Output capacitor	1.25 mF	1.25 mF
High-frequency transformer turns ratio ($N_S : N_P$)	1:1	1:1
PV panel parasitic capacitance	100 pF	100 pF
PV panel-to-ground resistance	$10^5\Omega$	$10^{-6}\Omega$

mA and 20 mA in the non-isolated system. This panel-to-ground stepped voltage is the result of the modulation of the CHB converter that introduces the high voltages to the DC side. As the potential at the DC-side of every H-bridge varies during the modulation process and is added upon the PV panel together with its parasitic capacitor, the leakage current finds its path through the parasitic capacitor and flows to the ground. However, this is not the case when the flyback converters are used. The high-frequency transformer integrated in the flyback converter isolates the DC-side from the AC-side. There is no path for the leakage current to flow through the grid converter and ground. Therefore no leakage current occurs while the PV panels are grounded, and no PWM induced potential is added upon the PV panels.

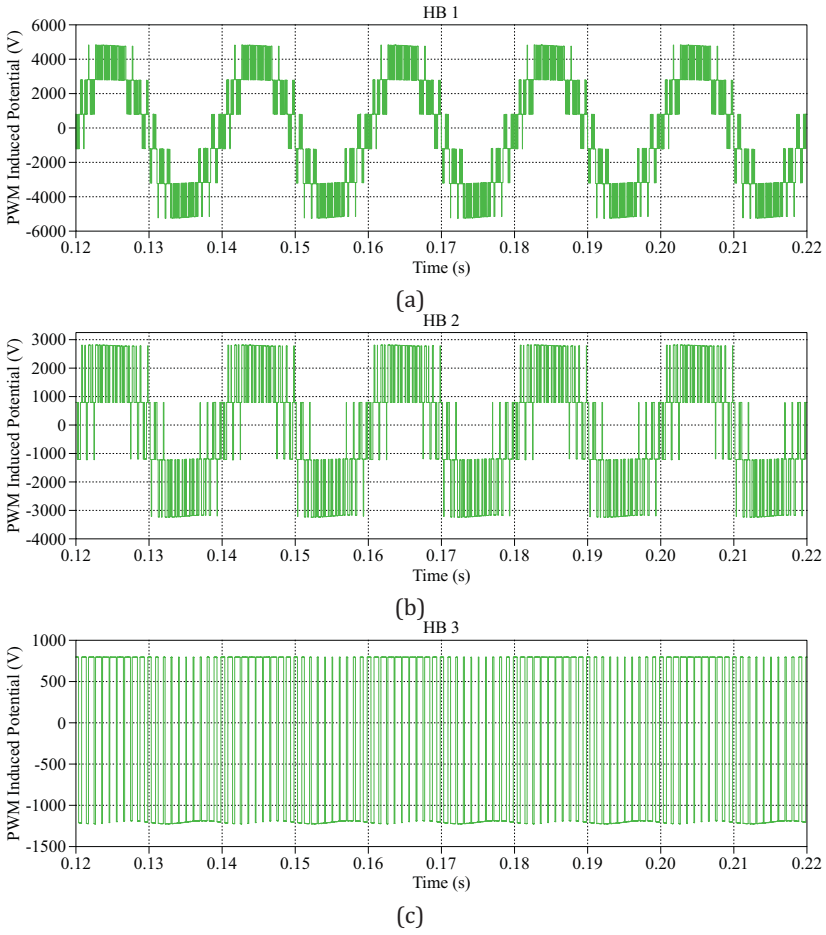

Figure 5.5. PWM induced potential at the DC-side of the CHB converter in the non-isolated topology

The PV output voltage and current for both topologies are shown in Fig. 5.7 and Fig. 5.8, respectively. The ripples on the voltage and the specific shapes of the current are subject to the circuit topology. The flyback topology is derived from the buck-boost converter, which is the non-isolated counterpart. The characteristics of the flyback converter in terms of voltage and current profiles are mostly the same with buck-boost converter. The comparison now would be between the characteristic of the buck-boost converter and the boost converter. Compared to boost converter, buck-boost has higher ripple on the input voltage, which in this case is the PV voltage, because the voltage gain of the converter is more sensitive to the variation of the duty ratio (see equations (5.1) and (5.2)); and higher ripple on the input

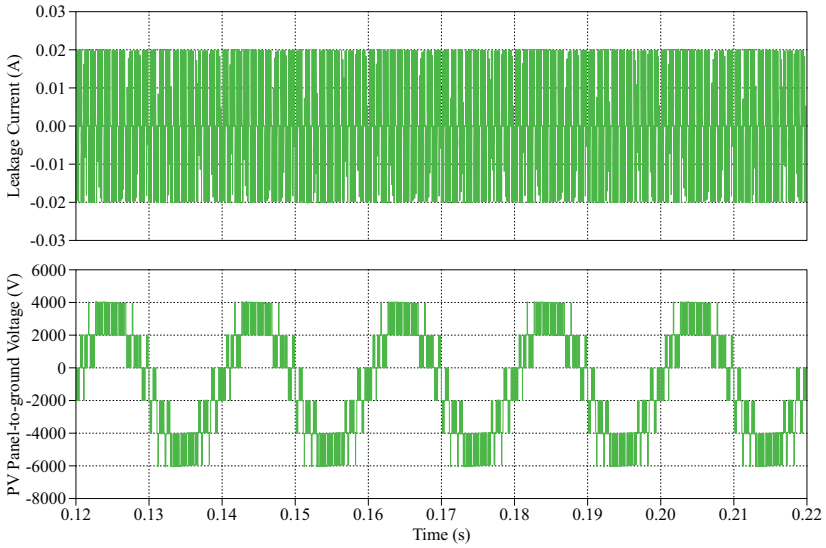

(a)

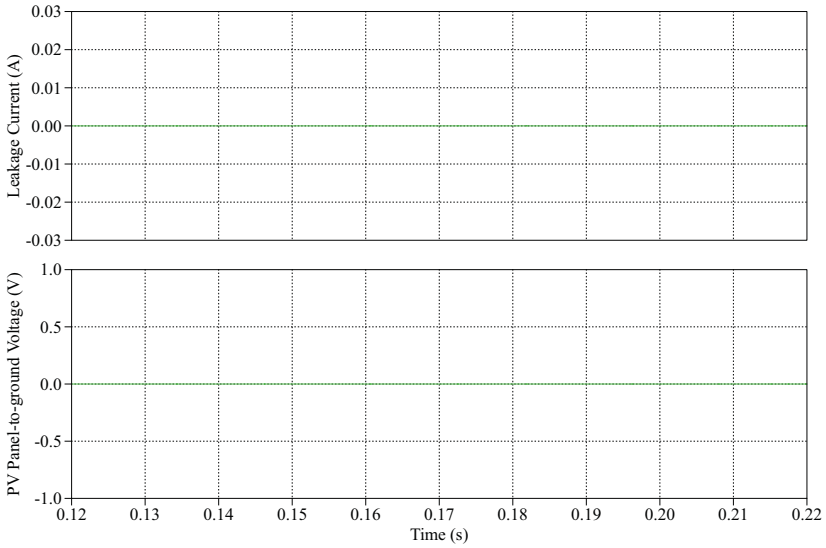

(b)

Figure 5.6. The panel-to-ground voltage and leakage current of the PV array at an H-bridge power cell: (a) boost, (b) flyback

current, which in this case is the PV current, due to the location of the input inductor in the converter (see Fig. 5.4).

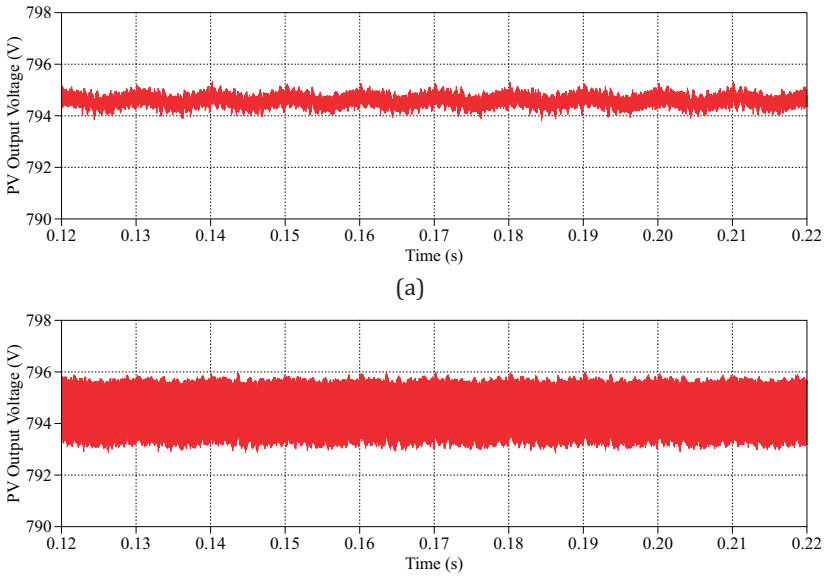

(a)

(b)

Figure 5.7. PV voltage: (a) boost, (b) flyback

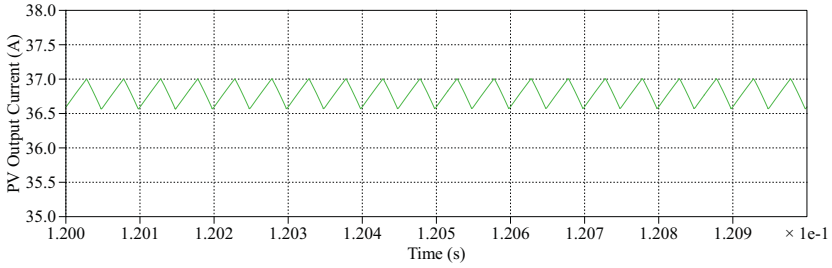

(a)

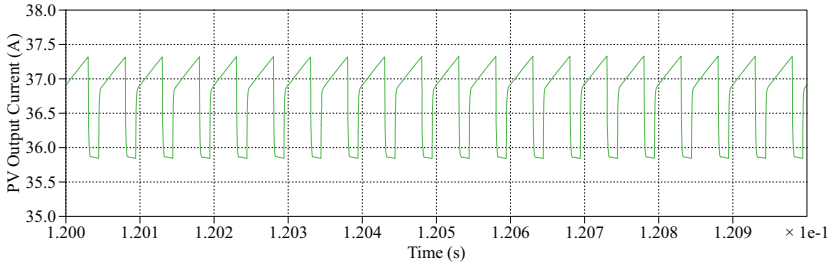

(b)

Figure 5.8. PV current: (a) boost, (b) flyback

B. The DC/DC Converters

The inductor current and the duty ratio of both DC/DC converters are shown in Fig. 5.9 and Fig. 5.10, respectively. As previously discussed, the comparison comes to the characteristics of the boost converter and the buck-boost type converter. As shown in Fig. 5.9 and Fig. 5.10, the inductor current and the duty ratio of the flyback converter are higher than those of the boost converter. This is because the inductor current equals to the input current plus the output diode current in the flyback (when the turns ratio of the transformer is 1:1), while the inductor current equals to the input current in the boost. Meanwhile the converter gain of each converters is calculated from (5.1) and (5.2) respectively for the boost and the flyback converter. Since the PV current and DC-link current are the same for both DC/DC converters, the inductor current is bigger in the flyback; and since the PV voltage and the DC-link voltage are the same for both converters, the duty ratio is bigger in the flyback as well.

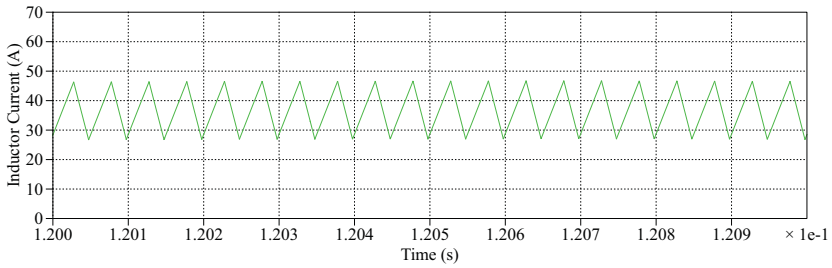

(a)

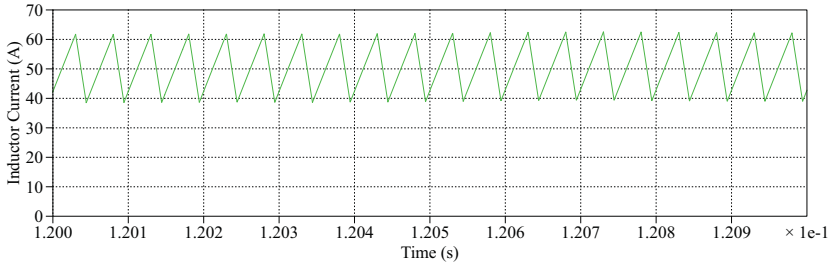

(b)

Figure 5.9. DC/DC converter inductor current: (a) boost, (b) flyback

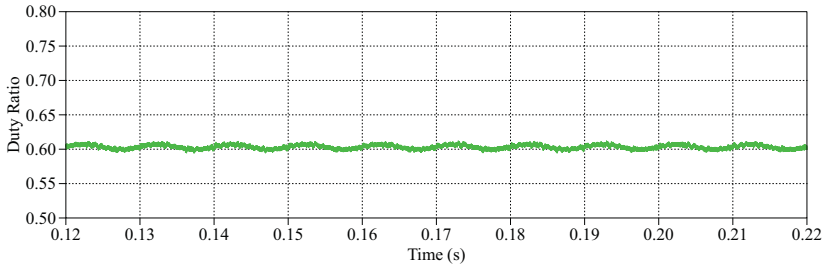

(a)

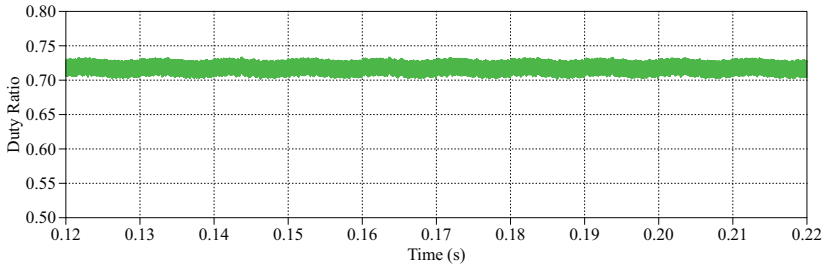

(b)

Figure 5.10. DC/DC duty ratio: (a) boost, (b) flyback

C. The CHB Converter and the Grid

The nine DC-link voltages, the CHB output phase voltage and the grid currents are shown in Fig. 5.11, Fig. 5.12 and Fig. 5.13, respectively. The CHB converter can fulfill its task of maintaining the DC-link voltage at 2 kV and well balanced, giving the 7-level stepped output voltages, and regulating the three-phase grid currents in good quality.

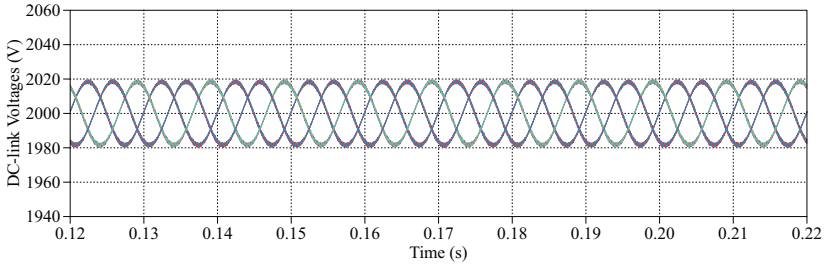

(a)

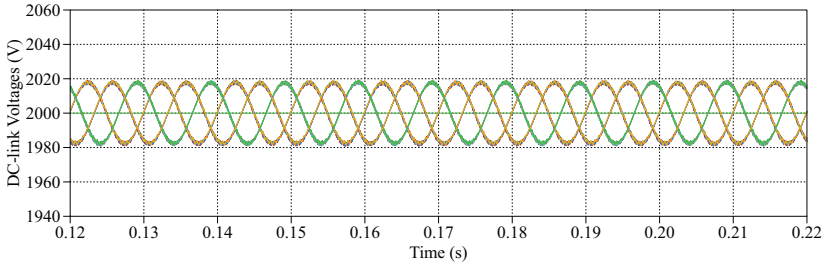

(b)

Figure 5.11. Nine DC-link voltages: (a) boost, (b) flyback

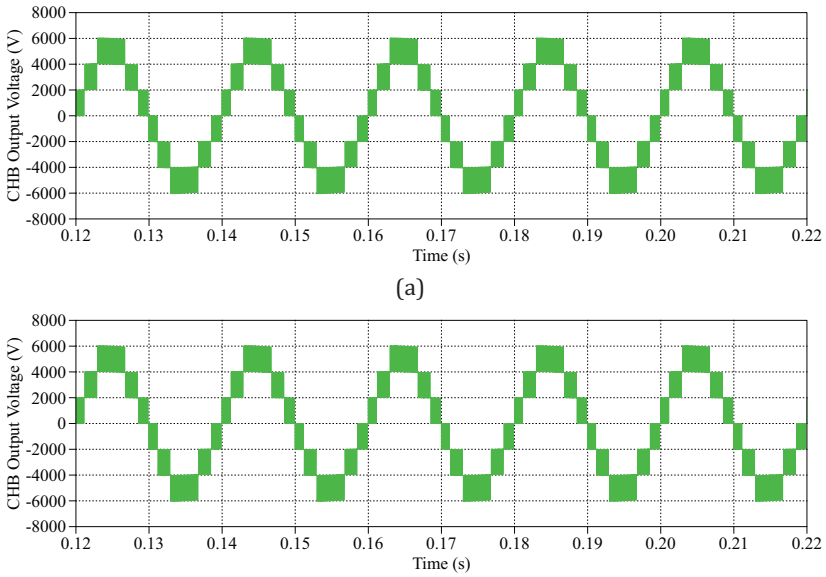

(a)

(b)

Figure 5.12. CHB output phase voltage: (a) boost, (b) flyback

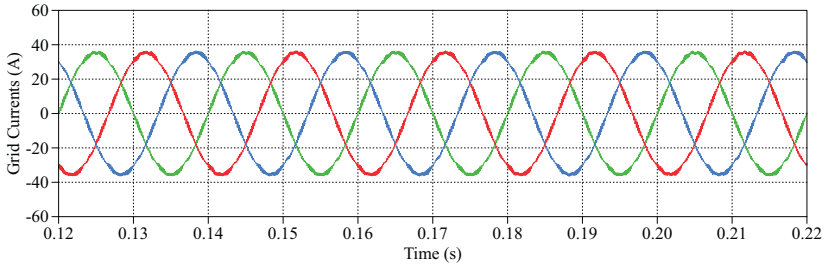

(a)

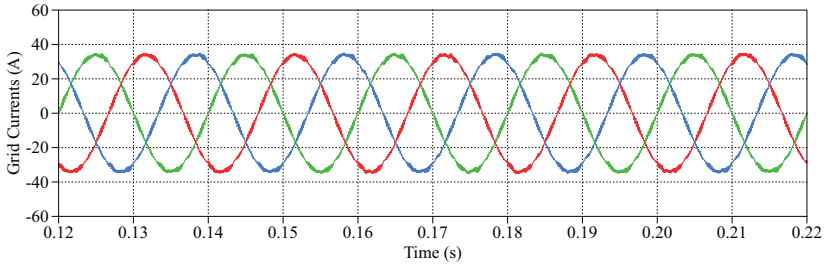

(b)

Figure 5.13. Three-phase grid currents: (a) boost, (b) flyback

5.3 Case study 2: MPPT operation under varying solar irradiance

5.3.1 Case study description

In Chapter 4 the MPPT operation of DC/DC converters has been investigated. In the previous section, non-isolated and isolated DC/DC converters have been investigated on their applications in the grid-connected CHB converter system. In this section, the MPPT operation of isolated DC/DC converters which integrate the PV sources into the 7-level CHB grid-connected converter system is investigated. The BHB converter is implemented in this study and the circuit topology is shown in Fig 5.14. The voltage gain of the converter is given by (5.3).

$$\frac{V_{out}}{V_{in}} = \frac{1}{1-D}\frac{N_S}{N_P} \tag{5.3}$$

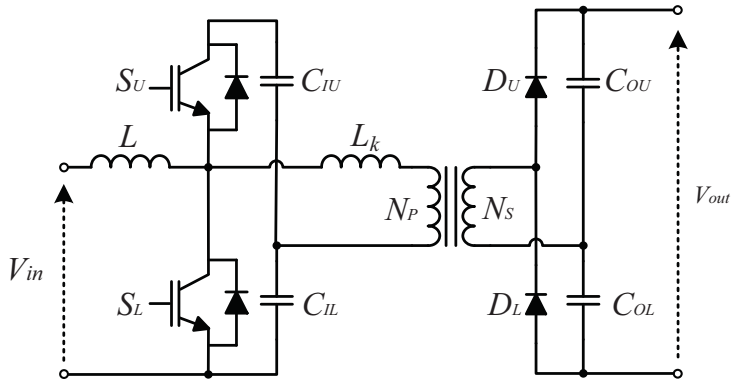

Figure 5.14. Isolated DC/DC topology: boost-half-bridge (BHB) converter

The system configuration and the control structure are as shown in Fig. 5.2 and Fig. 5.3 in the previous section, respectively. The system specifications are listed in Table 5.2.

Table 5.2. Simulation parameters - Case study 2

PV module (BP 365)		**CHB converter**	
Maximum Power P_{MPP}	65 W	Switching frequency f_s	1 kHz
MPP Voltage V_{MPP}	17.67 V	DC-link Voltage V_{dc}	2 kV
MPP Current I_{MPP}	3.68 A	Rated Power	300 kW
Open circuit voltage V_{OC}	22.04 V	Grid-side Filter L_f	20 mH
PV array		**Grid**	
Array configuration (Series $\times$ Parallel)	45$\times$10	Grid voltage (line-line RMS)	6 kV
Maximum Power P_{MPP}	29.25 kW	Fundamental frequency	50 Hz
MPP Voltage V_{MPP}	794.6 V	Grid impedance	R_g =5.4 mΩ, L_g =172 μH
MPP Current I_{MPP}	36.8 A	**DC/DC converter**	
Open circuit voltage V_{OC}	994.5 V	Converter topology	BHB
MPPT		Switching frequency	20 kHz
MPPT Algorithm	Incremental Conductance (INC)	Input inductor	1.2 mH (L) + 0.02 mH (leakage inductance L_k)
Sampling period	0.01 s	DC-link capacitance	5 mF
Incremental step	0.15 V	High-frequency transformer turns ratio ($N_S : N_P$)	1:1

5.3.2 Simulation results

The solar irradiance profile is shown in Fig. 5.15. It starts from 1 kW/m^2 and changes to 0.95 kW/m^2 at t =0.3 s. The calculated MPP voltage from the MPPT algorithm is shown in Fig. 5.16. It can be seen that the accuracy of the MPPT algorithm is determined by the incremental step. The smaller the incremental step, the more accurate the algorithm but the longer it takes to track down the MPP under varying solar irradiance. The MPPT of this system is able to locate the MPP under constant solar irradiance and track the new MPP after the irradiance changes. The PV output voltage and current of the PV array in one H-bridge power cell are shown in Fig. 5.17 and Fig. 5.18, respectively. The PV output voltage is able to follow the reference given by the MPPT algorithm and changes from 794.6 V to 793.3 V. The PV output current drops to 34.9 A immediately when the irradiance decreases and gradually rises up by 0.1 A as the PV output

voltage is adjusted towards the new MPP. The extracted PV power is shown in Fig. 5.19. It reduces immediately when the irradiance drops and is increased slightly as the new MPP is reached. The duty ratio of the DC/DC converter for the corresponding PV array is shown in Fig. 5.20. The change in the waveform is very subtle as the converter operating point does not need major changes. The DC-link current of the corresponding H-bridge power cell is shown in Fig. 5.21. It drops when less power is extracted as the irradiance reduces and is also increased when the new MPP is achieved under the reduced irradiance. The nine DC-link voltage waveforms of the CHB converter are shown in Fig. 5.22. They are well balanced and maintained at 2 kV with less than 1 p.u. fluctuation. The three-phase grid currents are shown in Fig. 5.23. They are regulated in good sinusoidal shape during the whole process. The THD of the grid currents slightly increases from 3.1% to 3.28% as the fundamental of the grid currents drops when the irradiance is reduced.

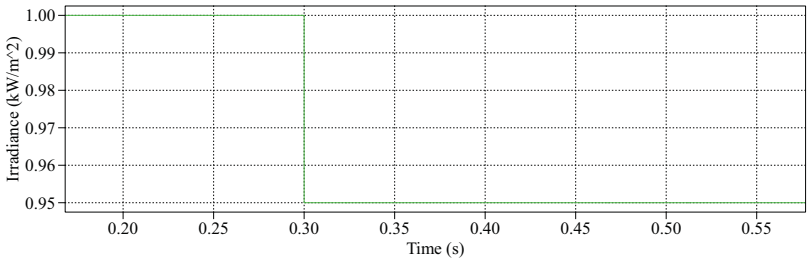

Figure 5.15. Solar irradiance profile

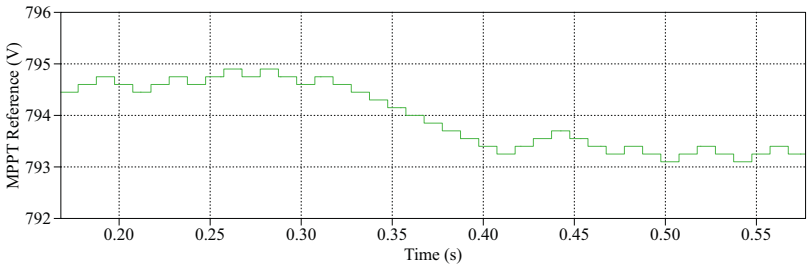

Figure 5.16. PV voltage reference calculated by the MPPT algorithm

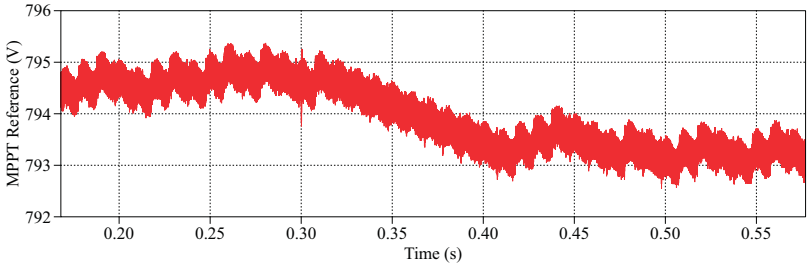

Figure 5.17. PV voltage

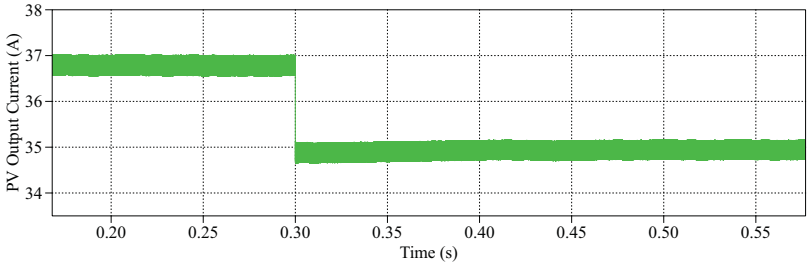

Figure 5.18. PV current

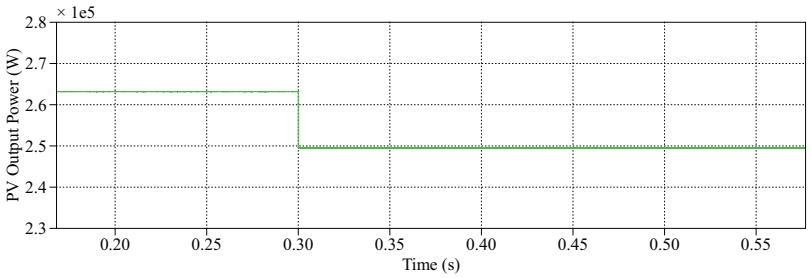

Figure 5.19. PV output power

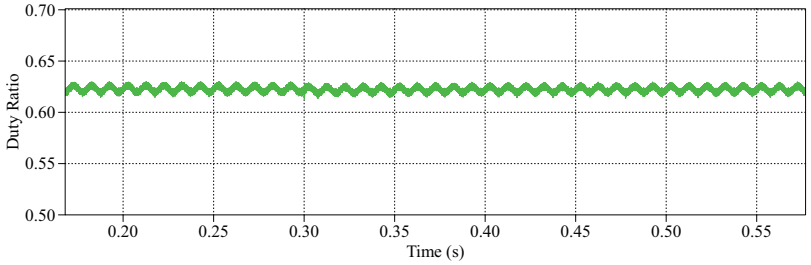

Figure 5.20. DC/DC duty ratio

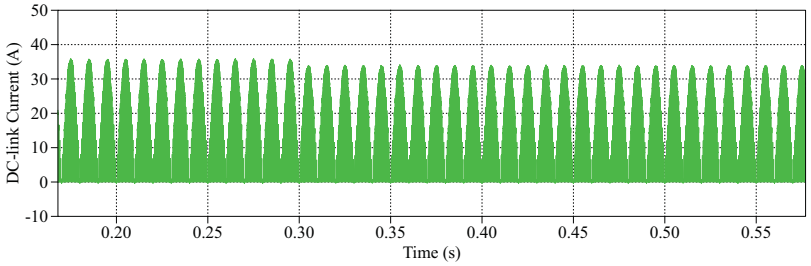

Figure 5.21. DC-link current

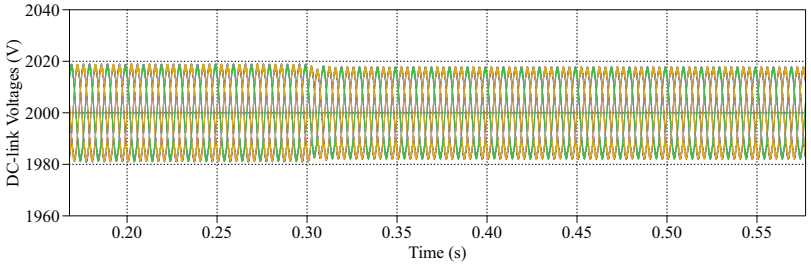

Figure 5.22. Nine DC-link voltages

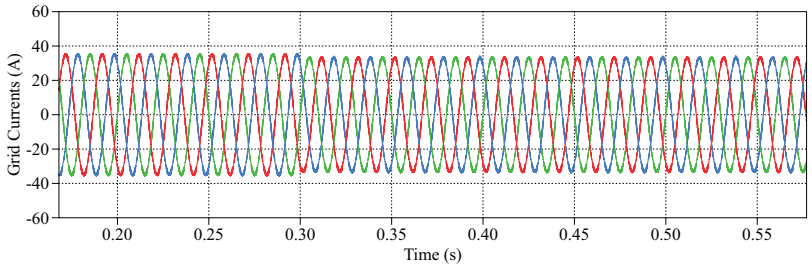

Figure 5.23. Three-phase grid currents

5.4 Case study 3: Comparison between two isolated topologies - the boost-half-bridge (BHB) and the flyback

5.4.1 Case study description

The characteristics of the BHB converter and the flyback converter are introduced in Chapter 4. Here simulation results will be provided to compare the performance of these two DC/DC topologies. The circuit topology of the flyback and the BHB are as shown in Fig. 5.4(b) and Fig. 5.14 respectively. The operation of both converters is investigated in two case studies. The first study is to check the capability of the DC/DC converters on achieving a certain operating point where the PV achieves its MPP, focusing on the steady-state performance of the converters under constant solar irradiation and temperature. The second study is to check the capability of the DC/DC converters on keeping track of the MPPs under varying environmental conditions or in case of partial shading, focusing on the dynamic response during changes of PV operating voltage. The two studies are approached by adding direct voltage referencing signals to the controller that regulates the duty ratio of the DC/DC converter. Through adjustment of the duty ratio, the PV array operating point changes accordingly. In the first case the PV output voltage value of the MPP at the solar irradiance of 1 kW/m^2 and the temperature of 25°C is directly applied as the PV voltage referencing signal. For the second case specifically, PV voltage reference varies in a range from 450 V to 800 V based on industry practice [83], so as to check if the DC/DC converter could follow the changes and regulate the PV output voltage as required fast and precisely.

The study in the case studies basically involve three operating points of the PV arrays, shown as point A, point B, and point C on the PV output characteristics curves in Fig. 5.24. Point A is the open-circuit condition, when the output voltage equals to the open-circuit voltage 994.5 V and the output current equals to 0, which gives zero output power. Point B is the PV array MPP under 1 kW/m^2 solar irradiance and 25°C temperature, where the PV output voltage equals to 794.6 V and the output current 36.8 A, giving the array maximum output power of 29.2 kW. Point C is chosen as the lower limit of PV operating voltage in the MPP range, considering the changes in the environmental condition and partial shading. The operating voltage of the PV array at point C equals to 450 V, giving a reduced output power of 17.9 kW with a slightly increased current of 39.9 A. The system specifications are listed in Ta-

ble 5.3. Additionally, in order to make a fair comparison between the two DC/DC topologies, all the parameters of the controllers for both DC/DC converters are the same.

Table 5.3. Simulation parameters - Case study 3

PV module (BP 365)		**CHB converter**	
Maximum Power P_{MPP}	65 W	Number of series-connected H-bridges per phase (k)	3
MPP Voltage V_{MPP}	17.67 V	Levels of the converter ($n = 2k + 1$)	7
MPP Current I_{MPP}	3.68 A	Switching frequency f_s	1 kHz
Open circuit voltage V_{OC}	22.04 V	DC-link voltage V_{dc}	2 kV
PV array		Rated Power	300 kW
Array configuration (Series $\times$ Parallel)	45$\times$10	Grid-side filter L_f	20 mH
Maximum Power P_{MPP}	29.25 kW	**Grid**	
MPP Voltage V_{MPP}	794.6 V	Grid voltage (line-line RMS)	6 kV
MPP Current I_{MPP}	36.8 A	Fundamental frequency	50 Hz
Open circuit voltage V_{OC}	994.5 V	Grid impedance	R_g =5.4 mΩ, L_g =172 μH

DC/DC converter		
Converter topology	BHB	Flyback
Switching frequency	20 kHz	20 kHz
Input voltage range	450 ~800 V	450 ~800 V
Input inductor	1.2 mH (L) + 0.02 mH (leakage inductance L_k)	L_m =1.22 mH
Input filter capacitor	C_I =1 mF, $C_{IU} = C_{IL}$ =50 μF	C_I =1 mF
Output capacitor	$C_{OU} = C_{OL}$ =2.5 mF	C_O =1.25 mF
High-frequency transformer turns ratio ($N_S : N_P$)	1:1	1:1

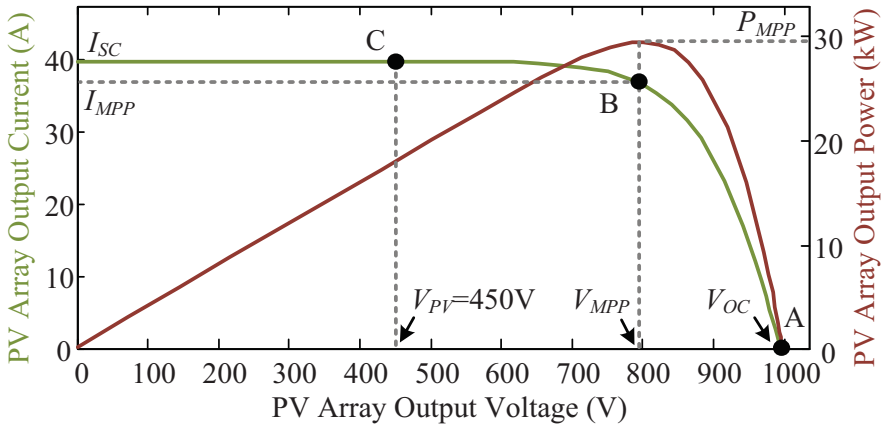

Figure 5.24. PV operating points on its output characteristic curve

5.4.2 Simulation results

5.4.2.1 MPP operation under constant atmospheric conditions

As shown in Fig. 5.25, the PV system starts from open-circuit, allowing 0.06 s of settling time for the PLL to achieve grid synchronization. The PV voltage follows a ramp reference which starts from the open-circuit voltage down towards the MPP voltage at the rate of 100 V per fundamental period (0.02 s) and then stays at the MPP voltage. The solar irradiation and the temperature remain constant during this process. Starting with the ramp reference is to avoid the initial overshoot in the grid currents as a result of the dynamics of the controllers. During this process, the PV array operating point should move from point A to B along the characteristic curve as shown in Fig. 5.24, and then continue working at point B. The DC/DC converters are responsible for the MPP tracking while the CHB converter keeps the DC-link voltages balanced at the desired level with minor fluctuation.

The steady-state results of both DC/DC converters are shown from Fig. 5.25 to Fig. 5.31. It can be seen that both converters can achieve the MPP operation under constant atmospheric conditions. The PV voltage and current waveforms at the MPP are shown in Fig. 5.25 and Fig. 5.26, respectively. The BHB achieves lower ripple in regulating the PV voltage and current than the flyback. The inductor current and duty ratio are shown in Fig. 5.27 and Fig. 5.28 respectively. Both converters work in the continuous conduction mode. The inductor current and the duty ratio are both at lower range with smaller ripple in the BHB than those in the flyback. This means that the BHB is more efficient on MPPT than the flyback due to smaller fluctuation of the PV operating points. The flyback, on the other hand, has a much smaller component count which is an advantage over the BHB. However, the ZVS feature of the BHB which gives less switching loss and the potential of building the multiphase DC/DC topology that is capable of high-voltage high-power operation make it a fairly competitive candidate. Additionally, the modular and flexible design of the multiphase DC/DC topologies is a plus in the PV power systems.

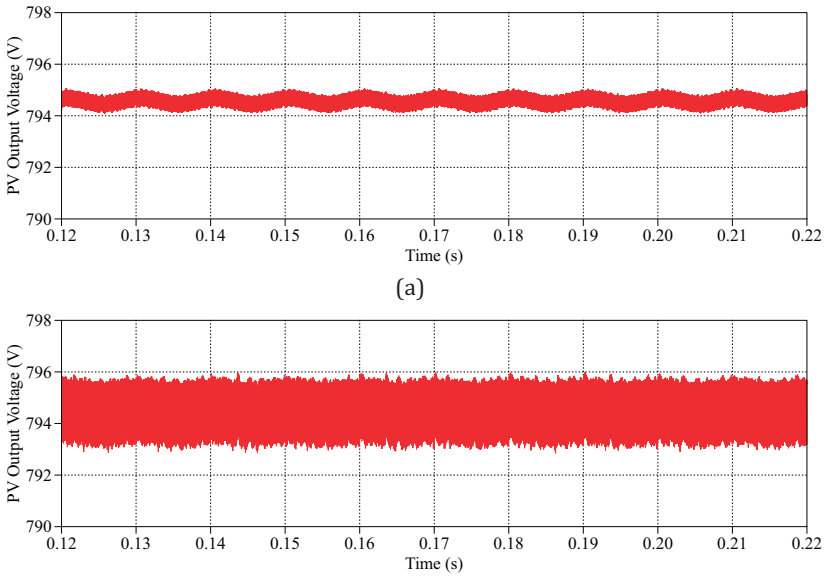

(a)

(b)

Figure 5.25. Steady-state PV voltage: (a) BHB, (b) flyback

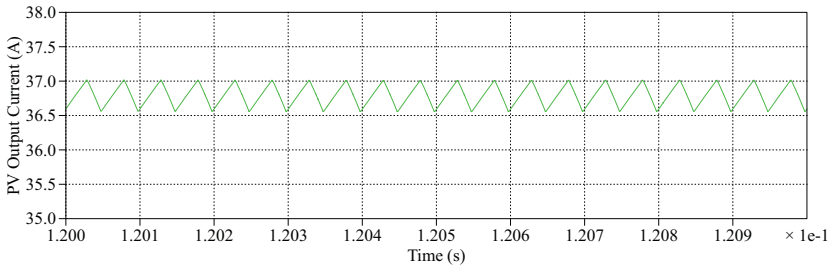

(a)

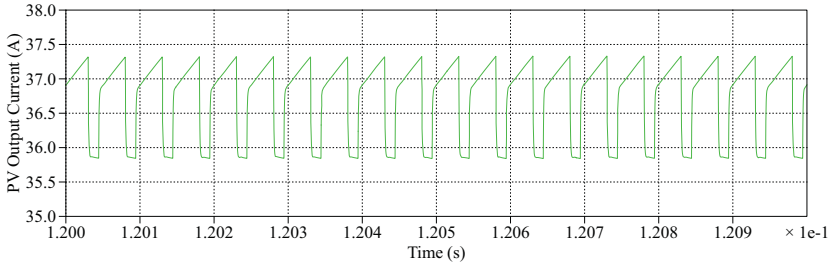

(b)

Figure 5.26. Steady-state PV current: (a) BHB, (b) flyback

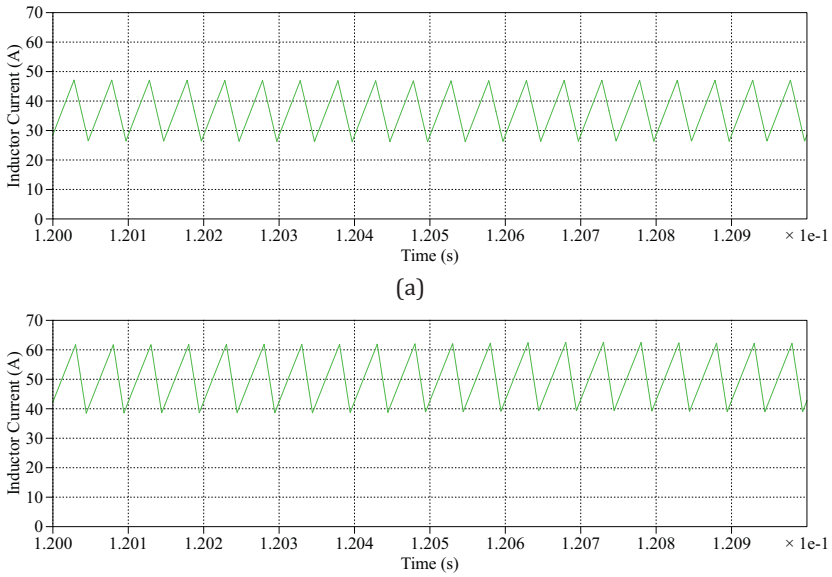

(a)

(b)

Figure 5.27. Steady-state DC/DC converter inductor current: (a) BHB, (b) flyback

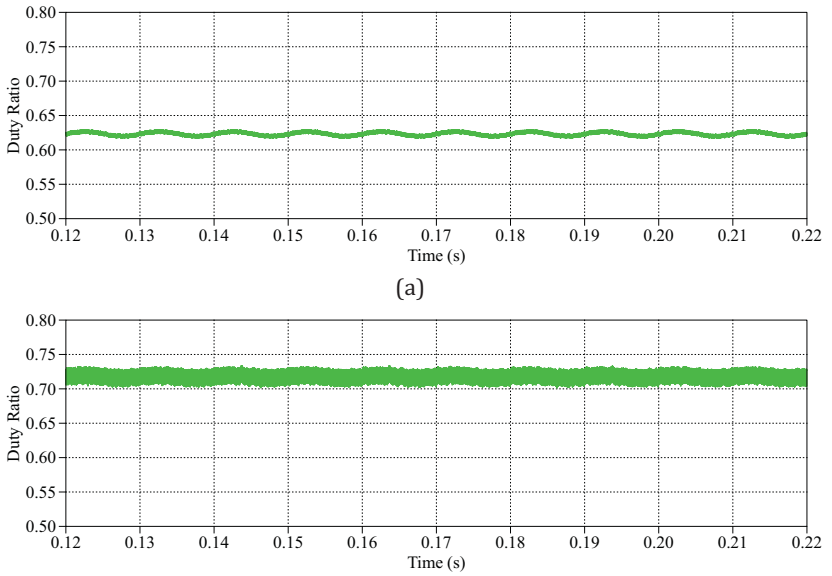

(a)

(b)

Figure 5.28. Steady-state DC/DC duty ratio: (a) BHB, (b) flyback

The CHB converter regulates the average DC-link voltage at 2 kV and the nine DC-link voltages are well balanced as shown Fig. 5.29. A second harmonic voltage ripple (100 Hz) is present on the DC-link due to the oscillatory instantaneous power [28]. The amplitude of the DC-link voltage fluctuation is less than 20 V (0.01 p.u.), which has little effect on the CHB modulation and the performance of the MPPT. The output phase voltage and the three-phase grid current waveforms of the CHB converter are shown in Fig. 5.30 and Fig.5.31, respectively. The output phase voltage of the CHB converter is composed of seven levels and the grid currents are sinusoidal with low harmonic distortion (3.2% for the BHB system and 3.3% for the flyback system).

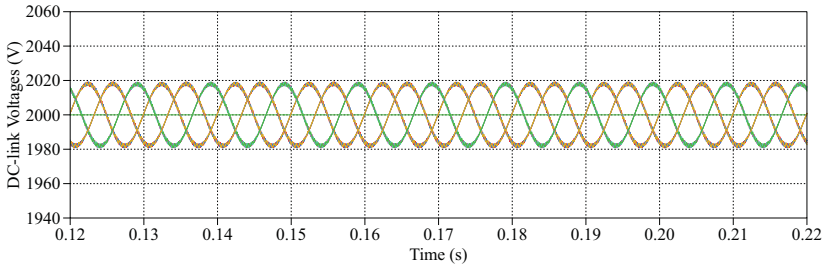

(a)

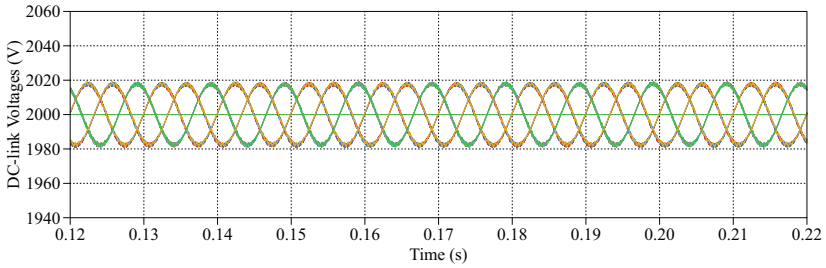

(b)

Figure 5.29. Steady-state nine DC-link voltages: (a) BHB, (b) flyback

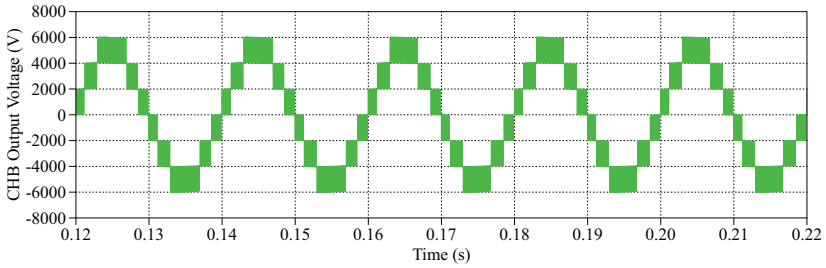

(a)

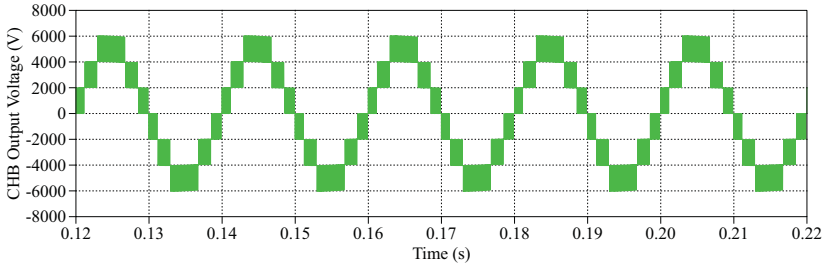

(b)

Figure 5.30. Steady-state CHB output phase voltage: (a) BHB, (b) flyback

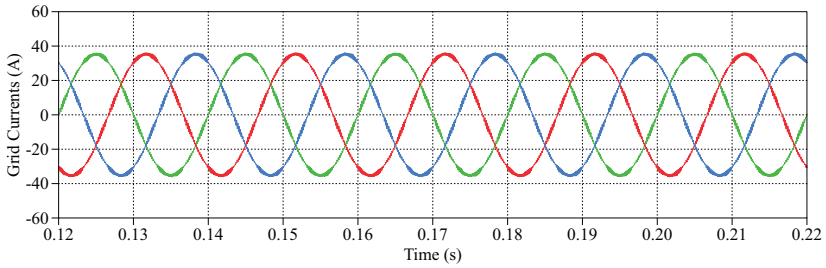

(a)

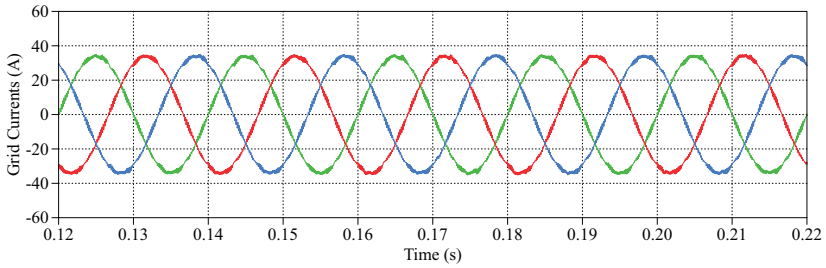

(b)

Figure 5.31. Steady-state three-phase grid currents: (a) BHB, (b) flyback

The comparison of the harmonic contents of the grid currents with the requirements of IEEE 1547, Standard for Interconnecting Distributed Resources with Electric Power Systems [116] is provided in Fig. 5.32, featuring the BHB and the flyback respectively. The results are from the same simulation period under the same conditions for both converters. The CHB converters in both implementations are capable of fulfilling the grid requirements on individual harmonic distortion for the first 40 harmonics, as required by the standard, and complying with the THD requirements. The harmonic performance of the BHB system is slightly better than the flyback system on low order harmonics, but basically they do not show significant difference.

It is worth mentioning that the high frequency harmonics which lie on the side-band of the converter switching frequency, 6 kHz in this case, are the main contributor to the current harmonic distortion. This is due to the fact that a single inductor is used as the interconnection between the converter system and the grid. Higher order filters, such as LC, LCL, are recommended if further reduction on the high frequency harmonics is required for EMI concerns. Nevertheless, increasing the power level of the system and/or expanding the CHB converter level by connecting more H-bridges in series can mitigate the effect of the harmonic currents at the switching frequencies.

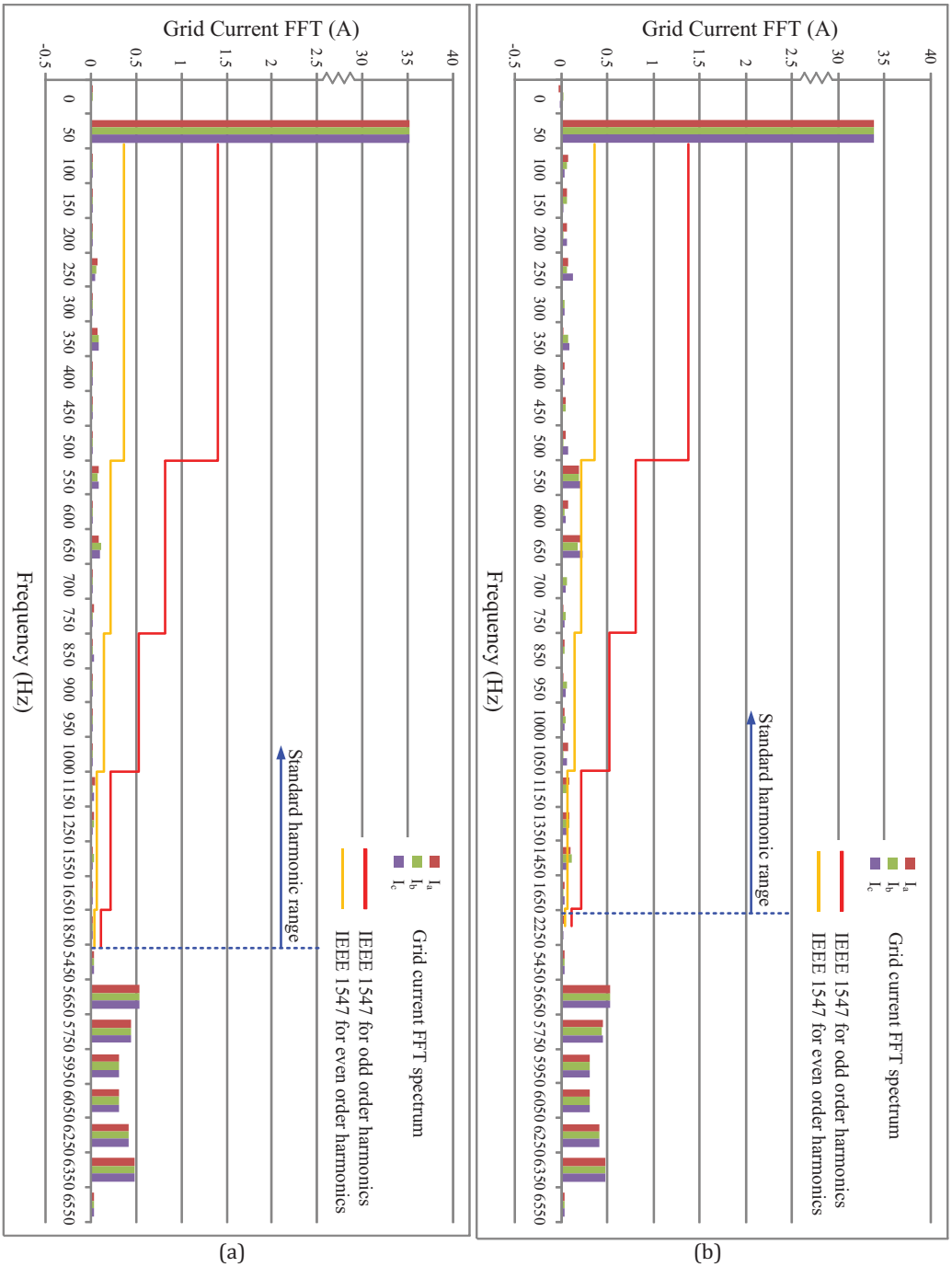

Figure 5.32. Grid current FFT spectrum with comparison to the IEEE standard 1547: (a) CHB PV system with the BHB, (b) CHB PV system with the flyback

5.4.2.2 Operation in a wide input voltage range

In this study, the process of variations in PV voltage include the start-up ramp as in the first case, and a second ramp from the nominated MPP voltage of 794.6 V (1 kW/m^2, 25°C) to the lower limit of the MPP range, specifically 450 V, considered based on industry practices [83]. Two steady-state operation periods are involved, with the PV voltage kept at 794.6 V and 450 V respectively. The operating point of the PV array moves from point A to B and then from B to C along the characteristic curve shown in Fig. 5.24. During the ramp changes and at different PV operating points, dynamic and steady-state responses of both DC/DC converters and the CHB converter are shown from Fig. 5.33 to Fig. 5.40.

Both of the DC/DC converters are capable of following the PV voltage reference with high accuracy, which can be seen from Fig. 5.33. The duty ratio is well controlled to accommodate the reduction of power delivered by the PVs, as shown in Fig. 5.37 and Fig. 5.35 respectively. The results indicate that both of the DC/DC converters can cope with the situation of low input voltage from the PV sources by increasing the converter voltage gain, and can track the PV voltage in the lower voltage range with high accuracy. In addition, both converters are capable of eliminating the PV panel leakage currents during the steady-state operation and the transients.

The CHB converter is capable of maintaining the average of the DC-link voltages to the reference value of 2 kV while keeping them well balanced, as can be seen in Fig. 5.38. The initial overshoot and subsequent 100 Hz ripple both remain below 25 V (0.0125 p.u.). The CHB converter is capable of delivering good quality output currents during the process of PV power and voltage variations, as shown in Fig. 5.40. The grid currents are in good sinusoidal shape with less than 5A initial overshoot during the startup and are regulated to lower amplitude when less power is extracted from the PV arrays. The system performance can be further enhanced at higher power levels, where the percentage of harmonic contents in the grid currents is reduced due to the increase in the fundamental components.

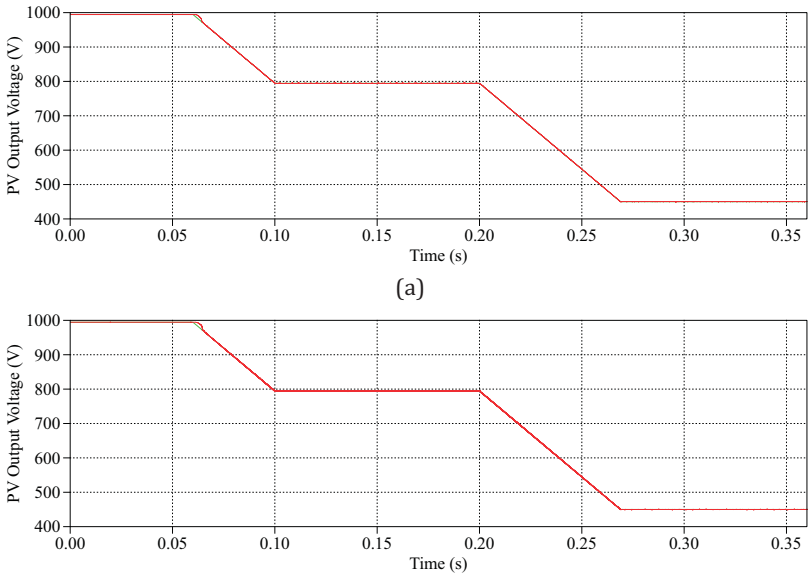

(a)

(b)

Figure 5.33. PV voltage: (a) BHB, (b) flyback

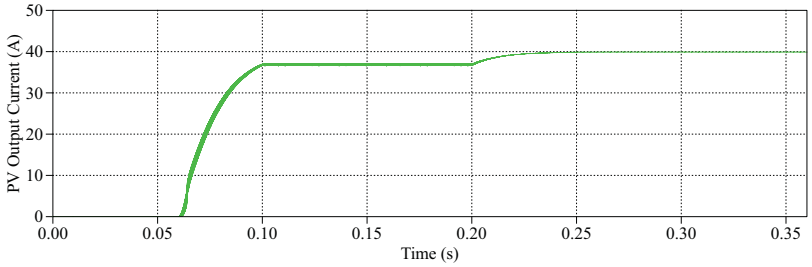

(a)

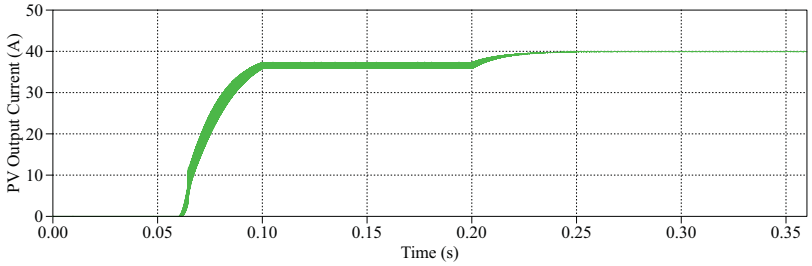

(b)

Figure 5.34. PV current: (a) BHB, (b) flyback

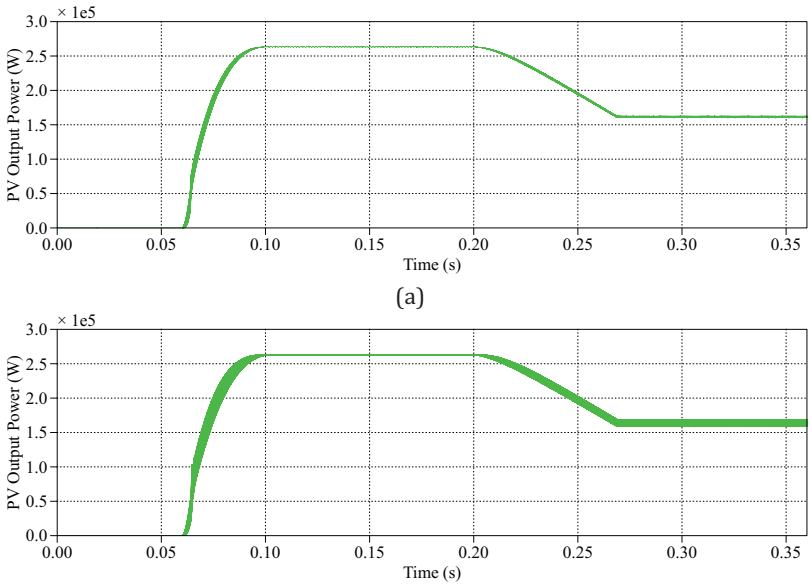

(a)

(b)

Figure 5.35. PV output power: (a) BHB, (b) flyback

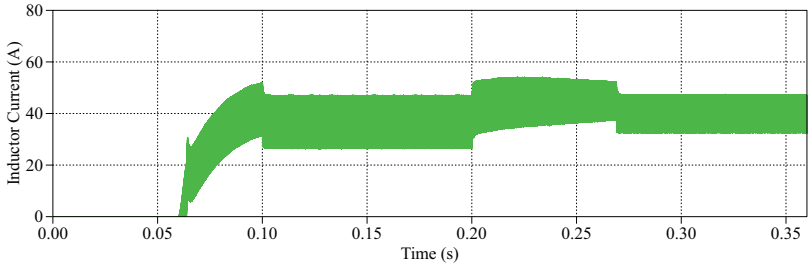

(a)

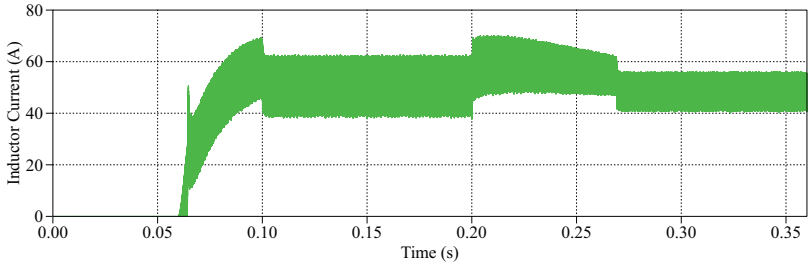

(b)

Figure 5.36. DC/DC converter inductor current: (a) BHB, (b) flyback

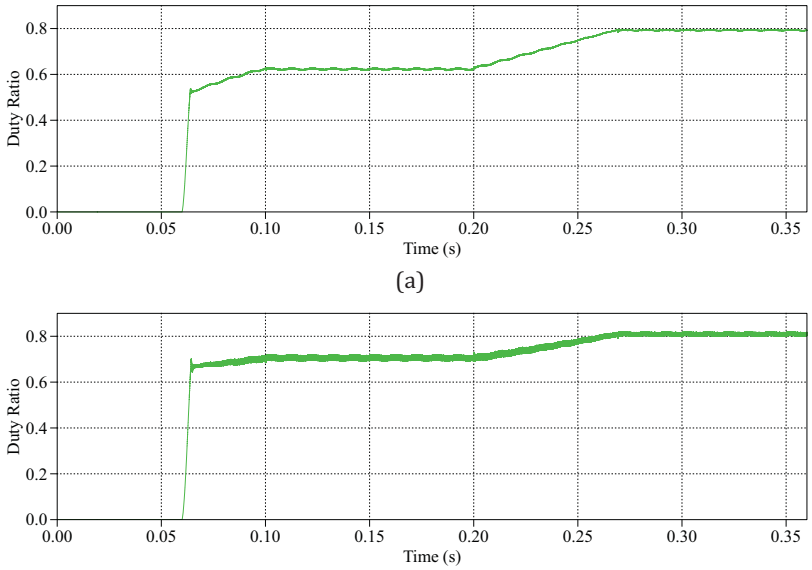

(a)

(b)

Figure 5.37. DC/DC duty ratio: (a) BHB, (b) flyback

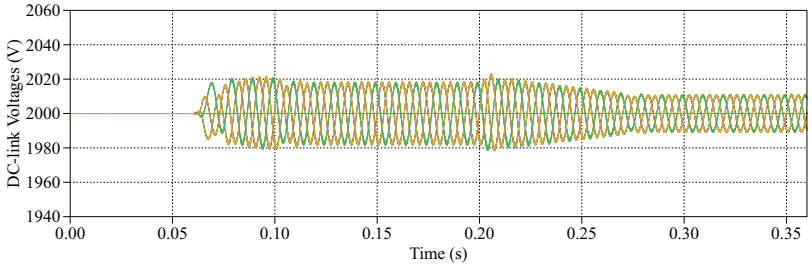

(a)

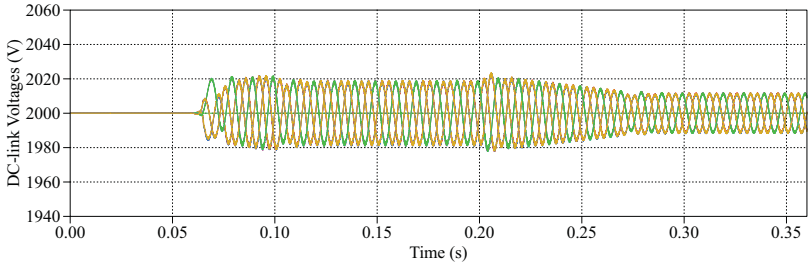

(b)

Figure 5.38. Nine DC-link voltages: (a) BHB, (b) flyback

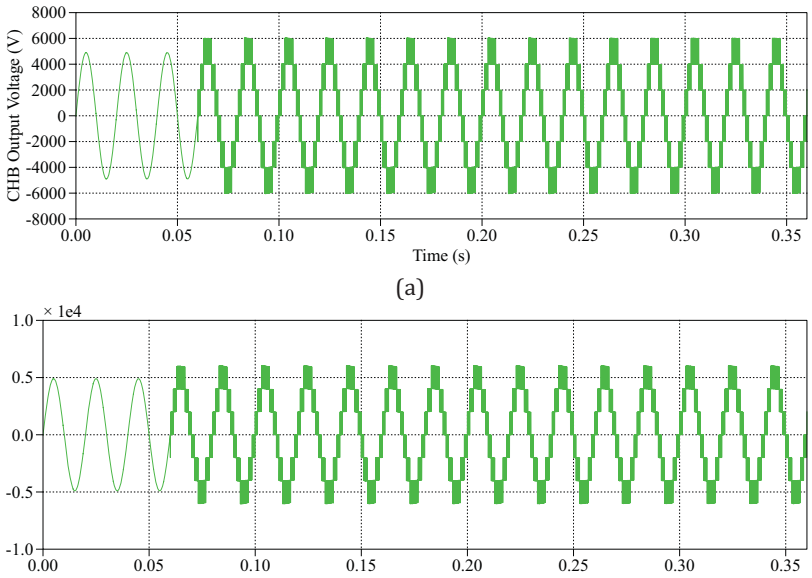

Figure 5.39. CHB output phase voltage: (a) BHB, (b) flyback

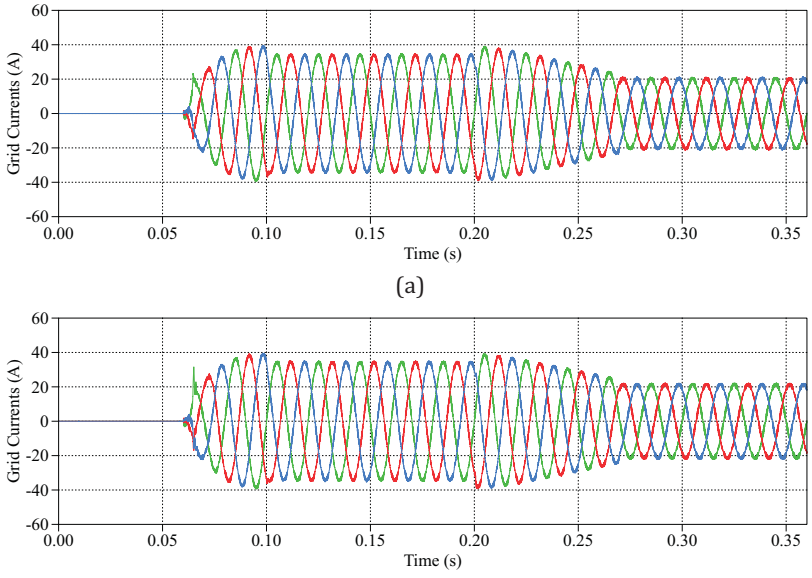

Figure 5.40. Three-phase grid currents: (a) BHB, (b) flyback

Additionally, a closer look at the DC-link voltage and current of a corresponding H-bridge power cell (top cell in phase A as an example) is shown in Fig. 5.41, featuring detailed interrelation between the two. As can be seen, the DC-link voltage and current both have a sinusoidal envelope and are correlated all the time. When the DC voltage stays above average value (2 kV), more power is drawn from the DC-link; when the DC voltage drops below average value, less power is drawn from the DC-link. On the other hand, the profile of the variation of the DC voltage reflects the variation tendency of the DC current envelope.

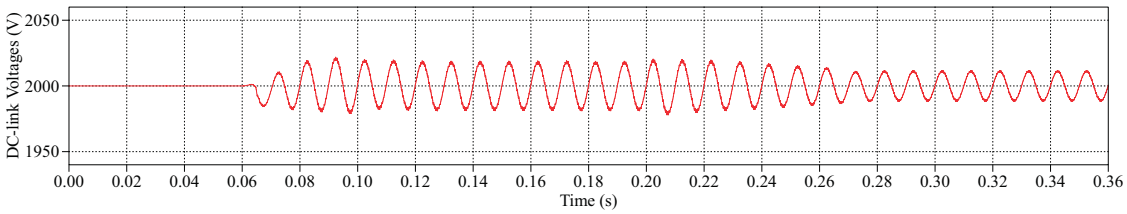

(a)

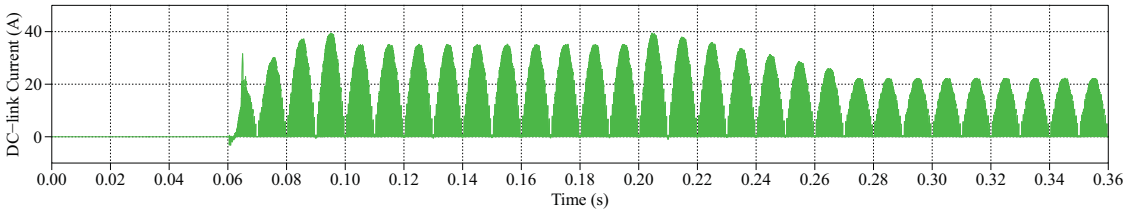

(b)

Figure 5.41. DC-link voltage and current interrelation

5.5 Case study 4: Raising power capacity by CHB extension featuring different control approaches

5.5.1 Case study description

The high voltage and power capability have been investigated in Chapter 3 based on the 3 MW simulation model featuring a 13-level CHB converter topology. By means of extending the number of series connected H-bridges, the CHB converter is capable of incorporating more DC sources and connecting to higher voltage grids. In this section, a 13-level three-phase CHB converter is used to integrate 2.63 MW_P rated PV power to the 10 kV AC grid. The control system employs two different methods for evaluation. One approach is through PI controllers in the dq frame and the other is through PR controllers in the $\alpha\beta$ frame. Both of the control methods have been discussed in Chapter 3 and will be evaluated in this section for the PV integrated converter system.

The system configuration is depicted in Fig. 5.42. The system consists of 18 sections of PV arrays arranged with their corresponding DC/DC converters for MPPT and isolation from the grid. Each section contains five PV arrays with their individually associated DC/DC converters. The DC/DC converters in the same section are connected to the CHB converter through

a common DC-bus. The 13-level three-phase CHB converter incorporates the 18 sections of PV generators and converts the DC power collected from the DC-buses to grid compatible AC power. The control structures of the two different approaches are shown in Fig. 5.43(a) and Fig. 5.43(b) based on VOC in the synchronous rotating reference frame and in the stationary reference frame respectively.

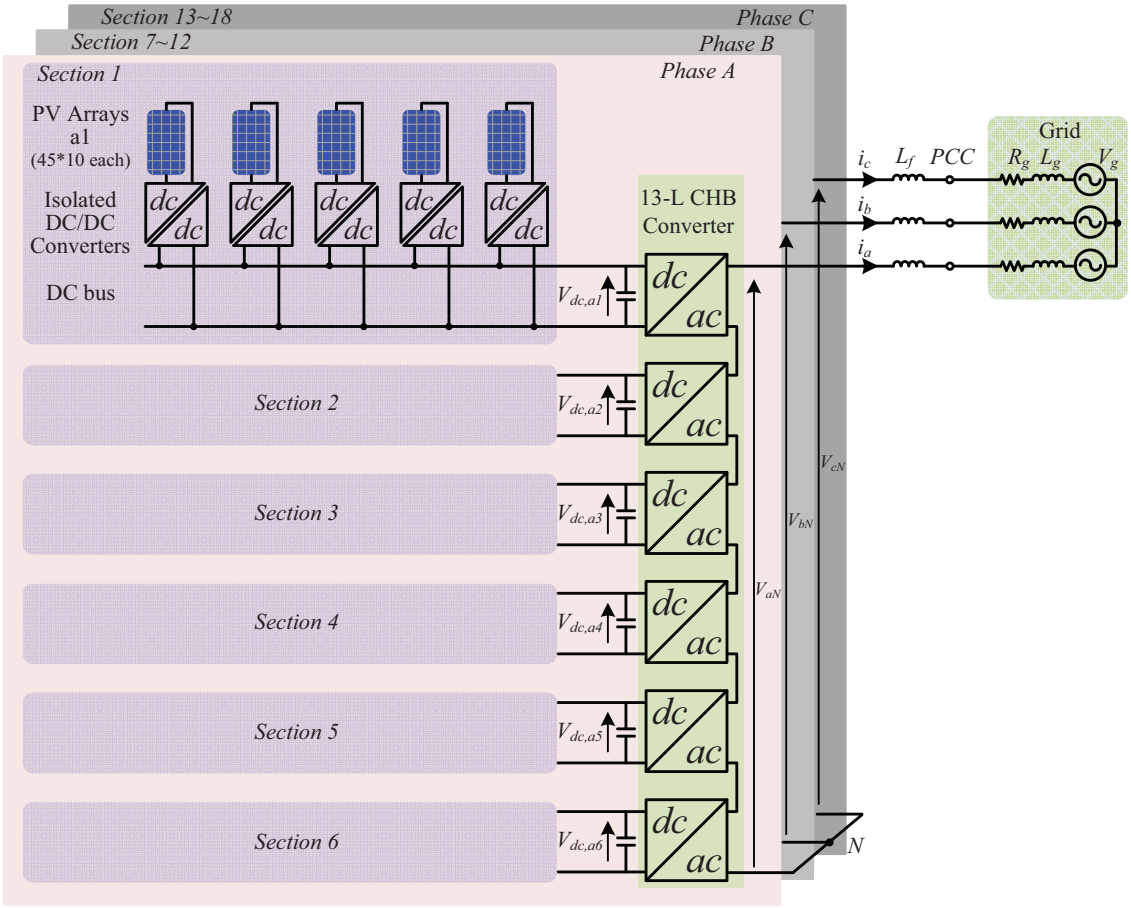

Figure 5.42. Configuration of the grid-connected PV system featuring the 13-L CHB converter with isolated DC/DC converters

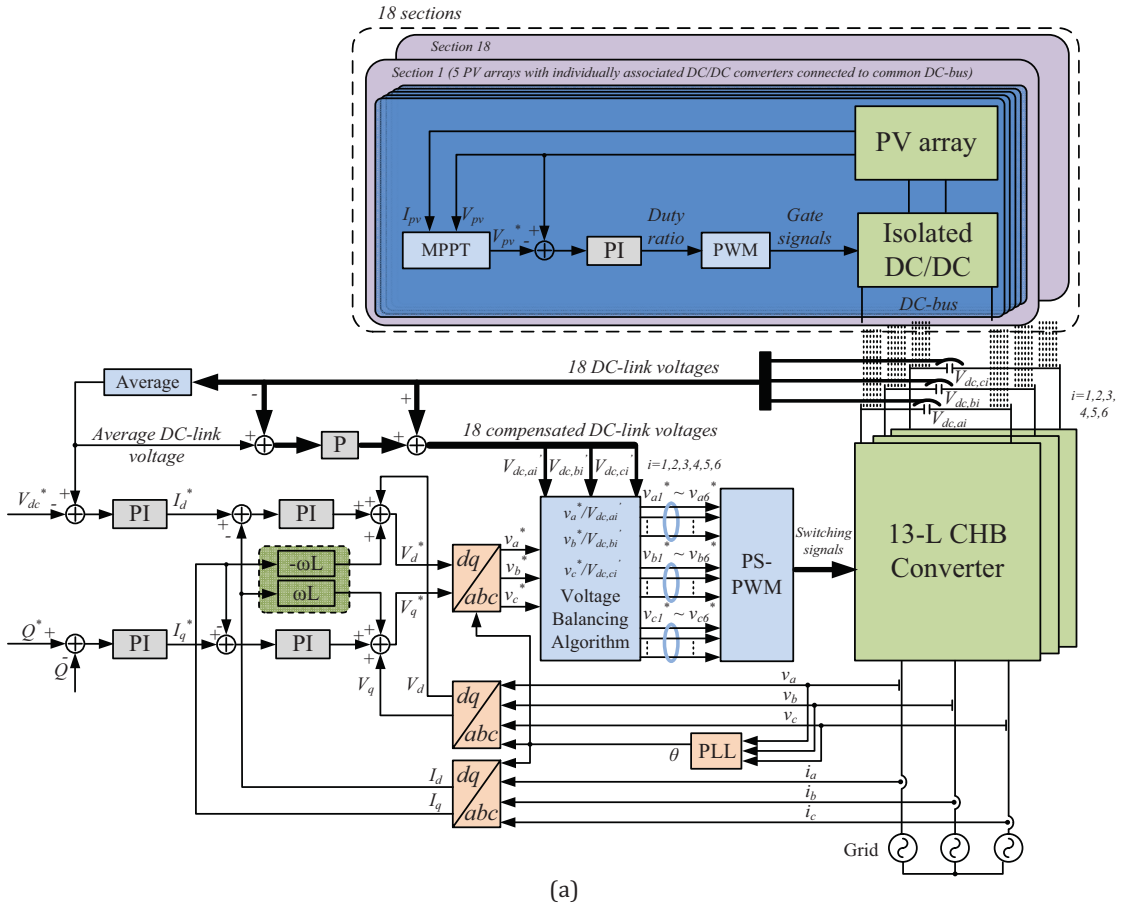

(a)

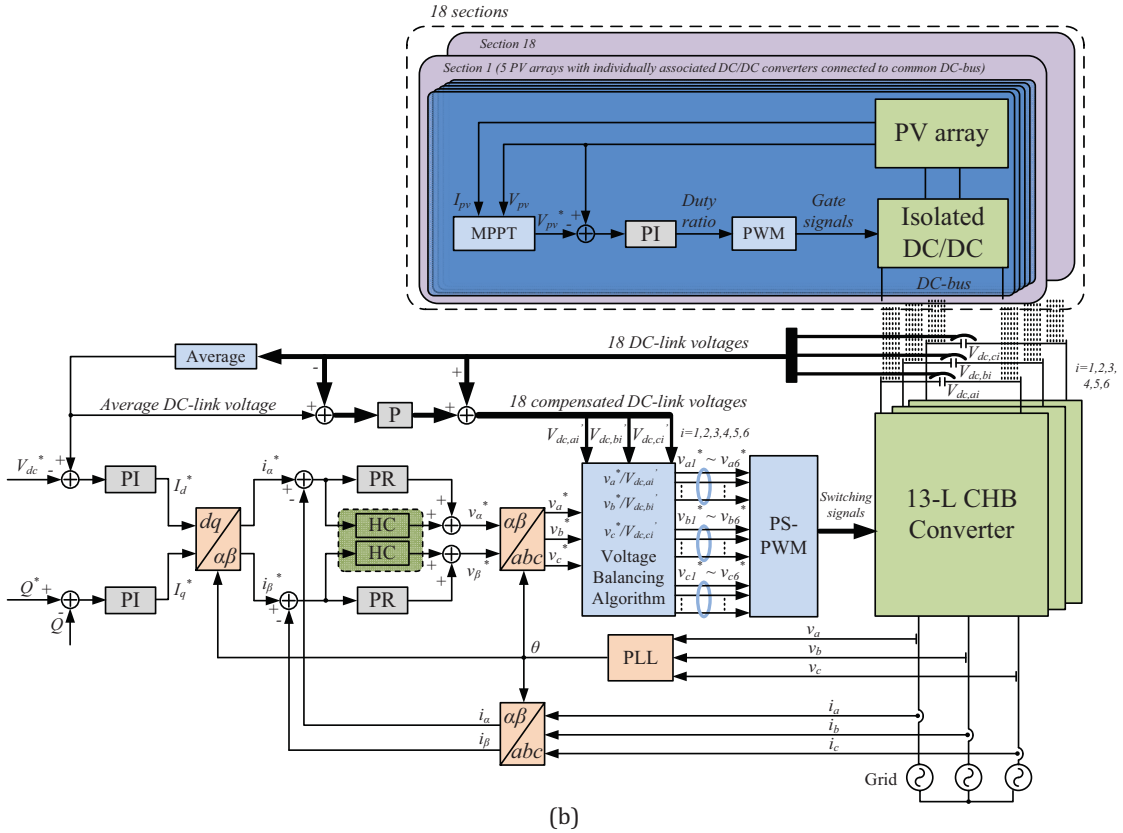

(b)

Figure 5.43. Control structure of the 13-L CHB grid-connected PV system: (a) synchronous frame VOC with PI controllers (b) stationary frame VOC with PR controllers

The system specifications are listed in Table 5.4. The 13-level CHB converter has double the amount of cascaded H-bridge power cells in each converter phase of its 7-level version. Instead of each DC/DC converter connected to an H-bridge power cell through an individual DC-link, five DC/DC converters are parallel-connected through a common DC-bus to the same H-bridge power cell. In this way, the 13-level CHB converter is able to integrate 10 times the PV power of the 7-level counterpart, given that the PV array configuration stays the same. With higher current rating of the converter, the filter size could be reduced while equally good power quality being achieved. The 13-level CHB converter connects the PV system to the 10 kV grid with 1.5 kV of the DC-bus voltage; while the 7-level CHB converter connects to the 6 kV grid with 2 kV of the DC-link voltage. By extending the voltage level of the CHB converter, higher power and voltage capability is achieved. Additionally, lower DC voltage alleviates the voltage boosting by the DC/DC converters so that they work with a lower duty ratio. The system configuration and component values are the same when using different control methods. The parameters of the PI and PR controllers are tuned to achieve the best performance individually.

Table 5.4. Simulation parameters - Case study 4

PV module (BP 365)		**CHB converter**	
Maximum Power P_{MPP}	65 W	Number of series-connected H-bridges per phase (k)	6
MPP Voltage V_{MPP}	17.67 V	Levels of the converter ($n = 2k + 1$)	13
MPP Current I_{MPP}	3.68 A	Switching frequency f_s	500 Hz
Open circuit voltage V_{OC}	22.04 V	DC-link voltage V_{dc}	1.5 kV
PV array		Rated Power	3 MW
Array configuration (Series $\times$ Parallel)	45$\times$10	Grid-side filter L_f	3 mH
Maximum Power P_{MPP}	29.25 kW	**DC/DC converter**	
MPP Voltage V_{MPP}	794.6 V	Converter topology	Flyback
MPP Current I_{MPP}	36.8 A	Switching frequency	20 kHz
Open circuit voltage V_{OC}	994.5 V	Input inductor	1.22 mH
Grid		Output Capacitor	1.25 mF
Grid voltage (line-line RMS)	10 kV	High-frequency transformer turns ratio ($N_S : N_P$)	1:1
Fundamental Frequency	50 Hz	Rated Power	30 kW
Grid Impedance	R_g =1.5 mΩ, L_g =48 μH	Number of DC/DC converters at the DC bus of each H-bridge	5

5.5.2 Simulation results

The controllers' steady-state performance of both control methods is shown from Fig. 5.44 to Fig. 5.48. The performance of the PI controllers in the dq frame is as follows: Fig. 5.44 (a) and Fig. 5.45 (a) show the I_d and I_q components of the converter system respectively; Fig. 5.46(a) shows the generated V_d and V_q referencing signals from the PI current controllers; Fig. 5.47 (a) shows the three-phase voltage referencing signals transformed from the V_d and V_q signals. The performance of the PR controllers in the $\alpha\beta$ frame is as follows: Fig. 5.44(b) and Fig. 5.45(b) show the i_α and i_β components of the converter system respectively; Fig. 5.46(b) shows the generated v_α and v_β from the PR current controllers; Fig. 5.47 (b) shows the three-phase voltage referencing signals transformed from the v_α and v_β signals. Fig. 5.48 shows the modulation indices generated by the three-phase voltage referencing signals through the DC balancing algorithm in both control schemes respectively. Although through different referencing frames via different controllers, both control schemes give very similar three-phase voltage referencing signals and generate very similar modulation indices for the modulator. From Fig. 5.44 to Fig. 5.48 it can be seen that the controllers in both control schemes give accurate responses and can fulfill the control tasks required for the system.

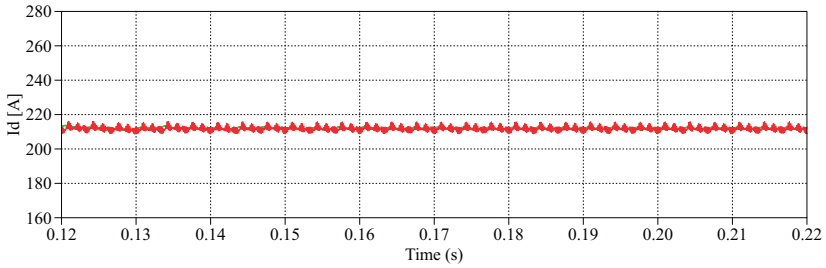

(a)

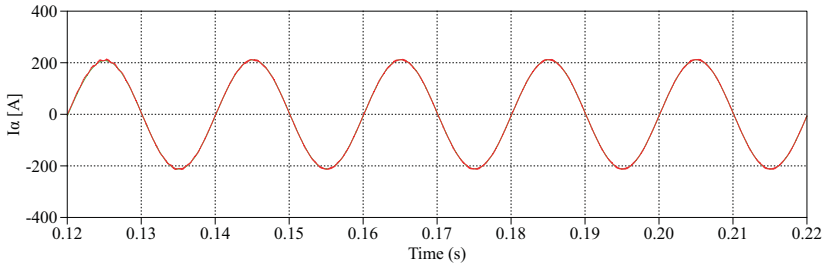

(b)

Figure 5.44. Current controller:(a) synchronous frame VOC with PI controllers: I_d, (b) stationary frame VOC with PR controllers: i_α

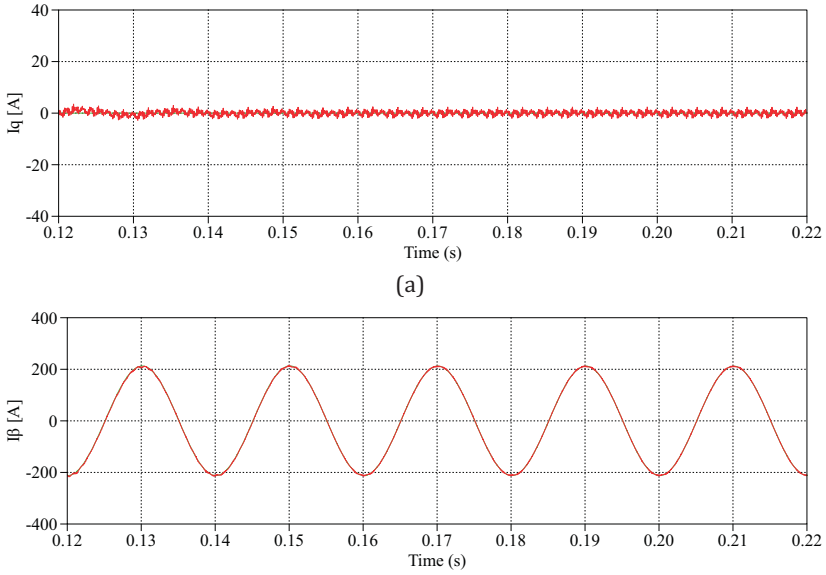

Figure 5.45. Current controller:(a) synchronous frame VOC with PI controllers: I_q, (b) stationary frame VOC with PR controllers: i_β

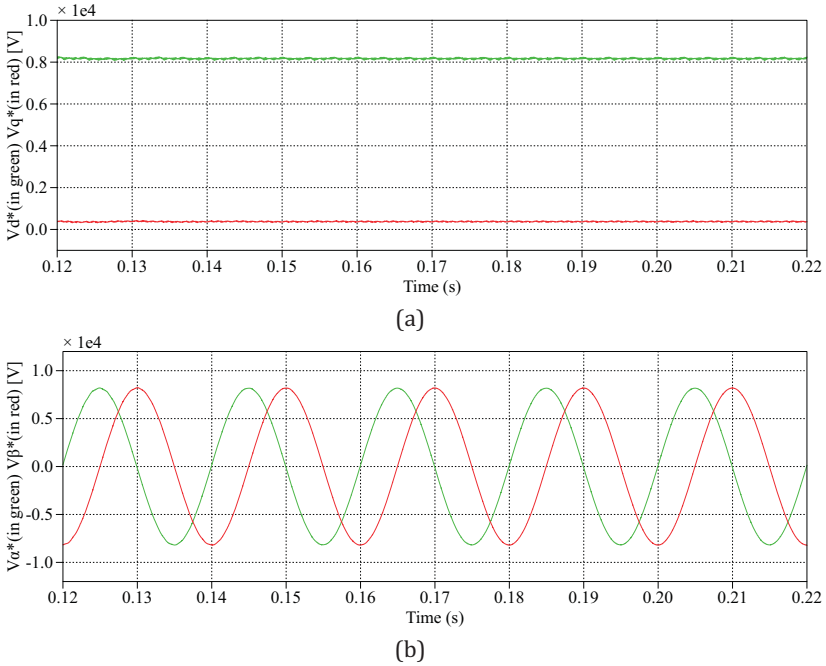

Figure 5.46. Current controllers:(a) synchronous frame VOC with PI controllers: V_d and V_q control signals, (b) stationary frame VOC with PR controllers: v_α and v_β control signals

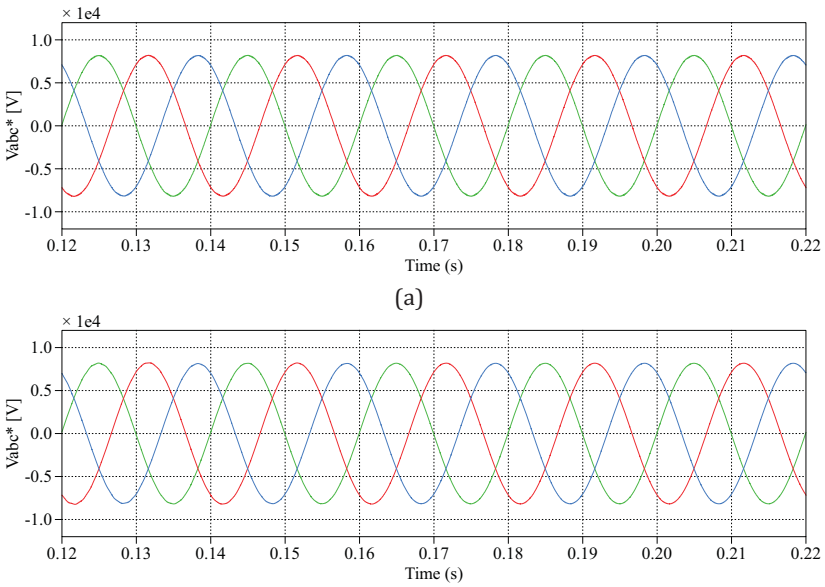

Figure 5.47. Three-phase voltage referencing signals: (a) synchronous frame VOC, (b) stationary frame VOC

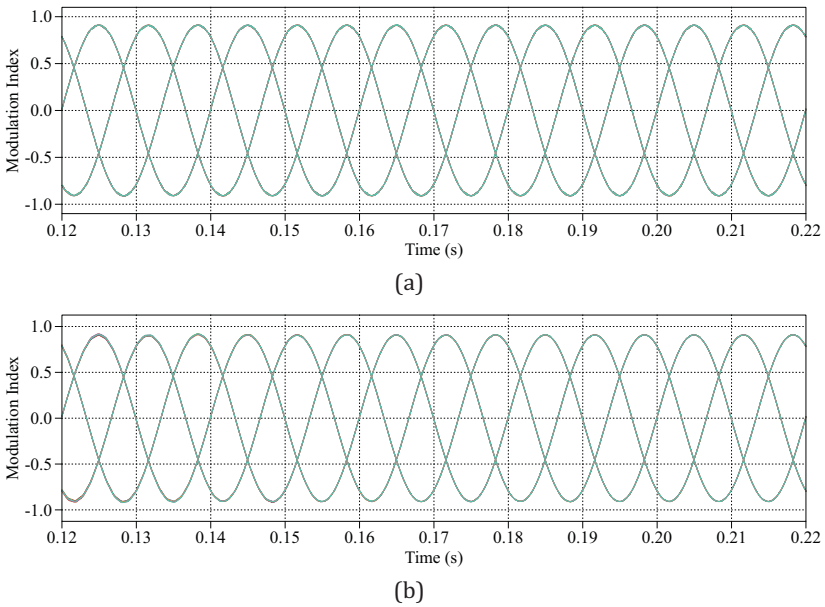

Figure 5.48. Modulation index: (a) synchronous frame VOC, (b) stationary frame VOC

The converter system steady-state performance through both control approaches is shown from Fig. 5.49 to Fig. 5.55. The output voltage and current of the PV arrays are shown in Fig. 5.49 and Fig. 5.50 respectively. The inductor current and the duty ratio of the DC/DC converters is shown in Fig. 5.51 and Fig. 5.52 respectively. The DC-bus voltages, the stepped output voltage waveforms of the CHB converter and the grid currents are shown in Fig. 5.53, Fig. 5.54, and Fig. 5.55, respectively. It can be seen that both of the control methods provide equally good performance on regulating the DC-bus voltage and the grid currents. The converter system under both control schemes can extract the maximum power out of the PV sources and inject good quality currents to the grid.

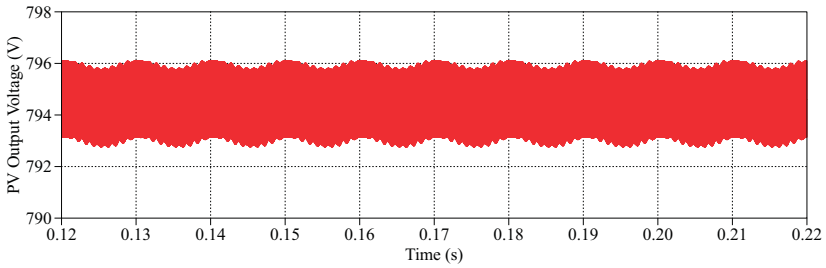

(a)

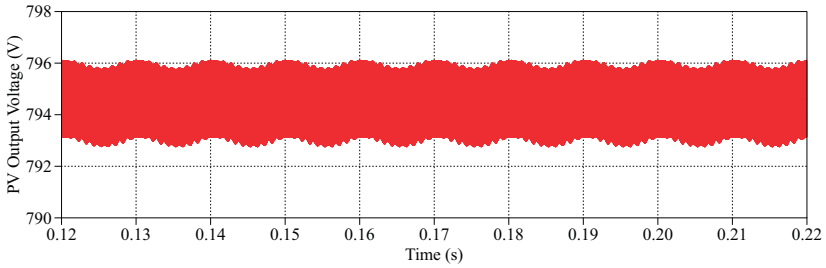

(b)

Figure 5.49. PV voltage: (a) synchronous frame VOC, (b) stationary frame VOC

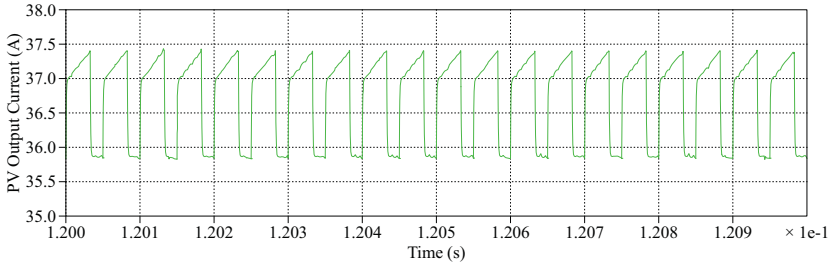

(a)

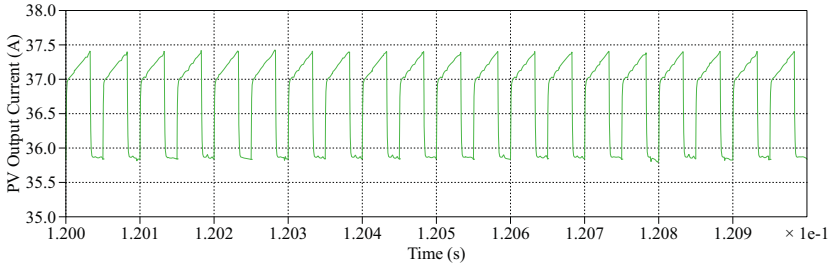

(b)

Figure 5.50. PV current: (a) synchronous frame VOC, (b) stationary frame VOC

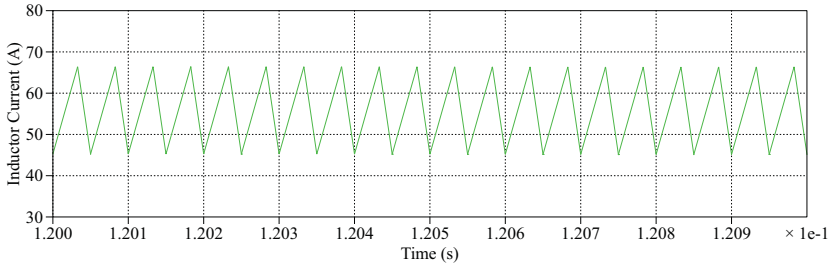

(a)

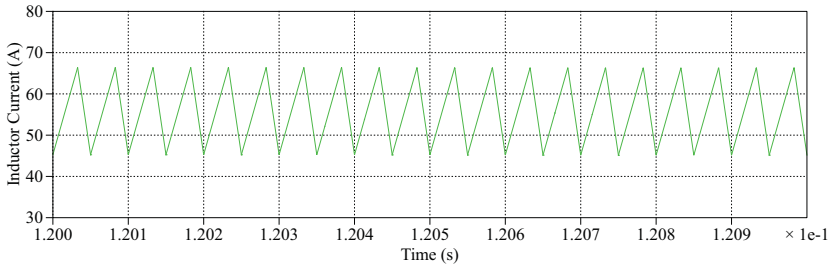

(b)

Figure 5.51. DC/DC converter inductor current: (a) synchronous frame VOC, (b) stationary frame VOC

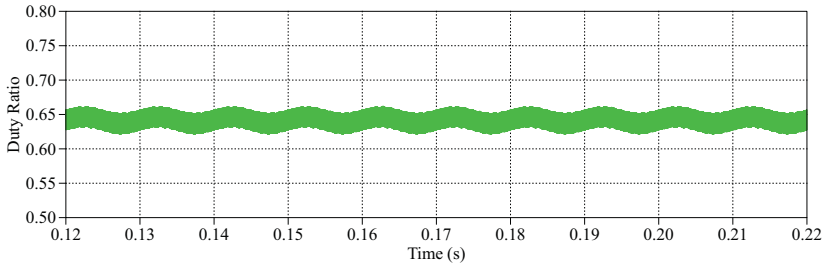

(a)

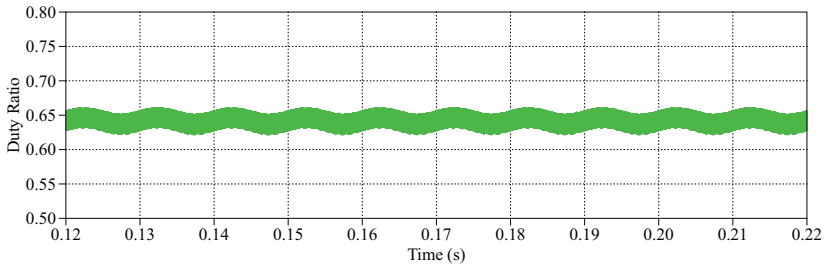

(b)

Figure 5.52. DC/DC duty ratio: (a) synchronous frame VOC, (b) stationary frame VOC

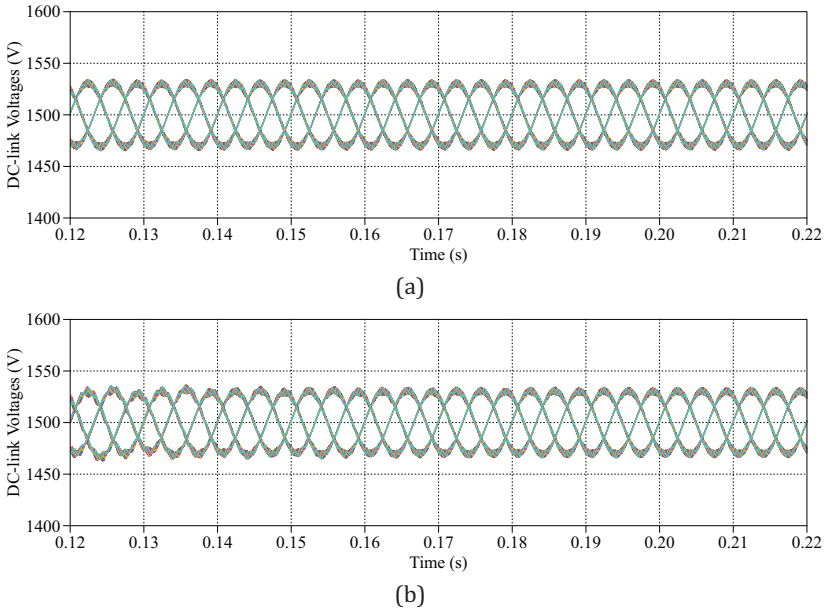

(a)

(b)

Figure 5.53. Eighteen DC-link voltages: (a) synchronous frame VOC, (b) stationary frame VOC

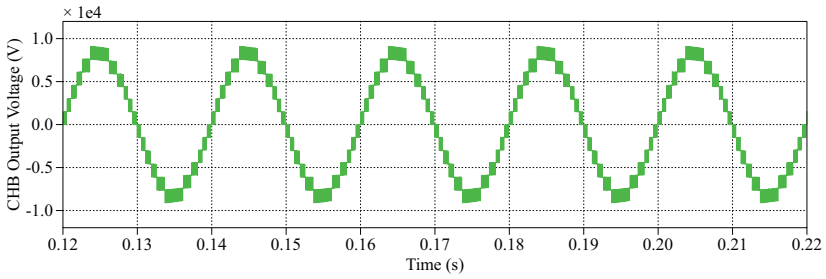

(a)

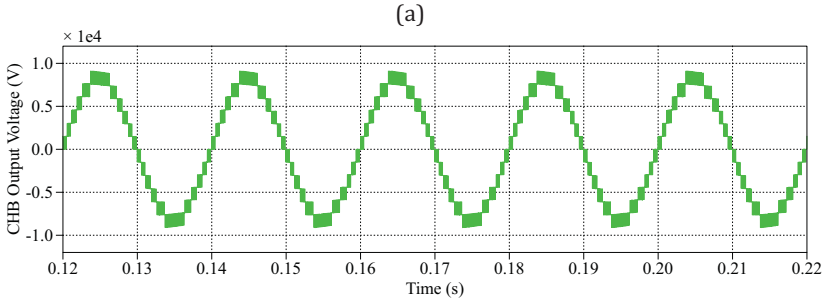

(b)

Figure 5.54. 13-Level CHB output phase voltage: (a) synchronous frame VOC, (b) stationary frame VOC

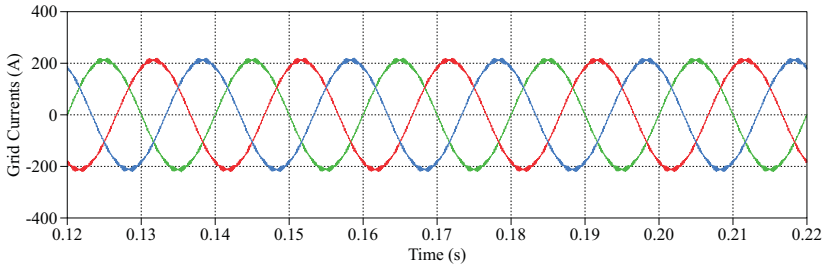

(a)

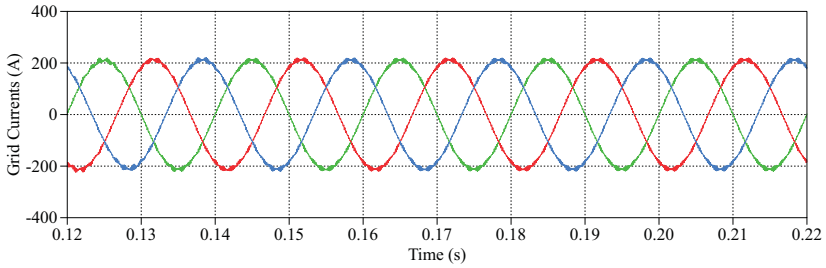

(b)

Figure 5.55. Three-phase grid currents: (a) synchronous frame VOC, (b) stationary frame VOC

The comparison of the grid current harmonics with the requirements of IEEE 1547 [116] is provided in Fig. 5.56, featuring the synchronous frame VOC and the stationary frame VOC respectively. The CHB converters under both control schemes are capable of fulfilling the grid requirements on individual harmonic distortion for the first 40 harmonics, as required by the standard, and complying with the THD requirements. The harmonic performance between the two control schemes do not show significant difference. It is worth noticing that the 6 kHz side-band harmonics (12 times the 500 Hz switching frequency), which lie on the higher frequency range than concerned by the standard, are the main contributor to the current distortion. This can simply be improved by adding a more advanced grid filter, such as LC, LCL. Nevertheless, compared with its 7-L version, the 13-L CHB converter system has better harmonic performance with lower device switching frequency and lower device ratings while connecting to higher voltage grids with higher power capacity.

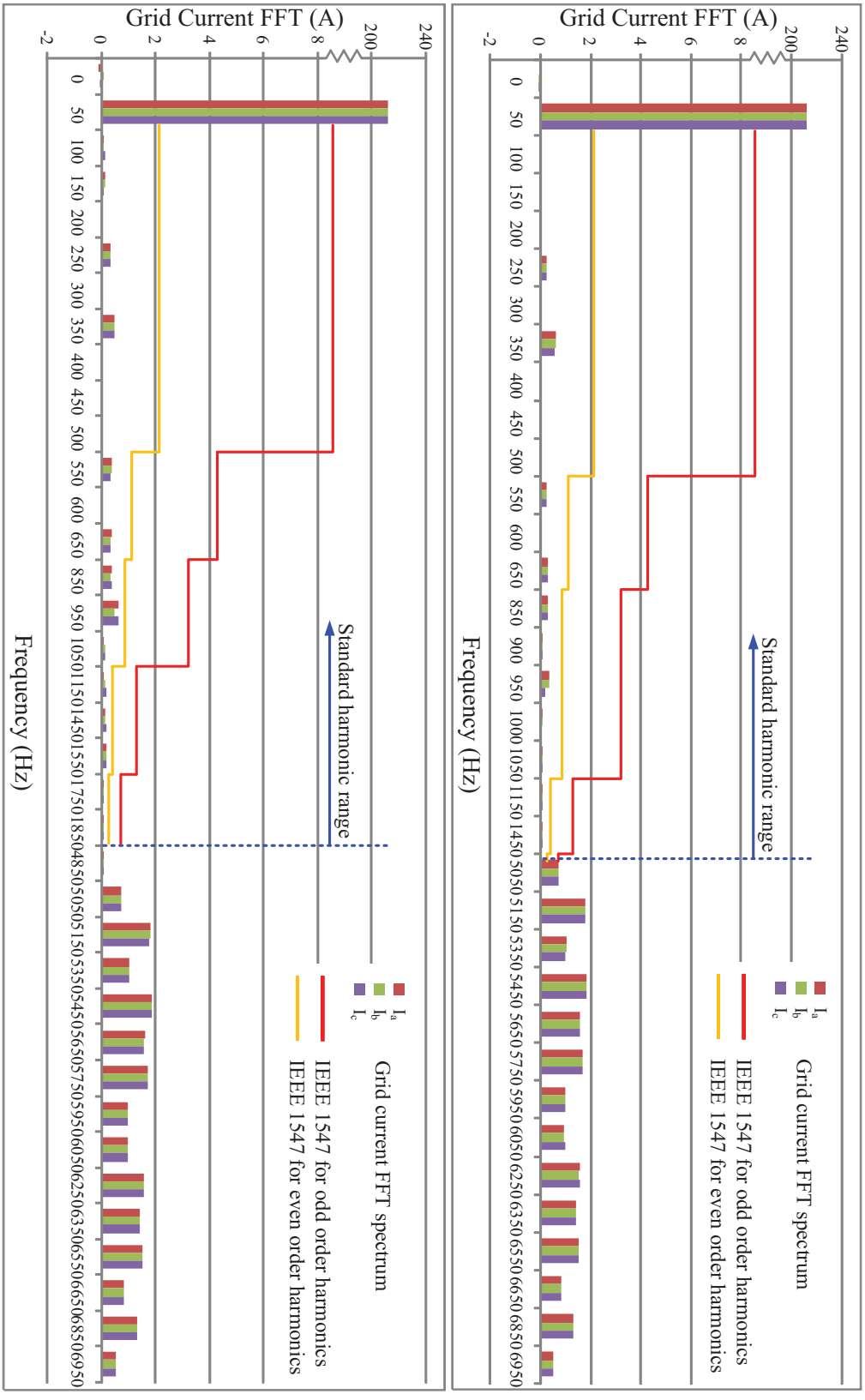

Figure 5.56. Grid current FFT spectrum with comparison to the IEEE standard 1547: (a) synchronous frame VOC, (b) stationary frame VOC

Chapter 6

Conclusions and Future Work

6.1 Summary

In this work, large-scale solar PV grid-integration featuring the CHB converter with isolated DC/DC converters is investigated. An overview of the PV system architecture and the PV inverter topologies is provided. The working principles, modulation techniques and control scenarios of the classic multilevel converter topologies are explored, especially that of the CHB converter are simulated and discussed. Two isolated DC/DC converters, namely the BHB and the flyback, are simulated and analyzed. The grid-connected PV system featuring the CHB converter with isolated DC/DC converters is investigated through case studies featuring different voltage and power ratings and control structures. The system performance is evaluated and discussed.

6.2 Conclusions

The CHB converter proves to be a suitable option for connecting large-scale PV power systems to medium-voltage grids. It offers a modular solution with a highly flexible system structure. Through the simulation studies carried out in this work, the CHB converter is capable of power levels of 300 kW and 3 MW, catering to voltage levels of 6 kV and 10 kV respectively, providing good quality power with low harmonic distortion (under 3%). The PS-PWM is implemented in the CHB converter and the VOC control method is applied to the system in the synchronous rotating frame and in the stationary frame respectively. PI controllers and PR controllers are implemented in the two control schemes respectively. Both types of controllers are capable of fulfilling the control tasks on regulating the DC voltages and grid currents, providing accurate steady-state operation and fast response during dynamics.

The two isolated DC/DC converters, the BHB and the flyback, are evaluated on the performance of MPPT for the PV arrays. Both converters are able to perform MPPT under STC and tracking varying PV voltage in a wide range. The BHB converter offers better MPPT efficiency due to smaller ripple on the control signals and less fluctuation around the required operating points than the flyback, however at the expense of increased component count and the power loss on the leakage inductance. Both converters are able to follow a wide range of input voltages fast and precisely. The BHB works at a lower range of inductor current and

duty ratio than the flyback, leading to better reliability and stability of the system.

The CHB converter with isolated DC/DC converters for the grid integration of large-scale PV systems is investigated through four simulation studies. It proves that the galvanic isolation between the PV and the grid is essential to prevent the leakage currents and PID of the PV modules. The CHB converter system with isolated DC/DC converters is capable of performing MPPT for the PV arrays under varying solar irradiance. The CHB converter is capable of balancing the DC-link voltages and regulating the grid currents in accordance with the grid codes.

Both types of isolated DC/DC converters, the BHB and the flyback, are capable of operating at MPP under STC and tracking a wide range of PV voltages when integrated into the CHB grid-connected converter system. The BHB is the building block of the multiphase DC/DC converter, which is expandable to higher voltage and power levels. This is especially advantageous for large-scale PV systems. Moreover, the ZVS and ZCS features of the BHB converter and the multiphase DC/DC converter are particularly effective in reducing the switching losses associated with the devices which lead to higher efficiency, making this type of DC/DC converers more attractive for this application.

The grid-connected PV system topology featuring the CHB converter with isolated DC/DC converters is capable of higher voltage and power levels by the expansion of the CHB converter. The thirteen-level CHB converter has been investigated on integrating 3 MW of PV power to the 10 kV grid. DC/DC converters are arranged in parallel on the DC-buses, transferring the PV power to the CHB converter and feed into the grid. The system is capable of balancing the DC-bus voltages and controlling the grid currents according to the regulations, injecting good quality power to the distribution networks.

6.3 Future work

Power converters in PV systems rarely operate under ideal conditions. Partial shading and rapidly moving clouds, dust and PV module deterioration create additional challenges for PV systems. Future work should take these into consideration and investigate the operation and behavior of the CHB converter with unequal energy yield from different PV generator zones and power imbalance between the converter phases as well as the H-bridge power cells. Control strategies should be developed in order to harvest the PV generation with optimal yield while retaining efficient operation of the CHB converter.

Energy storage elements are necessary to cope with the intermittent nature and the increasing penetration of renewable energy generation. Advanced battery technologies can assist the integration of these variable resources and enhance the power quality of the grid. The CHB converter is fitted for PV applications as it can integrate energy storage into its H-bridge power cells together with the PV sources. Future research on this subject should focus on the operation, performance and challenges of such systems.

The feasibility of the CHB topology for grid-connected PV systems featuring isolated DC/DC

converters should be practically demonstrated. The performance of the two DC/DC converters integrated with the CHB converter should be investigated through experimental work, initially on a small-scale, low-power laboratory prototype, and then extended to full-scale converters. Based on the experimental results, comparisons regarding the behavior and efficiency of the two DC/DC converters can be made and used for their evaluation.

Additionally, advanced grid filters should be designed to provide improved harmonic performance with reduced filter size. Future work should consider higher order filters such as LC and LCL. The harmonic performance and the stability of the CHB converter system should be evaluated when such filters are implemented.

Furthermore, as specified in some countries' grid codes, PV systems should offer grid support for voltage and frequency stablization and Fault Ride-Through (FRT) capability under grid faults. Inverters should become more intelligent in order to manage the control tasks without compromising the efficiency of energy conversion. Control algorithms delivering these functions should be developed and verified in future work.

Bibliography

[1] A. Gawel, C. Tam, and K. Breen, "Tracking clean energy progress," IEA 2012.

[2] G. Masson, M. Latour, and D. Biancardi, "Global market outlook for photovoltaics until 2016," EPIA 2012.

[3] S. Nowak, "Trends in photovoltaic applications: Survey report of selected IEA countries between 1992 and 2010," IEA-PVPS 2011.

[4] J. L. Sawin, "Renewables 2012: Global status report," REN21 2012.

[5] D. Lenardic, "Large-scale photovoltaic power plants: Annual and cumulative installed power output capacity," pvresources.com 2011.

[6] H. Schwarzburger, "PV power plants 2012: Industry guide," RENI 2012.

[7] "Trends in photovoltaic applications: Survey report of selected IEA countries between 1992 and 2010," IEA-PVPS 2011.

[8] D. Koenemann, "Inverter and PV system technology: Industry guide 2012," RENI 2012.

[9] PVCDROM, http://pveducation.org/pvcdrom

[10] S. Nema, R. K. Nema, and G. Agnihotri, "Inverter topologies and control structure in photovoltaic applications: A review," *Journal of Renewable and Sustainable Energy*, vol. 3, pp. 1-23, 2011.

[11] M. A. Eltawil and Z. Zhao, "Grid-connected photovoltaic power systems: Technical and potential problems - A review," *Renewable and Sustainable Energy Reviews*, vol. 14, pp. 112-129, 2010.

[12] M. Calais and V. G. Agelidis, "Multilevel converters for single-phase grid connected photovoltaic systems-an overview," in *Industrial Electronics, Proceedings of ISIE, IEEE International Symposium on*, 1998, pp. 224-229 vol.1.

[13] M. Calais, J. Myrzik, T. Spooner, and V. G. Agelidis, "Inverters for single-phase grid connected photovoltaic systems-an overview," in *Power Electronics Specialists Conference, PESC, IEEE 33rd Annual*, 2002, pp. 1995-2000.

[14] J. M. A. Myrzik and M. Calais, "String and module integrated inverters for single-phase grid connected photovoltaic systems - a review," in *Power Tech Conference Proceedings*, 2003, vol.2.

[15] F. Blaabjerg, R. Teodorescu, Z. Chen, and M. Liserre, "Power converters and control of renewable energy systems," presented at Plenary Speech ICPE 2004.

[16] S. B. Kjaer, J. K. Pedersen, and F. Blaabjerg, "A review of single-phase grid-connected inverters for photovoltaic modules," *Industry Applications, IEEE Transactions on*, vol. 41, pp. 1292-1306, 2005.

[17] J. M. Carrasco, L. G. Franquelo, J. T. Bialasiewicz, E. Galvan, R. C. P. Guisado, M. A. M. Prats, J. I. Leon, and N. Moreno-Alfonso, "Power-electronic systems for the grid integration of renewable energy sources: A survey," *Industrial Electronics, IEEE Transactions on*, vol. 53, pp. 1002-1016, 2006.

[18] X. Yuan and Y. Zhang, "Status and opportunities of photovoltaic inverters in grid-tied and micro-grid systems," in *Power Electronics and Motion Control Conference, IPEMC, CES/IEEE 5th International*, 2006, pp. 1-4.

[19] D. Picault, B. Raison, and S. Bacha, "Guidelines for evaluating grid connected PV system topologies," in *Industrial Technology, ICIT, IEEE International Conference on*, 2009, pp. 1-5.

[20] H. Hu, S. Harb, N. Kutkut, I. Batarseh, and Z. J. Shen, "Power decoupling techniques for micro-inverters in PV systems-a review," in *Energy Conversion Congress and Exposition (ECCE)*, 2010, pp. 3235-3240.

[21] R. C. Variath, M. A. E. Andersen, O. N. Nielsen, and A. Hyldgard, "A review of module inverter topologies suitable for photovoltaic systems," in *IPEC, Conference Proceedings*, 2010, pp. 310-316.

[22] C. Citro, A. Luna, J. Rocabert, R. S. Munoz-Aguilar, I. Candela, and P. Rodriguez, "Overview of power processing structures for embedding energy storage in PV power converters," in *IECON, 37th Annual Conference on IEEE Industrial Electronics Society*, 2011, pp. 2492-2498.

[23] M. A. G. de Brito, L. P. Sampaio, L. G. Junior, and C. A. Canesin, "Research on photovoltaics: Review, trends and perspectives," in *Power Electronics Conference (COBEP)*, 2011, pp. 531-537.

[24] M. Saghaleini, A. K. Kaviani, B. Hadley, and B. Mirafzal, "New trends in photovoltaic energy systems," in *Environment and Electrical Engineering (EEEIC), 10th International Conference on*, 2011, pp. 1-4.

[25] Y. Xue, K. C. Divya, G. Griepentrog, M. Liviu, S. Suresh, and M. Manjrekar, "Towards next generation photovoltaic inverters," in *Energy Conversion Congress and Exposition (ECCE)*, 2011, pp. 2467-2474.

[26] T. Kerekes, "Analysis and modeling of transformerless photovoltaic inverter systems," PhD Thesis, Institut for Energiteknik, Aalborg Universitet, Aalborg, Denmark, 2009.

[27] I. Patrao, E. Figueres, F. González-Espín, and G. Garcerá, "Transformerless topologies for grid-connected single-phase photovoltaic inverters," *Renewable and Sustainable Energy Reviews*, vol. 15, pp. 3423-3431, 2011.

[28] M. Liserre, P. Rodríguez , and R. Teodorescu, *Grid converters for photovoltaic and wind power systems*: Wiley, 2011.

[29] "Automatic disconnection device between a generator and the public low-voltage grid," Standard DIN VDE 0126-1-1, 2006.

[30] SMA, "Leading leakage currents: Information on the design of transformerless inverters SUNNY BOY/SUNNY MINI CENTRAL/SUNNY TRIPOWER".

[31] J. A. Cueto, S. Rummel, and N. R. E. Laboratory, *Degradation of photovoltaic modules under high voltage stress in the field: Preprint*: National Renewable Energy Laboratory, 2010.

[32] G. R. Walker and P. C. Sernia, "Cascaded DC-DC converter connection of photovoltaic modules," *Power Electronics, IEEE Transactions on*, vol. 19, pp. 1130-1139, 2004.

[33] S. Busquets-Monge, J. Rocabert, P. Rodriguez, S. Alepuz, and J. Bordonau, "Multilevel diode-clamped converter for photovoltaic generators with independent voltage control of each solar array," *Industrial Electronics, IEEE Transactions on*, vol. 55, pp. 2713-2723, 2008.

[34] S. Kouro, K. Asfaw, R. Goldman, R. Snow, B. Wu, and J. Rodriguez, "NPC multilevel multistring topology for large scale grid connected photovoltaic systems," in *Power Electronics for Distributed Generation Systems (PEDG), 2nd IEEE International Symposium on*, 2010, pp. 400-405.

[35] C. Cecati, F. Ciancetta, and P. Siano, "A multilevel inverter for photovoltaic systems with fuzzy logic control," *Industrial Electronics, IEEE Transactions on*, vol. 57, pp. 4115-4125, 2010.

[36] S. Jain and V. Agarwal, "A single-stage grid connected inverter topology for solar PV systems with maximum power point tracking," *Power Electronics, IEEE Transactions on*, vol. 22, pp. 1928-1940, 2007.

[37] L. Wu, Z. Zhao, and J. Liu, "A single-stage three-phase grid-connected photovoltaic system with modified MPPT method and reactive power compensation," *Energy Conversion, IEEE Transactions on*, vol. 22, pp. 881-886, 2007.

[38] M. E. Ropp and S. Gonzalez, "Development of a MATLAB/Simulink model of a single-phase grid-connected photovoltaic system," *Energy Conversion, IEEE Transactions on*, vol. 24, pp. 195-202, 2009.

[39] G. Grandi, C. Rossi, D. Ostojic, and D. Casadei, "A new multilevel conversion structure for grid-connected PV applications," *Industrial Electronics, IEEE Transactions on*, vol. 56, pp. 4416-4426, 2009.

[40] B. Yang, W. Li, Y. Zhao, and X. He, "Design and analysis of a grid-connected photovoltaic power system," *Power Electronics, IEEE Transactions on*, vol. 25, pp. 992-1000, 2010.

[41] J. Selvaraj and N. A. Rahim, "Multilevel inverter for grid-connected PV system employing digital PI controller," *Industrial Electronics, IEEE Transactions on*, vol. 56, pp. 149-158, 2009.

[42] N. A. Rahim and J. Selvaraj, "Multistring five-level inverter with novel PWM control scheme for PV application," *Industrial Electronics, IEEE Transactions on*, vol. 57, pp. 2111-2123, 2010.

[43] H. Ghoddami and A. Yazdani, "A single-stage three-phase photovoltaic system with enhanced maximum power point tracking capability and increased power rating," *Power Delivery, IEEE Transactions on*, vol. 26, pp. 1017-1029, 2011.

[44] J. Rodriguez, L. Jih-Sheng, and P. Fang Zheng, "Multilevel inverters: A survey of topologies, controls, and applications," *Industrial Electronics, IEEE Transactions on*, vol. 49, pp. 724-738, 2002.

[45] K. A. Corzine, M. W. Wielebski, F. Z. Peng, and W. Jin, "Control of cascaded multilevel inverters," *Power Electronics, IEEE Transactions on*, vol. 19, pp. 732-738, 2004.

[46] B. Wu, *High-power converters and AC drives*: Wiley, 2006.

[47] D. Holmes and T. Lipo, *Pulse width modulation for power converters: Principles and practice*: Wiley, 2003.

[48] B. P. McGrath, T. Meynard, G. Gateau, and D. G. Holmes, "Optimal modulation of flying capacitor and stacked multicell converters using a state machine decoder," *Power Electronics, IEEE Transactions on*, vol. 22, pp. 508-516, 2007.

[49] J. Rodriguez, L. G. Franquelo, S. Kouro, J. I. Leon, R. C. Portillo, M. A. M. Prats, and M. A. Perez, "Multilevel converters: An enabling technology for high-power applications," *Proceedings of the IEEE*, vol. 97, pp. 1786-1817, 2009.

[50] M. Malinowski, K. Gopakumar, J. Rodriguez, and M. A. Perez, "A survey on cascaded multilevel inverters," *Industrial Electronics, IEEE Transactions on*, vol. 57, pp. 2197-2206, 2010.

[51] H. Abu-Rub, J. Holtz, J. Rodriguez, and G. Baoming, "Medium-voltage multilevel converters - state of the art, challenges, and requirements in industrial applications," *Industrial Electronics, IEEE Transactions on*, vol. 57, pp. 2581-2596, 2010.

[52] S. Kouro, M. Malinowski, K. Gopakumar, J. Pou, L. G. Franquelo, B. Wu, J. Rodriguez, M. A. Perez, and J. I. Leon, "Recent advances and industrial applications of multilevel converters," *Industrial Electronics, IEEE Transactions on*, vol. 57, pp. 2553-2580, 2010.

[53] S. Kouro, J. Rodriguez, B. Wu, S. Bernet and M. Perez, "Powering the future of industry: High-power adjustable speed drive topologies" in *IEEE Industry Applications Magazine*, vol. 18, no. 4, pp. 26-29, 2012.

[54] C. Rech and J.R. Pinheiro, "Hybrid multilevel converters: Unified analysis and design considerations," in *Industrial Electronics, IEEE Transactions on*, vol. 54, no. 2, pp. 1092-1104, 2007.

[55] C. Silva, S. Kouro, J. Soto, P. Lezana, "Control of an hybrid multilevel inverter for current waveform improvement", in *Proceedings of IEEE ISIE 2008*, pp. 2329-2335, 2008.

[56] M. Wilkelnkemper, F. Wildner, P. Steimer, "Control of a 6MVA hybrid converter for a permanent-magnet synchronous generator for windpower", in *IEEE ICEM 2008*, pp. 1-6, 2008.

[57] J. Rodriguez, S. Bernet, B. Wu, J. O. Pontt, and S. Kouro, "Multilevel voltage-source-converter topologies for industrial medium-voltage drives," in *Industrial Electronics, IEEE Transactions on*, vol. 54, no. 6, pp. 2930-2945, 2007.

[58] G. Konstantinou, S.R. Pulikanti, and V.G. Agelidis, "Harmonic elimination control of a five-level DC-AC cascaded H-bridge inverter," in *Proceedings of IEEE PEDG*, 2010 pp. 352-357.

[59] S. R. Pulikanti, G. S. Konstantinou, and V. G. Agelidis, "Seven-level cascaded ANPC-based multilevel converter," in *Proceedings of IEEE ECCE*, 2010, pp. 4575-4582.

[60] T. Bruckner, S. Bernet, and H. Guldner "The active NPC converter and its loss-balancing control," in *Industrial Electronics, IEEE Transactions on*, Vol. 52, No. 3, pp. 855-868, 2005.

[61] P. Barbosa, P. K. Steimer, M. Winkelnkemper, J. Steinke, and N. Celanovic, "Active-neutral-point clamped (ANPC) multilevel converter technology," in *Proceedings of EPE Conference*, 2005, pp. 11-14.

[62] S.R. Pulikanti, G.Konstantinou, V.G. Agelidis, "Generalization of flying-capacitor based active-neutral-point-clamped multilevel converter using voltage-level modulation" in *IET Power Electronics*, vol. 5, no.4, pp. 456-466, 2012.

[63] L.G. Franquelo, J. Rodriguez, J.I. Leon, S. Kouro, R. Portillo and M.A.M. Prats, "The age of multilevel converters arrives" in *IEEE Industrial Electronics Magazine*, vol. 2, no. 2, pp. 28-39, 2008.

[64] P. Tenca, "Theoretical and practical aspects characterizing the research on multilevel converters," in *ECPE Workshop on Advanced Multilevel Converter Systems,* Sweden, 2010.

[65] N. Flourentzou, V. G. Agelidis, and G. Demetriades, "VSC based HVDC power transmission systems: An overview," in *Power Electronics, IEEE Transactions on*, vol. 24, no. 3, pp. 592-602, 2009.

[66] E. Cengelci, S. U. Sulistijo, B. O. Woom, P. Enjeti, R. Teodorescu, and F. Blaabjerg, "A new medium voltage PWM inverter topology for adjustable speed drives," in *Conference Record IEEE-IAS Annual Meeting*, 1998, pp. 1416-1423.

[67] M. Hagiwara and H. Akagi, "PWM control and experiment of modular multilevel converters," in *IEEE Power Electronics Specialists Conference, PESC*, 2008, pp. 154-161.

[68] G. Konstantinou and V. G. Agelidis, "Performance evaluation of half-bridge cascaded multilevel converters operated with multicarrier sinusoidal PWM techniques," in *Proceedings of IEEE Conference on Industrial Electronics and Applications*, 2009, pp. 3399-3404.

[69] A. Antonopoulos, L. Angquist and H. P. Nee, "On dynamics and voltage control of the Modular Multilevel Converter," in *Proceedings of European Conference on Power Electronics and Applications, EPE*, 2009, pp. 1-10.

[70] G. Konstantinou, M. Ciobotaru, V.G. Agelidis, "Operation of a modular multilevel converter with selective harmonic elimination PWM," in *Proceedings of IEEE ICPE (ECCE Asia)*, 2011, pp. 999-1004.

[71] J. Wang, B. Wu, and N. R. Zargari, "High-power multi-modular matrix converters with sinusoidal input/output waveforms," in *Proceedings of 35th IEEE IECON*, 2009, pp. 547-552.

[72] G. Gateau, T.A. Meynard, H. Foch, "Stacked Multicell converter (SMC): properties and design", in *Proceedings of IEEE PESC*, 2001, pp. 1583-1588.

[73] V.G. Agelidis, A. I. Balouktsis "A seven-level defined selective harmonic elimination PWM strategy," *Proceedings of IEEE PESC*, 2006, pp. 1-7.

[74] Z. Du, L. M. Tolbert, B. Ozpineci, and J. N. Chiasson, "Fundamental frequency switching strategies of a seven-level hybrid cascaded H-bridge multilevel inverter," in *Power Electronics, IEEE Transactions on*, vol. 24, no. 1, pp. 25-33, 2009.

[75] G. Konstantinou, M.S.A. Dahidah, V.G. Agelidis, "Solution trajectories for selective harmonic elimination PWM for seven-level waveforms: analysis and implementation", in *IET Power Electronics*, Vol. 5, No. 1, pp. 22-30, 2012.

[76] F. Khairy, L. Hyun Woo, T. Mishima, and M. Nakaokal, "Boost-half bridge single power stage PWM DC-DC converter for small scale fuel cell stack," in *Power and Energy Conference, PECon, IEEE International*, 2006, pp. 426-431.

[77] C. Yoon, J. Kim, and S. Choi, "Multiphase DC-DC converters using a boost-half-bridge cell for high-voltage and high-power applications," *Power Electronics, IEEE Transactions on*, vol. 26, pp. 381-388, 2011.

[78] N. Femia, G. Lisi, G. Petrone, G. Spagnuolo, and M. Vitelli, "Distributed maximum power point tracking of photovoltaic arrays: Novel approach and system analysis," *Industrial Electronics, IEEE Transactions on*, vol. 55, pp. 2610-2621, 2008.

[79] V. Quaschning, *Understanding renewable energy systems*: Earthscan, 2005.

[80] D. P. Hohm and M. E. Ropp, "Comparative study of maximum power point tracking algorithms," *Progress in Photovoltaics: Research and Applications*, vol. 11, pp. 47-62, 2003.

[81] Modeling of a Photovoltaic String using PLECS, http://www.plexim.com

[82] PLECS Blockset, http://www.plexim.com/products/plecs_blockset.html

[83] SMA solar inverters, SUNNY CENTRAL 800MV/1000MV/1250MV, http://www.sma.de/en/products/solar-inverters/sunny-central/sunny-central-800mv-1000mv-1250mv.html

[84] O. Alonso, P. Sanchis, E. Gubia, and L. Marroyo, "Cascaded H-bridge multilevel converter for grid connected photovoltaic generators with independent maximum power point tracking of each solar array," in *Power Electronics Specialist Conference, PESC, IEEE 34th Annual*, 2003, pp. 731-735 vol.2.

[85] J. J. Negroni, F. Guinjoan, C. Meza, D. Biel, and P. Sanchis, "Energy-sampled data modeling of a cascade H-bridge multilevel converter for grid-connected PV systems," in *International Power Electronics Congress, 10th IEEE*, 2006, pp. 1-6.

[86] E. Villanueva, P. Correa, and J. Rodriguez, "Control of a single phase H-bridge multilevel inverter for grid-connected PV applications," in *Power Electronics and Motion Control Conference, EPE-PEMC, 13th IEEE*, 2008, pp. 451-455.

[87] S. Kouro, B. Wu, A. Moya, E. Villanueva, P. Correa, and J. Rodriguez, "Control of a cascaded H-bridge multilevel converter for grid connection of photovoltaic systems," in *Industrial Electronics, IECON, 35th Annual Conference of IEEE*, 2009, pp. 3976-3982.

[88] E. Villanueva, P. Correa, J. Rodriguez, and M. Pacas, "Control of a single-phase cascaded H-bridge multilevel inverter for grid-connected photovoltaic systems," *Industrial Electronics, IEEE Transactions on*, vol. 56, pp. 4399-4406, 2009.

[89] J. J. Negroni, D. Biel, F. Guinjoan, and C. Meza, "Energy-balance and sliding mode control strategies of a cascade H-bridge multilevel converter for grid-connected PV systems," in *Industrial Technology (ICIT), IEEE International Conference on*, 2010, pp. 1155-1160.

[90] Y. Zhou, L. Liu, H. Li, and L. Wang, "Real time digital simulation (RTDS) of a novel battery-integrated PV system for high penetration application," in *Power Electronics for Distributed Generation Systems (PEDG), 2nd IEEE International Symposium on*, 2010, pp. 786-790.

[91] X. Bailu, F. Filho, and L. M. Tolbert, "Single-phase cascaded H-bridge multilevel inverter with nonactive power compensation for grid-connected photovoltaic generators," in *Energy Conversion Congress and Exposition (ECCE)*, 2011, pp. 2733-2737.

[92] B. Johnson, P. Krein, and P. Chapman, "Photovoltaic AC module composed of a very large number of interleaved inverters," in *Applied Power Electronics Conference and Exposition (APEC), 26th Annual IEEE*, 2011, pp. 976-981.

[93] M. A. Rezaei, S. Farhangi, and H. Iman-Eini, "Enhancing the reliability of single-phase CHB-based grid-connected photovoltaic energy systems," in *Power Electronics, Drive Systems and Technologies Conference (PEDSTC)*, 2011, pp. 117-122.

[94] S. Rivera, S. Kouro, B. Wu, J. I. Leon, J. Rodriguez, and L. G. Franquelo, "Cascaded H-bridge multilevel converter multistring topology for large scale photovoltaic systems," in *Industrial Electronics (ISIE), IEEE International Symposium on*, 2011, pp. 1837-1844.

[95] S. Wang, J. Zhao, and C. Shi, "Research on a three-phase cascaded inverter for grid-connected photovoltaic systems," in *Advanced Power System Automation and Protection (APAP), International Conference on*, 2011, pp. 543-548.

[96] X. Chavarria, D. Biel, F. Guinjoan, C. Meza, and J. Negroni, "Energy-balance control of PV cascaded multilevel grid-connected inverters for phase-shifted and level-shifted pulse-width modulations," *Industrial Electronics, IEEE Transactions on*, vol. 99, pp. 1-1, 2012.

[97] H. S. Krishnamoorthy, S. Essakiappan, P. N. Enjeti, R. S. Balog, and S. Ahmed, "A new multilevel converter for Megawatt scale solar photovoltaic utility integration," in *Applied Power Electronics Conference and Exposition (APEC), 27th Annual IEEE*, 2012, pp. 1431-1438.

[98] J. Chen, X. Xu, S. Li, K. Hu, and L. Yu, "Implementation of grid-connected cascaded multi-level inverter based on FPGA for centralized photovoltaic generation," *Energy Procedia*, vol. 17, Part B, pp. 1185-1192, 2012.

[99] S. Essakiappan, H. S. Krishnamoorthy, P. Enjeti, R. S. Balog, and S. Ahmed, "A new control strategy for megawatt scale multilevel photovoltaic inverters under partial shading," in *Power Electronics for Distributed Generation Systems (PEDG), 3rd IEEE International Symposium on*, 2012, pp. 336-343.

[100] S. Rivera, B. Wu, S. Kouro, H. Wang, and D. Zhang, "Cascaded H-bridge multilevel converter topology and three-phase balance control for large scale photovoltaic systems," in *Power Electronics for Distributed Generation Systems (PEDG), 3rd IEEE International Symposium on*, 2012, pp. 690-697.

[101] H. Choi, W. Zhao, M. Ciobotaru, and V. G. Agelidis, "Large-scale PV system based on the multiphase isolated DC/DC converter," in *Power Electronics for Distributed Generation Systems (PEDG), 3rd IEEE International Symposium on*, 2012, pp. 801-807.

[102] W. Zhao, H. Choi, G. Konstantinou, M. Ciobotaru, and V. G. Agelidis, "Cascaded H-bridge multilevel converter for large-scale PV grid-integration with isolated DC-DC stage," in *Power Electronics for Distributed Generation Systems (PEDG), 3rd IEEE International Symposium on*, 2012, pp. 849-856.

[103] L. Xu, Y. Han, M. M. Khan, J. M. Pan, C. Chen, G. Yao, and L. D. Zhou, "Analysis and effective controller design for the cascaded H-bridge multilevel APF with adaptive signal processing algorithms," *International Journal of Circuit Theory and Applications*, pp. n/a-n/a, 2011.

[104] Y. He, S. Du, and J. Liu, "A study on the DC link voltage balancing for power conditioners based on cascaded H-bridges," in *Power Electronics and ECCE Asia (ICPE & ECCE), IEEE 8th International Conference on*, 2011, pp. 1821-1827.

[105] M. Zygmanowski, B. Grzesik, and J. Michalak, "Power conditioning system with cascaded H-bridge multilevel converter DC-link voltage balancing method," in *Power Electronics and Applications (EPE), Proceedings of the 14th European Conference on*, 2011, pp. 1-10.

[106] W. A. Omran, M. Kazerani, and M. M. A. Salama, "Investigation of methods for reduction of power fluctuations generated from large grid-connected photovoltaic systems," *Energy Conversion, IEEE Transactions on*, vol. 26, pp. 318-327, 2011.

[107] L. Asiminoaei, R. Teodorescu, F. Blaabjerg, and U. Borup, "Implementation and test of an online embedded grid impedance estimation technique for PV inverters," *Industrial Electronics, IEEE Transactions on*, vol. 52, pp. 1136-1144, 2005.

[108] H. Langkowski, T. Trung Do, K. D. Dettmann, and D. Schulz, "Grid impedance determination - relevancy for grid integration of renewable energy systems," in Industrial Electronics, IECON, 35th Annual Conference of IEEE, 2009, pp. 516-521.

[109] A. A. Rockhill, M. Liserre, R. Teodorescu, and P. Rodriguez, "Grid-filter design for a multimegawatt medium-voltage voltage-source inverter," *Industrial Electronics, IEEE Transactions on*, vol. 58, pp. 1205-1217, 2011.

[110] F. Blaabjerg, C. Zhe, and S. B. Kjaer, "Power electronics as efficient interface in dispersed power generation systems," *Power Electronics, IEEE Transactions on*, vol. 19, pp. 1184-1194, 2004.

[111] F. Blaabjerg, F. Iov, R. Teodorescu, and Z. Chen, "Power electronics in renewable energy systems," in *Power Electronics and Motion Control Conference, EPE-PEMC, 12th International*, 2006, pp. 1-17.

[112] F. Blaabjerg, R. Teodorescu, M. Liserre, and A. V. Timbus, "Overview of control and grid synchronization for distributed power generation systems," *Industrial Electronics, IEEE Transactions on*, vol. 53, pp. 1398-1409, 2006.

[113] R. Teodorescu, F. Blaabjerg, M. Liserre, and P. C. Loh, "Proportional-resonant controllers and filters for grid-connected voltage-source converters," *Electric Power Applications, IEEE Proceedings*, vol. 153, pp. 750-762, 2006.

[114] A. V. Timbus, M. Ciobotaru, R. Teodorescu, and F. Blaabjerg, "Adaptive resonant controller for grid-connected converters in distributed power generation systems," in *Applied Power Electronics Conference and Exposition, APEC, 21st Annual IEEE*, 2006, pp. 1601-1606.

[115] A. Timbus, M. Liserre, R. Teodorescu, P. Rodriguez, and F. Blaabjerg, "Evaluation of current controllers for distributed power generation systems," *Power Electronics, IEEE Transactions on*, vol. 24, pp. 654-664, 2009.

[116] IEEE Std 1547-2003, "IEEE standard for interconnecting distributed resources with electric power systems," ed: The Institute of Electrical and Electronics Engineers, 2003.

[117] B.-I. Craciun, T. Kerekes, D. Sera, and R. Teodorescu, "Overview of recent grid codes for PV power integration," in *Optimization of Electrical and Electronic Equipment (OPTIM), 13th International Conference on*, 2012, pp. 959-965.

[118] A. Hoke and P. Komor, "Maximizing the benefits of distributed photovoltaics," *The Electricity Journal*, 2012.

[119] C. Lueken, P. M. S. Carvalho, and J. Apt, "Distribution grid reconfiguration reduces power losses and helps integrate renewables," *Energy Policy*, 2012.

[120] P. Lund, "Large-scale urban renewable electricity schemes - Integration and interfacing aspects," *Energy Conversion and Management*, 2012.